Power Control and Full-Duplex Wireless Networks

A Dissertation

Submitted to the Graduate School
of the University of Notre Dame
in Partial Fulfillment of the Requirements
for the Degree of

Doctor of Philosophy

by

Zhen Tong,

Martin Haenggi, Director

Graduate Program in Electrical Engineering
Notre Dame, Indiana
February 2015

Power Control and Full-Duplex Wireless Networks

Abstract

by

Zhen Tong

Medium Access Control (MAC) protocols deal with the problem of effectively utilizing wireless communication channels. Therefore, efficient MAC schemes play an important role in determining the fundamental capacity of wireless networks. In this thesis, we deal with this fundamental problem of how to design an effective MAC protocol to maximize the utilization of the shared wireless medium. Two types of techniques that can be utilized to design good MAC scheme and potentially significantly improve the wireless network performance are studied: power control and full-duplex transmission.

For any wireless communication system, it is critical to have an energy efficient MAC scheme given the limited power resource. This leads us to a question, which is how *power control* algorithm can help with the design of the MAC scheme? To answer this question, the classic Foschini-Miljanic power control algorithm has been analyzed from a geometric perspective. A novel tool, the Möbius transform, has been utilized for the first time to study the convergence condition of the power control algorithm. Based on the analysis, we proposed an energy efficient MAC scheme that enables the link nesting and therefore greatly improves the spatial reuse of the wireless networks. Moreover, the effects of the power constraints and fading on the convergence of the power control algorithms have also been considered in the context of random networks.

While focusing on the quest for a good MAC scheme that works for the current wireless systems, an alternative way is to think outside the box and design a wireless system that is fundamentally different from the current communication system model. One of the important issues that wireless medium makes the MAC design more challenging than the wireline networks is the half duplex operation which means that a node cannot transmit and receive simultaneously over the same frequency band due to overwhelming self-interference. This thesis challenges the paradigm by proposing a comprehensive investigation of the physical, medium access control and network layers of *virtual full-duplex* networks based on *rapid on-off-division duplex (RODD)*. The key to RODD is to allow all nodes to transmit and receive simultaneously by letting each node transmit through the *on-slots* of its on-off mask and receive over the *off-slots*. In case of a point-to-point connection of two nodes, both nodes can simultaneously transmit a message and receive a message at the same time, achieving full duplex at the frame level. Part of this thesis is design and prototype implementation of this virtual full-duplex wireless networks using software-defined radios (SDR) and evaluating its performance. It puts much emphasis on the practicality of the proposed technique. Novel channel coding, synchronization and estimation algorithms have been designed for the RODD scheme to correctly recover the received on/off signal. We implemented the RODD scheme using software-defined radio and tested the performance of the scheme.

Another type of full-duplex is achieved by canceling the self-interference caused by one's own transmitter. This thesis also investigates the throughput for wireless network with full-duplex radios using stochastic geometry. Full-duplex (FD) radios can exchange data simultaneously with each other. On the other hand,

the downside of FD transmission is that it will inevitably cause extra interference to the network compared to half-duplex (HD) transmission. Moreover, the residual self-interference has negative effects on the network throughput. In this thesis, we focus on a wireless network of nodes with both HD and FD capabilities and derive and optimize the throughput in such a network. Our analytical result shows that if the network is adapting an ALOHA protocol, the maximal throughput is achieved by scheduling all concurrently transmitting nodes to work in either FD mode or HD mode depending on one simple condition. Moreover, the effects of imperfect self-interference cancellation on the signal-to-interference ratio (SIR) loss and throughput are also analyzed based on our mathematical model. We rigorously quantify the impact of imperfect self-interference cancellation on the throughput gain, transmission range, and other metrics, and we establish the minimum amount of self-interference suppression needed for FD to be beneficial.

DEDICATION

To Qian, my wife and Ashley, my lovely daughter

CONTENTS

FIGURES

TABLES

ACKNOWLEDGMENTS

To be done.

SYMBOLS

$\mathbb{E}$	expectation
$[n]$	the set {1,2,$\cdots$,n}
$\mathbb{N}$	natural numbers $\{1, 2, \cdots\}$
$\mathbb{R}^d$	d-dimensional Euclidean space
o	origin of $\mathbb{R}^d$
$\|\cdot\|$	Euclidean metric of $x \in \mathbb{R}^d$
$\mathbb{R}^+$	non-negative real numbers
$\mathsf{1}(\cdot)$	indicator function
$\mathsf{1}_A(x)$	$\equiv \mathsf{1}(x \in A)$
$\triangleq$	definition

CHAPTER 1

INTRODUCTION

THE rapid technological advances and innovations of the past few decades have pushed wireless communication from concept to reality and changed people's way of life dramatically. With predictions of near exponential growth in the data demand in the next few years, pressure is mounting on the cellular providers to utilize scarce spectrum resources to lauch new wireless services. It becomes more and more critical to make fully use of a given shared spectrum resourse. MAC protocols deal with the problem of effectively utilizing wireless communication channels. Therefore, efficient MAC schemes play an important role in determining the fundamental capacity of the wireless networks. In our thesis, we will deal with the fundamental problem of how to design an effective MAC protocol to maximize the utilization of the shared wireless medium.

1.1 Power Control and MAC Design

Transmission power control plays an important role in the design and operation of wireless networks and can improve the energy efficiency and spatial reuse of the MAC schemes. There has been intensive recent research on MAC protocols for wireless networks (see [46, 47] and the references therein). Some MAC protocols with power control are considered in [1, 40, 55]. Limited to CSMA, transmissions

are scheduled in such a way that close nodes never transmit simultaneously to avoid collision.

In Chapter 2 , the classic Foschini-Miljanic power control algorithm [21] has been analyzed from a geometric perspective. A novel tool, Möbius transform [35], has been utilized for the first time to study the convergence condition of the power control algorithm. Based on the analysis, we proposed an energy efficient MAC scheme that enables the link nesting and therefore greatly improves the spatial reuse of the wireless networks. Moreover, the effects of the power constraints on the convergence of the power control algorithms have also been considered in the context of random networks.

1.2 Prototype of Virtual Full Duplex via Rapid-On-Off-Division Duplex

To date, almost all radios used in commercial and military wireless networks are *half-duplex (HD)*. Due to the limited dynamic range of affordable radio frequency (RF) circuits, such a radio cannot resolve the desired signal picked up by its receive antenna when it is overwhelmed by its own transmitted signal. The problem is exacerbated by the fact that a node's own transmission picked up by its own antenna is typically many orders of magnitude stronger than the desired received signal (often by over 100 dB). The proposed research challenges the conventional wisdom of separating transmit and receive frames in time or frequency.

Chapter 3 explores a novel *full-duplex (FD)* and *virtual full-duplex* paradigm for the physical (PHY) and medium access control (MAC) layers of wireless networks based on *rapid on-off-division duplex (RODD)*[29]. The key to RODD is to allow all nodes to transmit and receive simultaneously by letting each node transmit through the *on-slots* of its on-off mask and receive over the *off-slots*. In case of a

point-to-point connection of two nodes: both nodes can simultaneously transmit a message and receive a message at the same time, achieving full duplex at the frame level. We describe an RODD prototype to prove its key concepts, including re-designed synchronization and coding schemes. Simulation results are presented for comparison with the measurements obtained from a software-defined radio implementation of RODD. The effects of on-off signaling on the performance are investigated experimentally. In particular, the bit error rate is measured and compared with the simulation results. Our results indicate that virtual full duplex is feasible on USRPs/LabVIEW platform via RODD.

1.3 Throughput Analysis of Full-Duplex Wireless Networks

Besides achieving full duplex via RODD, there is another type of FD techniques in which extra circuits are added to cancel the self-interference. Chapter 4 explores the impacts of FD transmission on the network throughput and utilizes the powerful analytical tools from stochastic geometry to study the throughput performance of a wireless network of nodes with both FD and HD capabilities. Our results analytically show that for an ALOHA MAC protocol, FD always outperforms HD in terms of throughput if perfect self-interference cancellation is assumed. However, for a path loss exponent α, the achievable throughput gain is upper bounded by $\frac{2\alpha}{\alpha+2}$, i.e., it ranges from 0-33% for the practical range $\alpha \in (2, 4]$. This result holds for arbitrary node densities, link distances and SIR regimes. Moreover, we model imperfect self-interference cancellation and quantify its effects on the throughput. Imperfect self-interference cancellation causes a SIR loss in the FD transmission and thus reduces the throughput gain between the FD network and HD network. Tight bounds on the SIR loss are obtained using the concept of horizontal shifts

of the SIR distribution. The amount of self-interference cancellation determines if HD or FD is preferable in the networks.

Parts of the results above appear in [63–68]. The RODD work in Chapter 3 is being studied and implemented with Christina Russ in our group.

CHAPTER 2

POWER CONTROL AND MÖBIUS MAC DESIGN

2.1 Introduction

2.1.1 Motivation and Contribution

The Foschini-Miljanic (FM) power control algorithm in [21] is a distributed and dynamic power control algorithm to adjust transmit power levels using the instantaneous signal-to-interference ratio (SIR) or signal-to-interference-and-noise ratio (SINR) measured at the receiver such that the SNR or SINR converges to a desired value. While the convergence condition of the FM power control algorithm has been well studied, it has not been analyzed from a geometric perspective. A geometric analysis can help researchers better understand the dependencies between the links in a wireless network and provide insight into the design of MAC schemes with dynamic power control. In this chapter, we present such an analysis. An analytical tool that is novel in this context, the Möbius transform [35], is introduced to analyze the convergence condition. The Möbius transform has the property of mapping generalized circles to generalized circles, which can be used to illustrate the convergence condition geometrically. The analysis of the two-transmitter case illustrates that link nesting is possible with distributed and dynamic power control, which enables the design of MAC schemes that schedule link *pairs* instead of individual links.

A peak power constraint is an important factor that affects the convergence of dynamic power control algorithms. Existing dynamic power control algorithms with peak power constraint usually let the transmitters continue to transmit at peak power after the transmit power hits the power ceiling. However, their receivers' SINRs cannot achieve the desired SINR threshold. That is, while the convergence of the transmit powers is guaranteed, not all the receivers' SINRs converge to the desired threshold. Therefore, the quantification of the convergence of the receivers' SINRs under a peak power constraint is an unsolved problem. In this chapter, a novel metric called *convergence probability* is defined to show the impact of the peak power constraint, and the properties and bounds of the convergence probability are derived theoretically for random networks.

Our main contributions are summarized as follows:

1. *Geometric analysis*: A novel analytical tool, the Möbius transform, is used for the geometric analysis of the convergence condition for the FM power control algorithm without fading.

2. *Peak power constraint:* The effects of the peak power constraints on the networks are studied in detail. Random networks are used for the first time to study the convergence of the dynamic power control algorithm with peak power constraint.

3. *Möbius MAC scheme:* A novel MAC scheme based on the geometric analysis and observations from peak power analysis is proposed to schedule link pairs with unequal link distances. Simulation results show that our MAC scheme is much more efficient to schedule links than the traditional CSMA scheme and has better quality of service (QoS) performance in terms of transport density.

2.1.2 Related Work

Transmission power control plays an important role in the design and operation of wireless networks. Much of the study on cellular network power control started in the 1990s and involved minimizing the total power while maintaining a fixed target SIR or SINR at the desired receiver [21, 25, 75]. An efficient and distributed power control algorithm for cellular systems, now commonly referred to as the Foschini-Miljanic algorithm, was provided in [21]. The authors in [19] have shown the applicability of this algorithm to wireless ad hoc networks. Joint power control and scheduling algorithms have been proposed in [19, 49]. Different types of power control schemes for cellular systems have been presented in [14] and references therein. Recently, power control for various new types of wireless networks has been extensively studied, *e.g.,* [10] for two-tier femtocell networks and [56, 61] for cognitive radio networks. Power control problem for random wireless networks has also been studies recently in [78, 79]. Moreover, constrained power control has been studied in [24, 26] since the maximum transmit power of a mobile user or any wireless transmitter is limited. The convergence of the distributed and dynamic power control algorithm with peak power constraint has been analyzed in [36, 73] for cellular networks. The admission-centric power control problem have been studied extensively, see [5, 72] for example, with the goal to decide if a newcomer can be admitted into the network without affecting the active users. [5] lets new links power up in a fixed step to avoid sudden change in interference while the active links are provided with a margin protection. A criterion based on a certain discriminant has been derived to serve as the admission condition in [72] .

A heuristic scheduling scheme is provided in [19] to determine a maximum

subset of concurrently active links by shutting down the link with the minimum SINR until all the SINR requirements are satisfied. However, it is not distributed since one node needs all the SINR information from other nodes in order to decide if it can transmit or not. We propose a fully distributed MAC scheme that includes the peak power constraint in a natural way and schedules link in pairs. In our MAC scheme, called the Möbius MAC scheme, the geometric analysis that is derived from the two-transmitter case is utilized to serve as a criterion to schedule links in pairs.

2.1.3 Organization of the Chapter

The rest of this chapter is organized as follows. In Section 2.2, the system model is introduced, assumptions stated and the metrics used in the chapter defined. Section 2.3 discusses the convergence condition of the power control algorithm from a geometric perspective. The power control algorithm under the peak power constraint is also studied in detail in Section 2.4. Section 2.5 describes the novel energy-efficient MAC scheme. In Section 2.6, applications of our analysis to cognitive networks and heterogeneous networks are discussed. We conclude our work in Section 2.7.

2.2 System Model

Consider a wireless network where all nodes share the same frequency band. Assume that the network has n links with each link consisting of a transmitter and its associated receiver. Thus, there are n transmitters and n receivers, and the sets of transmitting and receiving nodes are disjoint. An example of such a wireless network is illustrated in Fig. 2.1.

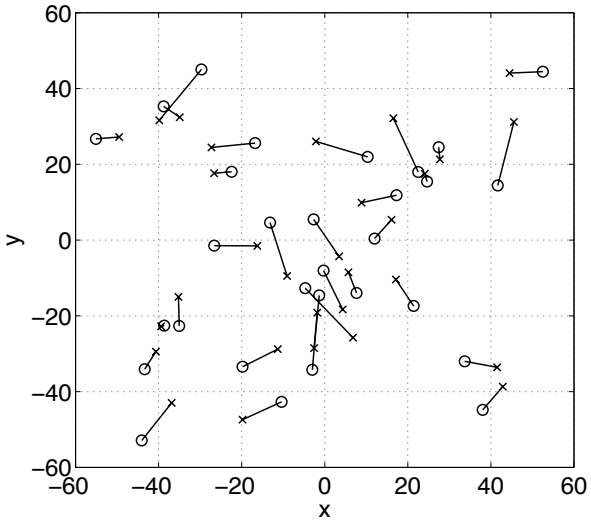

Figure 2.1. An example of the class of wireless networks considered in this chapter. Crosses indicate the transmitters, and circles indicate the receivers.

The channel power gain from transmitter j to receiver i is denoted by h_{ij}. Note that fading is not considered throughout the chapter. The QoS is represented by the SINR at the intended receiver. For a wireless network with n links, the SINR at the ith receiver is given by

$$\rho_i = \frac{h_{ii}P_i}{\sum_{j\neq i} h_{ij}P_j + \eta}, \tag{2.1}$$

where P_i is the power of the ith transmitter, and η is the noise power level.

2.3 Convergence Condition for Power Control

2.3.1 Review of Power Control Algorithm

Here we briefly review the power control algorithm proposed in [21]. The goal of the algorithm is to find the minimal solution of the transmit powers such that the SINR at each receiver meets a given threshold $\rho > 0$ required for acceptable performance. This constraint can be represented in matrix form as

$$(I - F)P \geq u, \tag{2.2}$$

where $P = (P_1, \cdots, P_n)^T \in \mathbb{R}_+^n$ (denoted as $P > 0$) is the column vector of transmit powers,

$$u = \left(\frac{\rho\eta}{h_{11}}, \frac{\rho\eta}{h_{22}}, \ldots, \frac{\rho\eta}{h_{nn}} \right)^T, \tag{2.3}$$

and F is a matrix with

$$F_{ij} = \begin{cases} 0, & \text{if } i = j \\ \frac{\rho h_{ij}}{h_{ii}}, & \text{if } i \neq j \end{cases} \tag{2.4}$$

where $i, j \in [n] \triangleq \{1, 2, \cdots, n\}$.

The Perron–Frobenius eigenvalue σ_F of the matrix F is defined as the maximum modulus of all eigenvalues of F, i.e., $\sigma_F = \max_{1 \leq i \leq n} \{|\lambda_i|\}$, where $\lambda_1, \lambda_2, \cdots, \lambda_n$ are the eigenvalues of F. From [21], if and only if $\sigma_F < 1$, $(I - F)^{-1}$ exists and $P^* = (I - F)^{-1}u > 0$ is the minimal power solution to (2.2). That is, if P is any other solution to (2.2), $P \geq P^*$ componentwise. Therefore, the total power consumption can be minimized by allocating the transmit powers P^*. $\sigma_F < 1$ also guarantees that the iterative distributed power control algorithm

$$P(k+1) = FP(k) + u, \tag{2.5}$$

or, equivalently,

$$P_i(k+1) = \frac{\rho}{\rho_i(k)} P_i(k) \tag{2.6}$$

converges to P^*, where $\rho_i(k)$ is the instantaneous SINR for ith receiver at time k, $P_i(k)$ is the power of the ith transmitter at time $k \in \mathbb{N}$, and the initial value $P(0)$ is given.

2.3.2 Geometric Analysis of the Convergence Condition in the Two-link Case

The path loss is assumed to be proportional to the γth power of the distance between the transmitter and the receiver. The channel power gain from transmitter j to receiver i is thus given by

$$h_{ij} = \left(\frac{d_0}{d_{ij}} \right)^{\gamma}, \tag{2.7}$$

where γ is the path loss exponent, d_0 is the normalization distance, and d_{ij} is the distance between transmitter j and receiver i.

For the two-transmitter case, the eigenvalues of the matrix F are $\pm\rho\sqrt{h_{12}h_{21}/h_{11}h_{22}}$, where h_{ij} is given in (2.7). Hence,

$$\sigma_F = \rho\sqrt{h_{12}h_{21}/h_{11}h_{22}} < 1$$

leads to

$$\frac{d_{12}d_{21}}{d_{11}d_{22}} > \rho^{\frac{2}{\gamma}}. \tag{2.8}$$

Let $\mathbf{t}_i \in \mathbb{R}^2$ be transmitter i's position, $i \in \{1, 2\}$, $\mathbf{r}_i \in \mathbb{R}^2$ be receiver i's position, and let

$$d_i \triangleq \|\mathbf{t}_i - \mathbf{r}_i\|; \quad \widetilde{d}_i \triangleq \|\mathbf{t}_i - \mathbf{r}_{3-i}\| \tag{2.9}$$

be the distances of the desired links and the interfering "links", respectively. Also, let $\hat{\rho} \triangleq \rho^{\frac{1}{\gamma}}$. Then the convergence condition in (2.8) can be rewritten as

$$\frac{\widetilde{d}_1 \widetilde{d}_2}{d_1 d_2} > \hat{\rho}^2, \tag{2.10}$$

Our goal is to find out what constraints on their placement the two transmitters (Tx1, Tx2) have to satisfy in order to guarantee that the distributed power control algorithm converges, given the locations of the receivers.

First, letting

$$b(x, y) \triangleq \hat{\rho}\frac{x}{y}, \tag{2.11}$$

the convergence condition is equivalent to

$$b(d_1, \widetilde{d}_1) b(d_2, \widetilde{d}_2) < 1, \tag{2.12}$$

which shows the symmetry in the two links.

By Apollonius's definition of a circle [53], $\left\{\mathbf{t}_i : b(d_i, \widetilde{d}_i) = c\right\}$, where c is a constant, defines a circle if the $\mathbf{r}_i$'s are given. Hence, (2.12) means that if $\mathbf{t}_1$ sits on the circle defined by $b(d_1, \widetilde{d}_1) = c$, $\mathbf{t}_2$ must be in the region $\left\{\mathbf{t}_2 : b(d_2, \widetilde{d}_2) < c^{-1}\right\}$ which is either inside or outside the circle $b(d_2, \widetilde{d}_2) = c^{-1}$ depending on the value of c, and vice versa.

Now, assume that $\mathbf{r}_1 = (-a, 0)$ and $\mathbf{r}_2 = (a, 0)$ so that the distance between the two receivers is $2a$. Fixing the two receivers at the given locations means

$$d_1 \triangleq \|\mathbf{t}_1 - (-a, 0)\|,\ d_2 \triangleq \|\mathbf{t}_2 - (a, 0)\|; \quad \widetilde{d}_1 \triangleq \|\mathbf{t}_1 - (a, 0)\|,\ \widetilde{d}_2 \triangleq \|\mathbf{t}_2 - (-a, 0)\|. \tag{2.13}$$

Note that $b(d_1, \widetilde{d}_1) = c$ is equivalent to $\mathbf{t}_1 \in \mathcal{C}_1(c)$, where $\mathcal{C}_1(c)$ is the circle

$$\mathcal{C}_1(c) = \{x, y \in \mathbb{R} : (x - x_1(c))^2 + y^2 = R_1^2(c)\}, \tag{2.14}$$

with $x_1(c) = a\frac{c^2+\hat{\rho}^2}{c^2-\hat{\rho}^2}$, $R_1(c) = \frac{2ac\hat{\rho}}{|\hat{\rho}^2-c^2|}$.

Similarly, $b(d_2, \widetilde{d}_2) = c^{-1}$ defines another circle $\mathcal{C}_2(c)$ given by

$$\mathcal{C}_2(c) = \{x, y \in \mathbb{R} : (x - x_2(c))^2 + y^2 = R_2^2(c)\}, \tag{2.15}$$

with $x_2(c) = a\frac{c^2+\hat{\rho}^{-2}}{c^2-\hat{\rho}^{-2}}$, $R_2(c) = \frac{2ac\hat{\rho}^{-1}}{|\hat{\rho}^{-2}-c^2|}$.

With the above setup, we have the following lemma, which describes the constraints on the placement of two transmitters given that the locations of two receivers are known.

Lemma 1. *Given* $\mathbf{r}_1$ *and* $\mathbf{r}_2$*, if* $\mathbf{t}_1 \in \mathcal{C}_1(c)$*, where* $c > \hat{\rho}^{-1}$*, then* $\mathbf{t}_2 \in \mathcal{D}_2$*, where* $\mathcal{D}_2$ *is the disk enclosed by* $\mathcal{C}_2$*; conversely, if* $\mathbf{t}_1 \in \mathcal{C}_1(c)$*, where* $c < \hat{\rho}^{-1}$*, then* $\mathbf{t}_2 \in \mathcal{D}_2^{\mathrm{c}}$*, where* $^{\mathrm{c}}$ *indicates set complement,* i.e., $\mathcal{D}_2^{\mathrm{c}} = \mathbb{R}^2 \backslash \mathcal{D}_2$.

Proof. The proof is straightforward from the definitions of the two circles $\mathcal{C}_1(c)$ and $\mathcal{C}_2(c)$ and the condition in (2.12). Hence, it is omitted here. □

Fig. 2.2 illustrates Tx2's location constraint for different $u_1 = d_1/\widetilde{d}_1$. For Fig. 2.2(a), when Tx1 is on the dashed circle ($u_1 = 2$), the dotted region shows the region of convergence for the power control algorithm. Here, the region of convergence (ROC) is defined as the set of Tx2's locations that guarantee the convergence of the SINRs to the desired threshold for both receivers when $\mathbf{t}_1 \in \mathcal{C}_1(c)$. This case is especially interesting because Rx2 is sometimes closer to Tx1 than Rx1 but can still receive from Tx2 as long as Tx2 is inside the circle $\mathcal{C}_2$. Moreover, Fig. 2.2(d) shows that the Tx1-Rx1 link can even *nest within* the Tx2-Rx2 link.

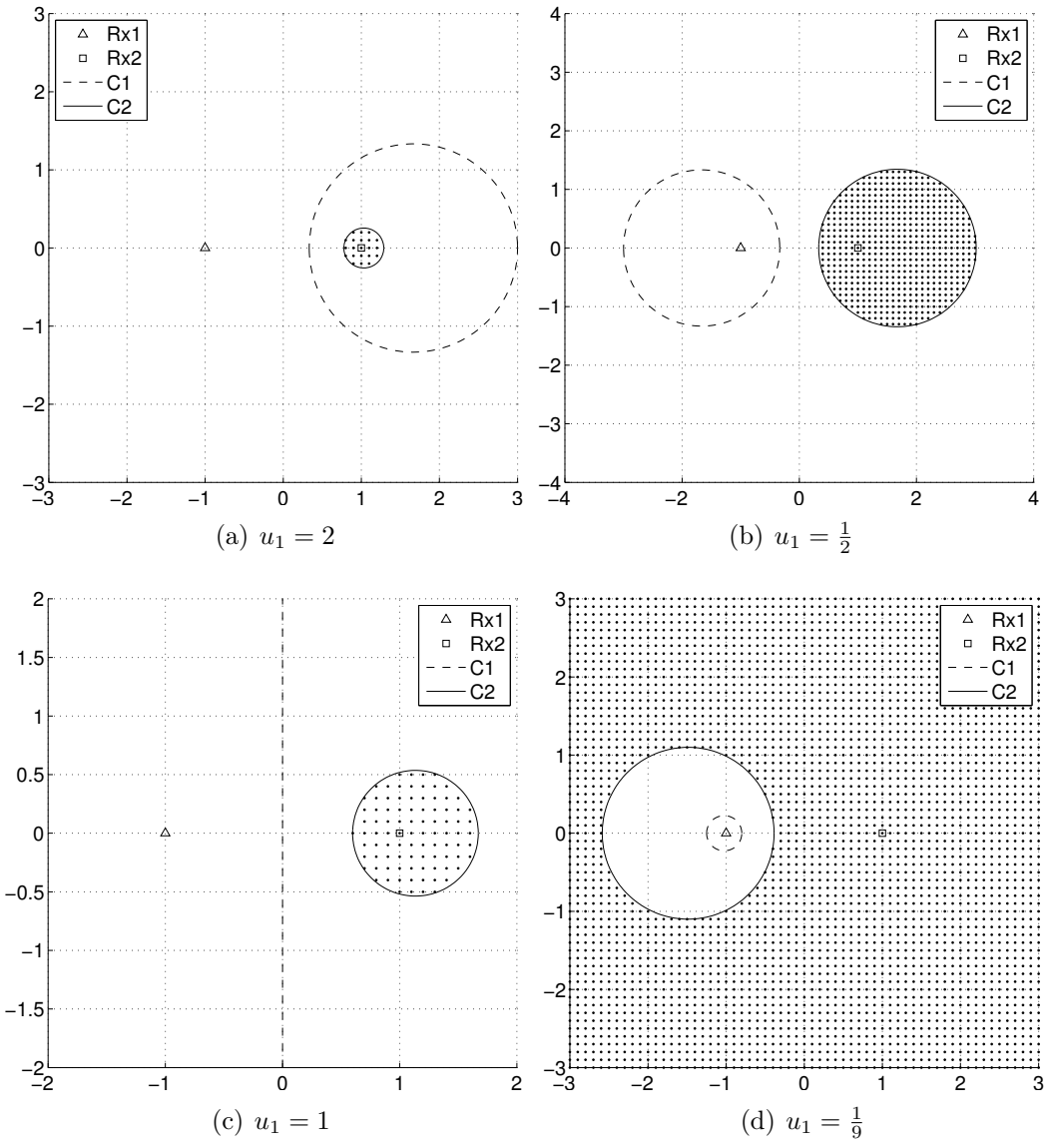

(a) $u_1 = 2$ (b) $u_1 = \frac{1}{2}$

(c) $u_1 = 1$ (d) $u_1 = \frac{1}{9}$

Figure 2.2. Tx2's ROC for different $u_1 = d_1/\widetilde{d}_1$. The other parameters are $a = 1, \gamma = 4, \rho = 12$ dB.

2.3.3 Möbius Transform

In Section 2.3.2, we have seen that for every circle $\mathcal{C}_1(c)$ on which Tx1 is located, there is a circle $\mathcal{C}_2(c)$ which serves as the boundary for Tx2's ROC. That means that there is one-to-one mapping between the circles. The Möbius transform maps generalized circles into generalized circles on the complex plane [35]. Hence it is perfectly suited to provide a connection between the circles in our results. To see this, we first quote a lemma about the Möbius transform from [35].

Lemma 2. *[35] If a Möbius transform $f\colon \mathbb{C} \to \mathbb{C}$, given by $\omega = f(z) = \frac{e_1 z + e_2}{e_3 z + e_4}$, has two fixpoints α and ϕ, i.e. $\alpha = f(\alpha)$, $\phi = f(\phi)$, f can be written in the normal form*

$$\frac{\omega - \alpha}{\omega - \phi} = m \frac{z - \alpha}{z - \phi}, \tag{2.16}$$

where $m = \frac{e_1 + e_4 - \sqrt{D}}{e_1 + e_4 + \sqrt{D}}$, $\alpha = \frac{e_1 - e_4 + \sqrt{D}}{2e_3}$, $\phi = \frac{e_1 - e_4 - \sqrt{D}}{2e_3}$, $D = (e_1 - e_4)^2 + 4e_2 e_3$.

Applying the Möbius transform to the power control problem and assuming the equivalence of $\mathbb{R}^2$ and $\mathbb{C}$ with $(x, y) \in \mathbb{R}^2$ and $(x + jy) \in \mathbb{C}$ denoting the same point, we have the following result:

Theorem 3. *Let $2a$ denote the distance between Rx1 and Rx2. The relationship between $\mathcal{C}_1$ and $\mathcal{C}_2$ in (2.14), (2.15) can be expressed using a Möbius transform that only depends on the desired SINR ρ and a:*

$$f(z) = a \frac{(\hat{\rho}^2 + 1)z + (\hat{\rho}^2 - 1)a}{(\hat{\rho}^2 - 1)z + (\hat{\rho}^2 + 1)a}. \tag{2.17}$$

Proof. First, every point (x, y) in $\mathbb{R}^2$ corresponds to a point $z = x + jy \in \mathbb{C}$ whose conjugate is denoted by $\bar{z} = x - jy$. The circles $\mathcal{C}_1$ and $\mathcal{C}_2$ in (2.14), (2.15) can be

represented as follows:

$$\mathcal{C}_1 : A_1 z\bar{z} + \bar{B}_1 z + B_1 \bar{z} + C_1 = 0, \tag{2.18}$$

$$\mathcal{C}_2 : A_2 z\bar{z} + \bar{B}_2 z + B_2 \bar{z} + C_2 = 0, \tag{2.19}$$

where $A_1 = c^2\hat{\rho}^{-4} - 1$, $B_1 = \bar{B}_1 = -a(c^2\hat{\rho}^{-4} + 1)$, $C_1 = a^2(c^2\hat{\rho}^{-4} - 1)$; $A_2 = c^2\hat{\rho}^4 - 1$, $B_2 = \bar{B}_2 = -a(c^2\hat{\rho}^4 + 1)$, $C_2 = a^2(c^2\hat{\rho}^4 - 1), c > 0$.

To obtain the Möbius transform using Lemma 2, we need to identify two fixpoints of the transform and one pair of points that are mapped to each other. In (2.18), (2.19), as c goes to infinity, $\mathcal{C}_1$ and $\mathcal{C}_2$ will converge to the same point $(a, 0)$. Similarly, as c goes to zero, $\mathcal{C}_1$ and $\mathcal{C}_2$ will converge to the same point $(-a, 0)$. Therefore, $(a, 0), (-a, 0)$ are two fixpoints of our Möbius transform, which are actually the locations of the two receivers. For $\forall c$, assume that $z_1 = \left(a\frac{c+\hat{\rho}}{c-\hat{\rho}}, 0\right) \in \mathcal{C}_1$ is mapped to $\omega_1 = \left(a\frac{c+\hat{\rho}^{-1}}{c-\hat{\rho}^{-1}}, 0\right) \in \mathcal{C}_2$. Inserting z_1, ω_1 and two fixpoints into (2.16), we have

$$m = \frac{\omega_1 - a}{\omega_1 + a} \cdot \frac{z_1 + a}{z_1 - a}. \tag{2.20}$$

Inserting m back into (2.16), we obtain

$$\omega = f(z) = a\frac{(\hat{\rho}^2 + 1)z + (\hat{\rho}^2 - 1)a}{(\hat{\rho}^2 - 1)z + (\hat{\rho}^2 + 1)a}. \tag{2.21}$$

□

(2.21) is the Möbius transform from $\mathcal{C}_2$ to $\mathcal{C}_1$ and, conversely, $z = f^{-1}(w) = a\frac{(\hat{\rho}^2+1)\omega - (\hat{\rho}^2-1)a}{(\hat{\rho}^2+1)a - (\hat{\rho}^2-1)\omega}$ is the corresponding transform from $\mathcal{C}_1$ to $\mathcal{C}_2$. The Möbius transform obtained here can be used as a mechanism to select concurrently active links

based on the SINR requirement and the location information of the receivers. Therefore, it is very helpful for the design of MAC protocols. We will explore this in Section 2.5.

2.4 Analysis of Power Control with Peak Power Constraints

In the previous section, we only focused on the convergence condition for power control with the assumption that there are no constraints on the transmit power. However, this is not realistic due to hardware limitations and regulations. The existing power control algorithms with peak power constraint only guarantee the convergence of the transmit powers but not for the receivers' SINRs to the required values. Moreover, the impact that peak power constraints have on wireless networks is not well understood. To the best of our knowledge, no metric has been proposed to quantize the convergence of the power control algorithm when peak power constraints are present?

To solve these issues, we start with the two-transmitter case where both transmitters and receivers are restricted to the real line $\mathbb{R}$. Then, we study power control with peak power constraints for random networks and define a novel metric to measure the convergence of the power control algorithm under the peak power constraint. The properties of this novel metric are analyzed in detail.

2.4.1 Analysis of Power Levels in Linear Networks with 2 Links

For this network, the convergence condition remains the same as in (2.12). As in Section 2.3.2, if Tx1 sits on $b(d_1, \widetilde{d}_1) = c$, Tx1 is on either point $t_1 = a\frac{c-\hat{\rho}}{c+\hat{\rho}}$ or $a\frac{c+\hat{\rho}}{c-\hat{\rho}}$ for the linear network instead of a circle for two-dimensional networks. Similarly, $b(d_2, \widetilde{d}_2) = c^{-1}$ defines another two points $a\frac{c\hat{\rho}-1}{c\hat{\rho}+1}$ and $a\frac{c\hat{\rho}+1}{c\hat{\rho}-1}$. If $t_1 = a\frac{c-\hat{\rho}}{c+\hat{\rho}}$ or $a\frac{c+\hat{\rho}}{c-\hat{\rho}}$,

where $c > \hat{\rho}^{-1}$, then $t_2 \in (a\frac{c\hat{\rho}-1}{c\hat{\rho}+1}, a\frac{c\hat{\rho}+1}{c\hat{\rho}-1})$. Conversely, if $t_1 = a\frac{c-\hat{\rho}}{c+\hat{\rho}}$ or $a\frac{c+\hat{\rho}}{c-\hat{\rho}}$, where $c < \hat{\rho}^{-1}$, then $t_2 \in (a\frac{c\hat{\rho}+1}{c\hat{\rho}-1}, a\frac{c\hat{\rho}-1}{c\hat{\rho}+1})^{\mathrm{c}}$. Similar to the ROC, define the Interval of Convergence (IOC) for linear networks. Here, let $b_1 = a\frac{c\hat{\rho}-1}{c\hat{\rho}+1}$ and $b_2 = a\frac{c\hat{\rho}+1}{c\hat{\rho}-1}$. Therefore, if $c > \hat{\rho}^{-1}$, the IOC is $\mathcal{I}_1 = (b_1, b_2)$; if $c < \hat{\rho}^{-1}$, the IOC is $\mathcal{I}_2 = (b_2, b_1)^{\mathrm{c}}$. For the latter case, it means that if Tx1 and Rx1 are close enough, their link can nest inside the Tx2-Rx2 link as long as the transmit power is large enough similar to the case in Fig. 2.2(d).

Fig. 2.3 shows that the optimal power without power constraint depends on Tx2's locations given a fixed Tx1 location t_1. The IOCs highlighted in Fig. 2.3 agree with the analytical intervals $\mathcal{I}_1$ and $\mathcal{I}_2$ for different scenarios. Note that the flat part of the transmit power is due to the assumption that $h_{ij} = \min\left\{1, \left(\frac{d_0}{d_{ij}}\right)^{\gamma}\right\}$ since no receiver ever gets more power than is transmitted.

Fig. 2.3 shows the power allocations with varied Tx2 locations for some specific locations of Tx1 and given the receivers' locations. Fig. 2.3(d) resembles the case in Fig. 2.2(d) in which a short link nests within a longer one. However, with a peak power constraint, the SINR condition may not be satisfiable even if the convergence condition is met. As a result, the IOC will shrink.

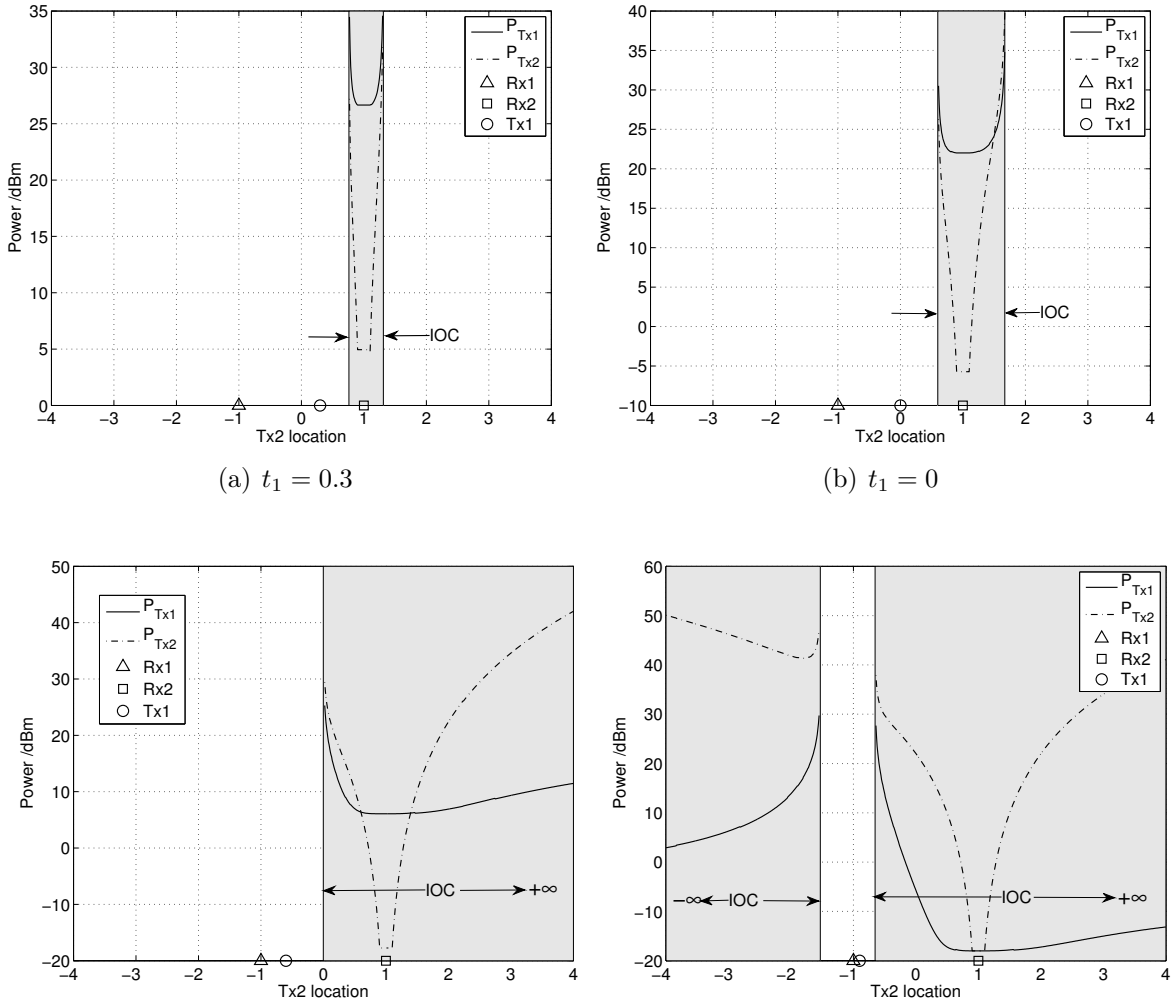

(a) $t_1 = 0.3$

(b) $t_1 = 0$

(c) $t_1 = -0.6$

(d) $t_1 = -0.9$

Figure 2.3. Optimal power for two transmitters with different Tx2 locations (the grey shadowed region indicates the IOC) for $a = 1, \gamma = 4, \rho = 12$ dB, $\eta = -30$ dBm and $d_0 = 0.1$.

2.4.2 Analysis of Peak Power Constraints in Random Networks

In this subsection, two different types of networks with random node locations are studied to illustrate how the peak power constraint affects the convergence of the power control algorithm, averaged over different network topologies.

First, we define this metric to measure the convergence when there is a peak power constraint for each node in the wireless network.

Definition 4. (Convergence Probability) The convergence probability under the power constraint $P_{\max}$ is defined as the probability that there exists a feasible power vector $P^* \leq P_{\max}$ componentwise that satisfies (2.2) for randomly located nodes in the network. It is denoted as $\mathcal{P}_{\text{con}}(P_{\max})$ or $\mathcal{P}_{\text{con}}$. For the special case where there is no power constraint, *i.e.*, $P_{\max} = \infty$, the convergence probability is denoted as $\mathcal{P}_{\text{con}}(\infty)$.

The convergence probability implies both the convergence of the transmit power and the receivers' SINR to the desired threshold. $\mathcal{P}_{\text{con}}(P_{\max})$ can be estimated by the fraction of realizations for which the power control algorithm converges under the power constraint $P_{\max}$ in simulation runs. The power update policy with power constraints is [24, 26]

$$P_i(k+1) = \min\left\{\frac{\rho}{\rho_i(k)}P_i(k), P_{\max}\right\}. \tag{2.22}$$

The convergence probability is a novel metric defined to describe the influence of the peak power constraint on the convergence of the power control algorithm and has the case without peak power constraint as a special case. It has a close connection with the standard metric *outage probability*. The convergence probability without peak power constraint can be considered as the probability that there is

no outage for any link in a wireless system with n interfering links after the power control algorithm converges. That is,

$$\mathcal{P}_{\text{con}}(\infty) = \prod_{i=1}^{n}(1 - p_{i,\text{outage}}), \tag{2.23}$$

where $p_{i,\text{outage}}$ is the outage probability for link i. Hence, the convergence probability can also be used as a metric for system design.

First, we present two general lemmas about $\mathcal{P}_{\text{con}}$.

Lemma 5. *The convergence probability $\mathcal{P}_{\text{con}}$ is a non-decreasing function of the power constraint $P_{\max}$, and its maximum is*

$$\mathcal{P}_{\text{con}}(\infty) \triangleq \mathbb{P}\left(\sigma_F < 1\right), \tag{2.24}$$

where σ_F is the Perron–Frobenius eigenvalue of the random *matrix F defined in (2.4).*

Proof. Let $P_{\max,1} < P_{\max,2}$, and

$$\begin{aligned}
\mathcal{P}_{\text{con}}(P_{\max,2}) &= \mathbb{P}(\{\exists P^* \leq P_{\max,1} \text{ s.t. (2.2) holds}\} \cup \\
&\qquad \{\exists P^* \text{ s.t. } P_{\max,1} \leq P^* \leq P_{\max,2} \text{ and (2.2) holds}\}) \quad (2.25)\\
&\geq \mathbb{P}\left(\{\exists P^* \leq P_{\max,1} \text{ s.t. (2.2) holds}\}\right) \quad (2.26)\\
&= \mathcal{P}_{\text{con}}(P_{\max,1}). \quad (2.27)
\end{aligned}$$

Therefore, it is a non-decreasing function of $P_{\max}$. As a result, its maximum is $\mathcal{P}_{\text{con}}(\infty)$. □

Note that the matrix F is a random matrix due to the random node locations. Although Lemma 5 gives an expression for $\mathcal{P}_{\text{con}}(\infty)$, there is no explicit expression

for $\mathcal{P}_{\text{con}}$ in general. However, an upper bound of the convergence probability $\mathcal{P}_{\text{con}}$ can be derived by omitting the interference in the SINR, which leads to the following lemma.

Lemma 6. *Assume that the transmitters* $\mathbf{t}_i$ *and/or the receivers* $\mathbf{r}_i$ *(*$i \in [n]$*) are randomly located within a compact set* $B \subseteq \mathbb{R}^d$ *(*$d = 1, 2$*). An upper bound of the convergence probability is given by*

$$\bar{\mathcal{P}}_{\text{con}}(P_{\max}) = \mathbb{E}\left[\mathbb{1}_{\left\{\mathbf{t}_i, \mathbf{r}_i \in B \text{ and } \|\mathbf{t}_i - \mathbf{r}_i\| \leq \Phi^{\frac{1}{\gamma}}, \quad \forall i \in [n]\right\}}\right] \tag{2.28}$$

where $\Phi = \frac{P_{\max} d_0^{\gamma}}{\rho \eta}$.

Proof. When the interference term is absent,

$$\rho_i = \frac{h_{ii} P_i}{\eta}, \quad \forall i \in [n], \tag{2.29}$$

with $P_i \leq P_{\max}$. Therefore, $\rho_{i,\max} = \frac{h_{ii} P_{\max}}{\eta}$. To satisfy the convergence condition, $\rho_{i,\max}$ must be greater than or equal to the desired SINR threshold ρ for any i, which leads to

$$\frac{\left(\frac{d_0}{d_{ii}}\right)^{\gamma} P_{\max}}{\eta} \geq \rho, \quad \forall i \in [n]. \tag{2.30}$$

By algebraic deduction, it is easily shown that (2.30) is equivalent to

$$d_{ii} \leq \Phi^{\frac{1}{\gamma}}, \quad \forall i \in [n], \tag{2.31}$$

where $\Phi = \frac{P_{\max} d_0^{\gamma}}{\rho \eta}$. With $\|\mathbf{t}_i - \mathbf{r}_i\| = d_{ii}$ and the definition of the convergence probability, we obtain (2.28). □

To obtain concrete results, we will discuss $\mathcal{P}_{\text{con}}$, $\mathcal{P}_{\text{con}}(\infty)$ and some related

bounds in the following two cases.

2.4.2.1 One-dimensional Random Networks

Assume that Tx1 is uniformly randomly placed within the interval $[-2, 0]$ and Tx2 within $[0, 2]$, and that the two receivers are fixed in $[-1, 0]$ and $[0, 1]$ respectively. Here, $B = [-2, 2]$.

The convergence probability without peak power constraints from Lemma 5 is

$$\begin{aligned} \mathcal{P}_{\text{con}}(\infty) &= \mathbb{P}\left(\sigma_F < 1\right) && (2.32) \\ &= \mathbb{P}\left(b(d_1, \widetilde{d}_1) b(d_2, \widetilde{d}_2) < 1\right) && (2.33) \\ &= \mathbb{E}_c\left[\mathbb{P}\left(b(d_2, \widetilde{d}_2) < c^{-1} \mid c = b(d_1, \widetilde{d}_1)\right)\right]. && (2.34) \end{aligned}$$

Applying the results from Section 2.4.1, $\mathbb{P}\left(b(d_2, \widetilde{d}_2) < c^{-1} \mid c = b(d_1, \widetilde{d}_1)\right)$ is $\frac{|\mathcal{I}_2 \bigcap [0,2]|}{|[0,2]|}$ for $c < \hat{\rho}^{-1}$ or $\frac{|\mathcal{I}_1 \bigcap [0,2]|}{|[0,2]|}$ for $c > \hat{\rho}^{-1}$. Note that conditioning on c is equivalent to conditioning on Tx1. Since the location of Tx1 is assumed to be uniformly distributed within $[-2, 0]$, $\mathcal{P}_{\text{con}}(\infty)$ can be expressed as

$$\mathcal{P}_{\text{con}}(\infty) = \frac{1}{2}\left(\int_{c<\hat{\rho}^{-1}} \frac{|\mathcal{I}_2 \bigcap [0,2]|}{|[0,2]|} dx + \int_{c>\hat{\rho}^{-1}} \frac{|\mathcal{I}_1 \bigcap [0,2]|}{|[0,2]|} dx\right). \tag{2.35}$$

From Lemma 6, an upper bound of the convergence probability is

$$\bar{\mathcal{P}}_{\text{con}} = \left(\frac{1}{2}\int_{|x+1| \le \min\left\{1, \Phi^{\frac{1}{\gamma}}\right\}} dx\right) \cdot \left(\frac{1}{2}\int_{|x-1| \le \min\left\{1, \Phi^{\frac{1}{\gamma}}\right\}} dx\right). \tag{2.36}$$

Basic integration results in

$$\bar{\mathcal{P}}_{\text{con}} = \min\left\{1, \Phi^{\frac{2}{\gamma}}\right\}. \tag{2.37}$$

Fig. 2.4 illustrates how the convergence probability $\mathcal{P}_{\text{con}}$ varies with the peak power constraint $P_{\max}$. The theoretical upper bound (2.37) is also given in Fig. 2.4(a). It can be seen that for small $P_{\max}$, the convergence probability increases almost quadratically with $P_{\max}$ (in dB). This region can be considered as power-limited or noise-limited since the power is so low that mainly the noise level limits the convergence. On the other hand, the convergence probability converges to a maximum asymptotically with increasing power constraint. That means the noise ceases to be a limiting factor, and the convergence probability becomes limited only by node locations, or, in other words, the interference. In this interference-limited regime, only the relative powers matter. By integrating (2.35) using the same parameters as in Fig. 2.4, we obtain $\mathcal{P}_{\text{con}}(\infty) \approx 0.93$. There is a small gap between the noise-limited and interference-limited regions as shown in Fig. 2.4(a), where both noise and interference play a significant role. Note that in the noise-limited regime, the upper bound $\bar{\mathcal{P}}_{\text{con}}$ is a good approximation for $\mathcal{P}_{\text{con}}$ while $\mathcal{P}_{\text{con}}$ coincides with $\mathcal{P}_{\text{con}}(\infty)$ in the interference-limited regime. As a result, $\min\left\{\bar{\mathcal{P}}_{\text{con}}, \mathcal{P}_{\text{con}}(\infty)\right\}$ serves as a tight upper bound and close approximation of the convergence probability $\mathcal{P}_{\text{con}}$.

Fig. 2.4(b) illustrates how the various noise levels affect the convergence probability curves. The noise-limited curves shift left as the noise level decreases while the convergence probability curves approach the same maximum $\mathcal{P}_{\text{con}}$, as expected.

2.4.2.2 Two-Dimensional Random Networks

Consider a binomial bipolar network (BBN) where receivers form a binomial point process (BPP) [33, 62] with n receivers within $B = [0, l]^2 \subset \mathbb{R}^2$, and each receiver has a dedicated transmitter randomly located around it with deterministic

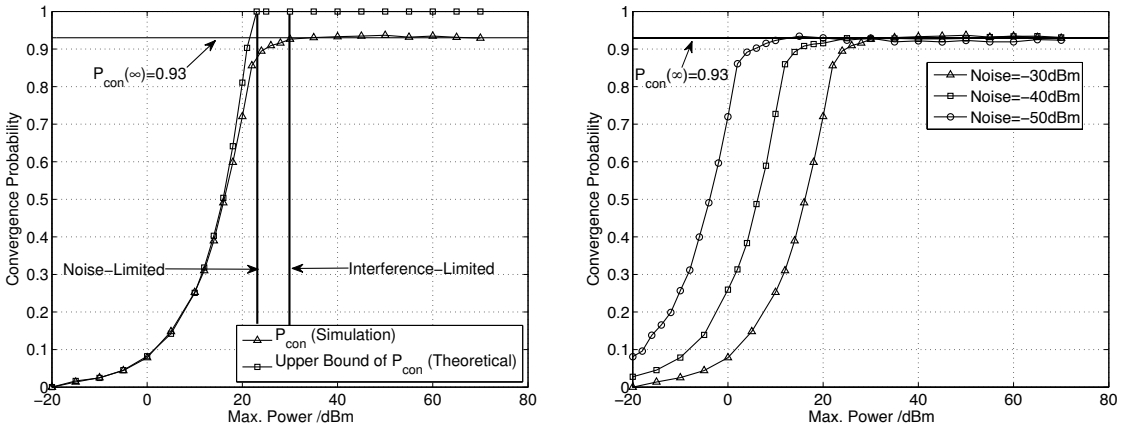

(a) Estimated $\mathcal{P}_{\text{con}}$ and its upper bound with fixed noise level -30dBm

(b) Estimated $\mathcal{P}_{\text{con}}$ at various noise levels

Figure 2.4. Estimated convergence probability $\mathcal{P}_{\text{con}}$ vs. power constraint in linear random network with 10000 realizations for $a = 1, \gamma = 4, \rho = 12$ dB.

constant link distances R. Therefore, there are n links in total.

Fig. 2.5(a) shows the estimated convergence probability from simulation with and without power constraints in a BBN. It is seen that the convergence probability decreases greatly as the number of links n increases. Also, for power constraints greater than 20 dBm, the convergence probability is almost the same as without power constraint. A reduction in the peak power may however have a drastic effect on the convergence probability. For comparison, also plotted are the cases without power control in which all transmitters use the maximum power. The cases without power control are illustrated in dashed lines. As seen, the convergence probability for the cases without power control is smaller than those with power control except for the case in which the power constraint is 10 dBm. Fig. 2.5(b) illustrates how the convergence probability varies with different power constraints

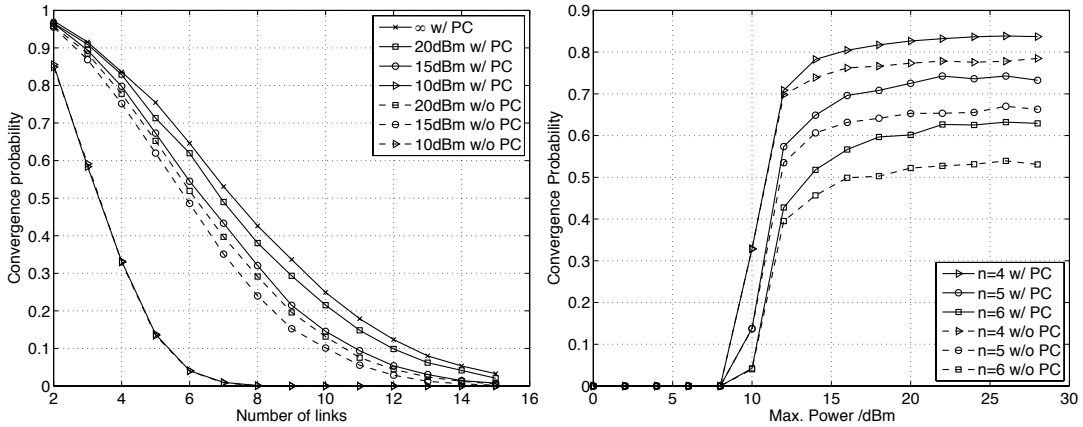

(a) Estimated convergence probability vs. number of links for different power constraints: the curves for 10 dBm overlap, i.e., at such low power, power control is ineffective since the network is noise-limited.

(b) Estimated convergence probability vs. power constraint for different number of links

Figure 2.5. Comparison of estimated convergence probability in binomial bipolar network with 10000 realizations for $\gamma = 4, \rho = 12$ dB, $R = 0.5$, $\eta = -30$ dBm, $B = [0, 10]^2$, $d_0 = 0.1$.

for a fixed number of links. The solid lines are for the cases with power control while the dashed lines without power control. Again, power control can improve the convergence probability as illustrated. The abrupt transition starting at 10 dBm comes from the assumption of a fixed transmitter-receiver distance R. Since the convergence requires that $\rho_i = \frac{h_{ii}P_i}{\sum_{i\neq j} h_{ij}P_j + \eta} \geq \rho$, omitting the interference term in the denominator we have

$$P_i \geq \rho\eta / h_{ii} = \rho\eta \left(\frac{R}{d_0}\right)^{\gamma}. \tag{2.38}$$

Therefore, the minimal power level required depends on the desired SINR, the noise level, and the channel gain even if the convergence condition is satisfied without power constraint. By inserting the parameters into the right side of

(2.38), it happens to be around 10 dBm, which explains why there is an abrupt transition of the convergence probability around 10 dBm. It also explains why the convergence probability curves are the same with or without power control for the case with power constraint 10 dBm. Besides, the convergence probabilities depend on the number of links. More links will cause more mutual interference and therefore lower the convergence probability.

Their maxima are $\mathcal{P}_{\text{con}}(\infty)$, which are computable in theory from (2.24):

$$\begin{aligned}
\mathcal{P}_{\text{con}}(\infty) &= \mathbb{E}_{\mathbf{r}_1,\mathbf{r}_2,\cdots,\mathbf{r}_n}\left[\mathbb{P}\left(\sigma_F < 1 \mid \mathbf{r}_1,\mathbf{r}_2,\cdots,\mathbf{r}_n\right)\right] && (2.39)\\
&= \mathbb{E}_{\mathbf{r}_1,\mathbf{r}_2,\cdots,\mathbf{r}_n}\left[\underbrace{\int_{\mathbb{R}^2}\cdots\int_{\mathbb{R}^2}}_{n} 1_{\{\sigma_F<1\}}\prod_{i=1}^{n} f(\mathbf{t}_i \mid \mathbf{r}_i)d\mathbf{t}_1\cdots d\mathbf{t}_n\right], && (2.40)\\
&= \mathbb{E}_{\mathbf{r}_1,\mathbf{r}_2,\cdots,\mathbf{r}_n}\left[\left(\frac{1}{2\pi}\right)^n \underbrace{\int_0^{2\pi}\cdots\int_0^{2\pi}}_{n} 1_{\{\sigma_F<1\}}d\theta_1\cdots d\theta_n\right], && (2.41)
\end{aligned}$$

where $f(\mathbf{t}_i \mid \mathbf{r}_i)$[1] is the probability density function (PDF) of the transmitter i conditional on receiver i and (2.41) is the result for $\mathbf{t}_i$ in polar coordinates.

There is no closed-form expression for $\mathcal{P}_{\text{con}}(\infty)$ for general n. For $n = 2$, we have the following proposition.

Proposition 1. *For $n = 2$, given that $\rho > 0$ and $R_0 = R\left(1+\rho^{\frac{1}{\gamma}}\right) < l$, $\mathcal{P}_{\text{con}}(\infty)$ is lower bounded by*

$$\underline{\mathcal{P}}_{\text{con}}(\infty) = 1 - \left(\frac{\pi R_0^2}{l^2} - \frac{8R_0^3}{3l^3} + \frac{R_0^4}{2l^4}\right). \tag{2.42}$$

[1]For BPP with fixed link distance, the pdf does not exist. However, the integral can be evaluated by assuming that the Tx is located on a thin annulus around the Rx of width ϵ, and then letting ϵ go to zero.

The proof is given in Appendix A.1. Since $R = 0.5$ and $\rho = 12$ dB in simulation, these conditions $\rho > 0$ and $R_0 < l$ can be guaranteed. Inserting the same parameters as in simulations, the theoretical value of $\underline{\mathcal{P}}_{\text{con}}(\infty)$ turns out to be 0.94 while the estimated $\mathcal{P}_{\text{con}}(\infty)$ in simulation is about 0.97. Hence, (2.42) serves as a tight lower bound and close approximation for $\mathcal{P}_{\text{con}}(\infty)$ for $n = 2$.

2.5 Möbius MAC Scheme

Future wireless networks are expected to accommodate a wide variety of nodes with different link distances as dictated by a large set of applications such as heterogeneous networks and cognitive networks. The cross-layer design concept, which exploits the power control technique from physical layer to improve the performance of MAC layer, has been studied in the literature [5, 19, 40, 72]. The fundamental goal is to make full use of the scarce power and bandwidth resources in a dynamic and volatile communication environment. In the following, we will work on the joint design of scheduling and power control in wireless networks with heterogeneous link distances. The newly proposed MAC scheme will combine the analysis of the peak power constraint and the Möbius transform to exploit the resources more aggressively and efficiently than the traditional CSMA scheme.

2.5.1 Model Description

Based on the observations from the Möbius transform and the analysis of the peak power constraints, we next propose a novel MAC scheme, called Möbius MAC scheme, to schedule links in pairs instead of individually. To illustrate this concept of scheduling in pairs, we consider two-tier networks that consist of two types of links, long links with link distance l_1 and short links with link distance

$l_2 < l_1$. For the long links, n points are chosen to form a BPP within the region $B = [0, l]^2 \subset \mathbb{R}^2$. Each of n points serves as the midpoint of two other points (one for transmitter and the other for receiver) that are separated by distance l_1; the orientation of the axis of the two points is uniformly chosen. The short links are placed in a similar way but have distance l_2. Assume long links have link index $i \in \{0, 1, \cdots, n-1\}$ and short links have $j \in \{n, n+1, \cdots, 2n-1\}$. Such a network model can be applied to both heterogeneous networks and cognitive networks as will be discussed in Section 2.6. One realization of the network is illustrated in Fig. 2.6.

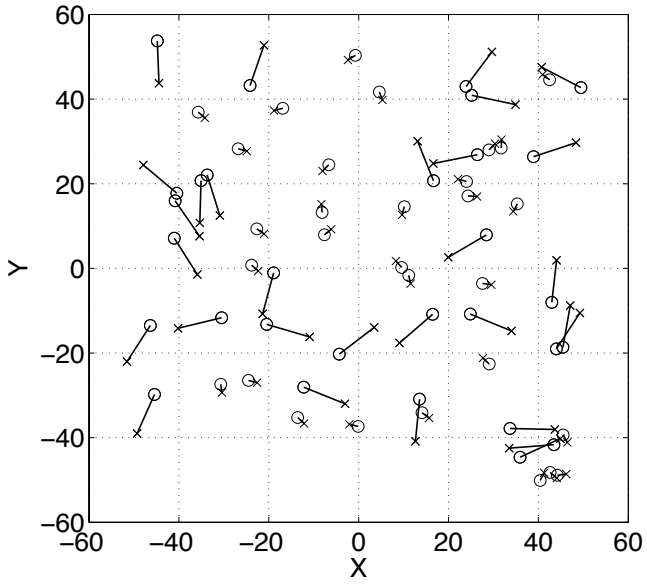

Figure 2.6. Illustration of a wireless network consisting of long and short links with $l_1 = 10$ and $l_2 = 2$ where the crosses indicate the transmitters and the circles the receivers.

2.5.2 Description of MAC Scheme

The Möbius MAC scheme operates in two stages: first the long links are scheduled using the power control algorithm with peak power constraints, and next when the set of scheduled long links is known, the short links are scheduled to be associated with their "nearest" long links if the condition established in the previous sections is satisfied. By doing so, the short links will team up with the long links and be scheduled to be active concurrently if possible, which can improve the spatial reuse greatly. The detailed description of the Möbius MAC scheme is as follows:

Algorithm 1 Möbius MAC scheme

1: The distributed power control algorithm with peak power constraint in (2.45) for a given set of n long links with initial power $P_i(0) = \rho\eta/h_{ii}$ is run;
2: If long link i's power $P_i(k) \geq p_{i,\max}$ in (2.43), link i is shut down immediately; the algorithm is run until the SINRs for the remaining long links satisfy the condition $\|\boldsymbol{\rho}(k) - \boldsymbol{\rho}^{\boldsymbol{L}}\|_\infty \leq \epsilon\rho^{\mathrm{L}}$ (ρ^{L} is given in (2.46)) for a given ϵ or the number of iterations k is greater than the maximal number of iterations $k_{\max}$; $j = n$.
3: The short link j is paired up with the long link whose receiver is closest to the transmitter of the short link, i.e., i. If the link pairs (i, j) can satisfy the constraint from Lemma 1, the short link gets assignment of its transmit power as $P_j = \min\left(\frac{P_i h_{ii}}{h_{ij}}\left(\frac{1}{\rho} - \frac{1}{\rho^{\mathrm{L}}}\right), \rho^{\mathrm{S}}\frac{P_i h_{ji}+\eta}{h_{jj}}\right)$, ($\rho^{\mathrm{S}}$ is given in (2.51)); else P_j is set to 0; $j \leftarrow j + 1$.
4: **if** $j = 2n$ **end**, **else go to** 3

As specified in Algorithm 1, the long links are scheduled first. Based on the analysis of Section 2.4 and in [63], it is beneficial to use an adjusted peak power constraint in the power control algorithm with peak power constraint with the

form in (2.22). Here, instead of using a fixed peak power constraint $P_{\max}$ as in (2.22), we choose

$$p_{i,\max} = \frac{\beta\rho\eta}{h_{ii}}, \tag{2.43}$$

where $p_{i,\max}$ is the peak power constraint for transmitter i and $\beta > 1$ is a parameter that adjusts the dynamic range of the peak power constraint. The reason why the peak power constraint in (2.43) is chosen is because under this constraint the interference at the receiver for a scheduled link can be bounded. To see that, assuming that the transmit power of transmitter i is $p_{i,\max}$, we have for the SINR at its receiver

$$\rho_i = \frac{p_{i,\max}h_{ii}}{I_i + \eta} \geq \rho, \tag{2.44}$$

which leads to $I_i \leq (\beta - 1)\,\eta$ after inserting (2.43) into (2.44), where I_i is the interference at receiver i. In cellular systems, $\beta' = \beta - 1$ is the upper bound for the Interference over Thermal (IoT) ratio[17], which is a critical parameter for system design and analysis. Hence, we can choose the parameter β based on the system requirement. All the scheduled links are guaranteed that their interference is bounded and therefore achieve the required performance. In summary, the n long links are first scheduled based on the power control algorithm with peak power constraint

$$P_i(k+1) = \min\left\{\frac{\rho^{\mathrm{L}}}{\rho_i(k)}P_i(k), p_{i,\max}\right\}, \tag{2.45}$$

with

$$\rho^{\mathrm{L}} = \rho\left(1 + \delta^{\mathrm{L}}\right), \tag{2.46}$$

and initial power $P_i\left(0\right) = \rho\eta/h_{ii}$, in which $h_{ii} = l_1^{-\gamma}$ from (2.7) is the channel power

gain between the transmitter and receiver of the long link i. Note that the positive parameter $\delta^{\mathrm{L}} \ll 1$ is used to provide protection for long links from the interference from the short links that are going to be scheduled next. This technique is similar to the active link protection used in [5]. If any long-link's transmit power is greater than or equal to $p_{i,\max}$, that link is shut down immediately. The distributed power control algorithm is run until the SINRs for the remaining links converge to a small range around ρ^{L} or the number of iterations reaches to the maximal iteration threshold. In other words, the long links "sacrifice" a little in terms of transmit power (larger SINR needs higher transmit power) in order to enable the short links to be scheduled.

Let $m \leq n$ denote the number of scheduled long links out of n from the first stage. Next, we want to know how many short links out of n can be scheduled together since it has been illustrated that link nesting is possible in Section 2.3. The short link is made to pair up with the long link whose receiver is nearest to the transmitter of the short link. Also, assume that all receivers have the location information of their associated transmitter. In this stage, if the transmitter of the short link is within the region given in Lemma 1, a proper transmit power for the short link is assigned in a way that (1) the SINR of the long link will *not* decrease from around ρ^{L} to being below the desired SINR threshold ρ; (2) the SINR of the short link should be above the SINR threshold ρ if possible.

Now, a suboptimal transmit power for the short links is derived in the following way. Ideally, any scheduled long link is supposed to satisfy

$$\frac{P_i h_{ii}}{I_i + \eta} = \rho^{\mathrm{L}}, \tag{2.47}$$

where P_i is the transmit power for transmitter i in the long link, and I_i is the

interference at the receiver i of the long link from other scheduled long links. After the short links are scheduled, we need to guarantee that

$$\frac{P_i h_{ii}}{I_i + \eta + P_j h_{ij} + \tilde{I}_i} \geq \rho, \tag{2.48}$$

where P_j is the transmit power for the transmitter j in the short link that is paired up with the long link i, h_{ij} is the channel power gain from short-link's transmitter j to long-link's receiver i, and $\tilde{I}_i$ is the interference at the long link's receiver i caused by other short-link's transmitters except short-link's transmitter j. Note that there can be multiple short links that pair up with one long link. Omitting $\tilde{I}_i$ in (2.48) and combining (2.47) and (2.48), an upper bound of P_j is obtained:

$$P_j \leq \frac{P_i h_{ii}}{h_{ij}} \left(\frac{1}{\rho} - \frac{1}{\rho^{\mathrm{L}}} \right). \tag{2.49}$$

On the other hand, in order to guarantee the SINR of the scheduled short links, we need

$$\frac{P_j h_{jj}}{P_i h_{ji} + \eta + I_j} \geq \rho^{\mathrm{S}}, \tag{2.50}$$

where

$$\rho^{\mathrm{S}} = \rho \left(1 + \delta^{\mathrm{S}} \right), \tag{2.51}$$

in which $0 < \delta^{\mathrm{S}} \ll 1$ is the margin used to protect short links from falling below the SINR threshold ρ, and h_{ji} is the channel power gain from long-link's transmitter i to short-link's receiver j, $h_{jj} = l_2^{-\gamma}$ is the channel power gain between the transmitter and receiver of the short link, and I_j is the total interference at the short link's receiver j from other links except the long-link's transmitter i.

Omitting I_j, (2.50) leads to a lower bound of P_j:

$$P_j \geq \rho^{\mathrm{S}} \frac{P_i h_{ji} + \eta}{h_{jj}}. \tag{2.52}$$

Hence, if $\rho^{\mathrm{S}} \frac{P_i h_{ji}+\eta}{h_{jj}} \leq \frac{P_i h_{ii}}{h_{ij}} \left(\frac{1}{\rho} - \frac{1}{\rho^{\mathrm{L}}}\right)$, set $P_j = \rho^{\mathrm{S}} \frac{P_i h_{ji}+\eta}{h_{jj}}$ and both SINRs for the long and short links can be above the threshold; if $\rho^{\mathrm{S}} \frac{P_i h_{ji}+\eta}{h_{jj}} > \frac{P_i h_{ii}}{h_{ij}} \left(\frac{1}{\rho} - \frac{1}{\rho^{\mathrm{L}}}\right)$, set $P_j = \frac{P_i h_{ii}}{h_{ij}} \left(\frac{1}{\rho} - \frac{1}{\rho^{\mathrm{L}}}\right)$ and the SINR of the long link can be guaranteed while the SINR of the short link may be below the threshold but make the "best effort".

2.5.3 Performance Evaluation

For the purpose of comparison, we use the CSMA scheme implemented as follows: if a receiver's interference power level is smaller than a threshold, the receiver sends a feedback signal to its transmitter to set the transmit power to be

$$P_i = \frac{(1+\delta)\,\rho\eta}{h_{ii}}, \tag{2.53}$$

where $0 < \delta \ll 1$ serves as a marginal protection to tolerate interference from other links; otherwise, it is impossible to satisfy the receiver i's SINR. The CSMA scheme is described in detail in Algorithm 2.

Algorithm 2 CSMA

1: A random timer for each link among a total of n short links and n long links is assigned; $k = 0$
2: **if** transmitter i's timer expires, receiver i calculates its received power $P_{r,i}$. If the power level $P_{r,i} < P_0$, where $P_0 = (1 + \delta)\,\eta$, link i can transmit with power given by (2.53). Link i is then admitted into the subset of links scheduled. $k = k + 1$
3: Wait for next timer expiration and **if** $k < n$ **go to** 2
4: **if** $k = n$ **end**

The key metrics for the MAC scheme are (1) how many links can be scheduled successfully in total? (2) how many long and short links can be scheduled, respectively? In order to quantify the performance of the MAC schemes, we use the *transport density* as the performance metric to combine the link distance and the number of scheduled links into one metric. Similarly to the transport capacity in [22, 31], the metric used is a variation of the transport density in [4]. The definition of transport density is as follows:

Definition 7. (Transport Density) The transport density is defined as the sum of the products of bits and the distances of all scheduled links whose SINR satisfies $\|\boldsymbol{\rho}(k) - \boldsymbol{\rho}\|_\infty \leq \epsilon$, averaged over the network realizations. It is denoted as T. Assume that all n links in a wireless network are located within a $l \times l$ region and within a time slot, a link will carry the same number of bits (W) regardless of its length as long as it can be scheduled successfully, *i.e.*, its SINR requirement can be satisfied. Then, the transport density is

$$T = \frac{W}{l^2}\mathbb{E}\left[\sum_{i=1}^{n} d_{ii}\,\mathbb{1}_{\{|\rho_i(k)-\rho|\leq\epsilon\}}\right],$$

where $\mathbb{1}_A$ is the indicator function and d_{ii} is the link distance of link i.

Its unit is bits$\cdot$m/m^2. This metric is a precise indicator of a network's capacity. For link scheduling, maximizing the transport density is more meaningful than maximizing the number of successfully scheduled links as in [64] since a longer link contributes more to the transport density than a shorter link. The transport density in this chapter can be considered as the transport capacity per unit area. Note that $\boldsymbol{\rho}(k) \to \boldsymbol{\rho}$ can only be achieved in the limit as $k \to \infty$. Therefore, it is reasonable to loosen the convergence condition to be that the error of SINRs is within some range $0 < \epsilon \ll 1$ of the target SINR, which makes it practical to implement in reality. Also, the transport density includes the relevant sub-metrics, such as link distance and convergence probability in the following way: $\lim_{k\to\infty,\epsilon\to 0} T = \lim_{k\to\infty,\epsilon\to 0} \frac{W}{l^2}\mathbb{E}\left[\sum_{i=1}^{n} d_{ii}\mathbb{1}_{\{|\rho_i(k)-\rho|\le\epsilon\}}\right] = \frac{W}{l^2}\sum_{i=1}^{n} d_{ii}\mathcal{P}\text{con}\left(p_{i,\max}\right)$. Therefore, the analysis of convergence probability in the previous section is directly related to the performance metric, transport density.

Fig. 2.7 shows the transport density of the scheduled links as a function of the total number of candidate long/short link number for the different long/short link distance ratios. As seen, the transport density for Möbius MAC is roughly twice as that of CSMA. In general, Möbius MAC always has better performance than CSMA in terms of transport density. The reason is that Möbius MAC schedules long links first and then short links while CSMA implicitly gives preference to the short links. The long links are easily prohibited from transmitting in CSMA since they would cause strong interference to others or getting easily interfered by others. This disparity could lead to a fairness problem in scheduling. Also, as the long/short link distance ratio decreases, the transport density using Möbius MAC is getting larger. On the other hand, the transport density of CSMA does not change much with the long/short link distance ratio due to the fact that all

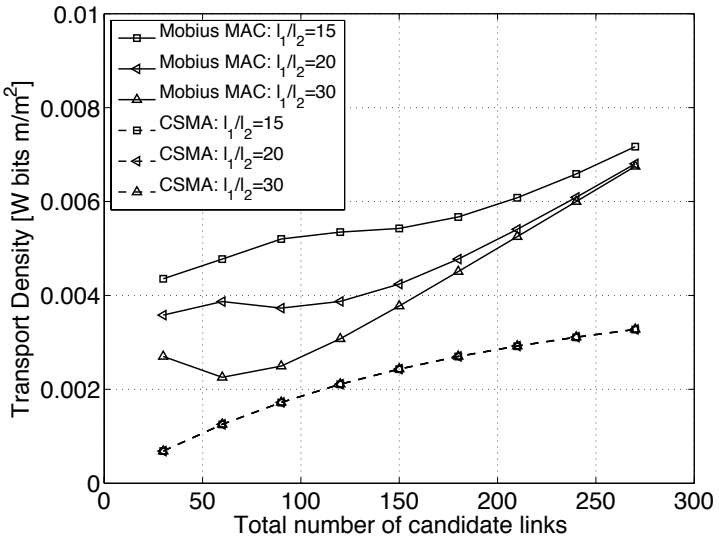

Figure 2.7. Transport density of scheduled links vs the total number of candidate long/short link with different long link distances: $l_1 = 15$, 20, 30, $l_2 = 1$, $B = [0, 200]^2$, $\gamma = 4$, $\rho = 11$ dB, $\delta = \delta^S = 0.09$, $\delta^L = 0.009$, $\beta = 50$, $\eta = -60$ dBm, $\epsilon = 1\%$, $k_{\max} = 30$.

the long links are prohibited from transmitting by CSMA.

In general, the Möbius MAC scheme can provide relatively fair scheduling or sometimes gives preference to long links while CSMA has difficulty in scheduling long links since they are easily prohibited from transmitting by short links. Moreover, the QoS performance of the scheduled links in terms of transport density by the Möbius MAC scheme is also much better than that by CSMA.

The traditional MAC schemes with or without power control usually treat different types of links, i.e. long links and short links equally without any difference. In our MAC scheme, we tried to make use of the link distance "diversity" and schedule them in a cooperative and efficient way. As a result, the performance is improved greatly. Simply speaking, the idea is to schedule long links first and then squeeze the short links between the spaces among the long links since the

short links are easily accommodated.

2.6 Applications

In this section, we will highlight two applications of our analysis and MAC scheme. One is for cognitive radio networks while the other for heterogeneous networks.

2.6.1 Application to Cognitive Radio Networks

The analysis of power levels in linear networks with two transmitters in Section 2.4.1 provides a new perspective on the spatial reuse of cognitive radios that share the spectrum with the primary users through spatial separation [48, 80].

One example is a cognitive radio network sharing spectrum with a TV broadcast system. Usually, the secondary users' locations are assumed to be outside the coverage of the TV station as illustrated in Fig. 2.8(a). However, as analyzed in Sections 2.3.2 and 2.4.1, this does not have to be the case. Assume that the power constraint for the TV station is $P_{TV,\max} = 50$ dBm and that for the secondary users is $P_{S,\max} = 20$ dBm. Fig. 2.9 shows the IOC of the TV station. The IOC bounded by the grey rectangle is the case with power constraints. Although the IOC is decreased due to the power constraints, the cognitive radio network can still find a feasible power allocation as long as the TV station is located within the power-constrained IOC. Therefore, the secondary users can still be located within the coverage of the TV station while maintaining their SINR above the threshold. Fig. 2.8(b) illustrates how this case looks in contrast to the traditional layout in Fig. 2.8(a). As shown, only the secondary users with small link distances can be tolerated within the coverage of the TV station. Short links offer the dual benefits

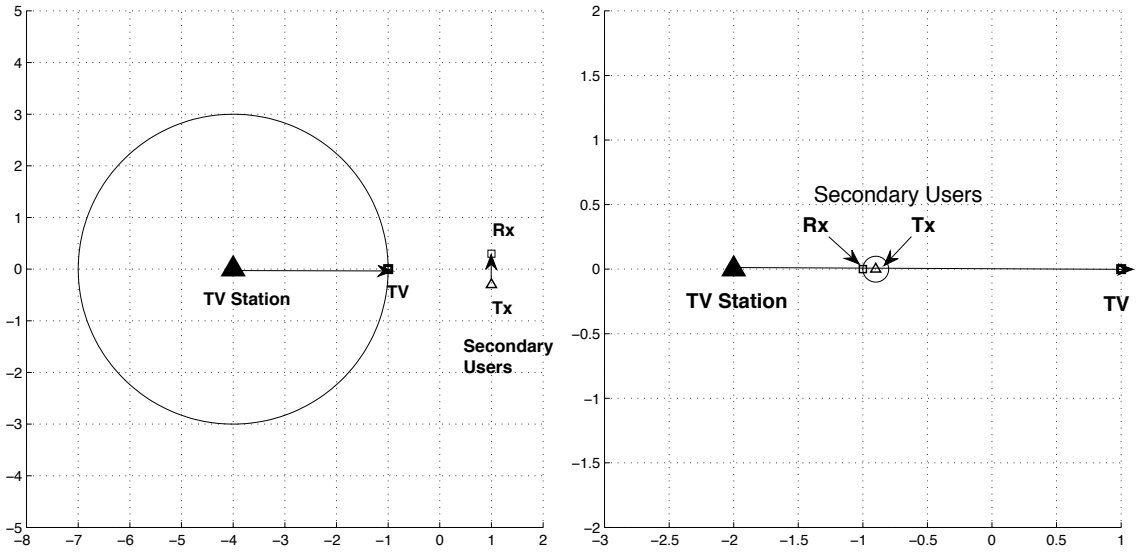

(a) Secondary users outside the coverage of TV station (b) Secondary users inside the coverage of TV station

Figure 2.8. Illustrations of spectrum sharing of a cognitive radio network with a TV broadcast system.

of higher quality links and improved spatial reuse.

The Möbius MAC scheme can readily be applied to cognitive radio networks. The primary users are scheduled first as the long links while the secondary users pair up with the "nearest" primary user and are scheduled jointly according to the criterion. The primary users' performance is always guaranteed while the secondary users "squeeze" in and make best-effort delivery whenever possible.

2.6.2 Application to Heterogeneous Cellular Networks

Another example is the concept of femtocells [9]. Femtocell deployment can improve indoor voice and data reception with the advantages of short range, low cost and low power. In this subsection, we focus on macro-femto heterogeneous

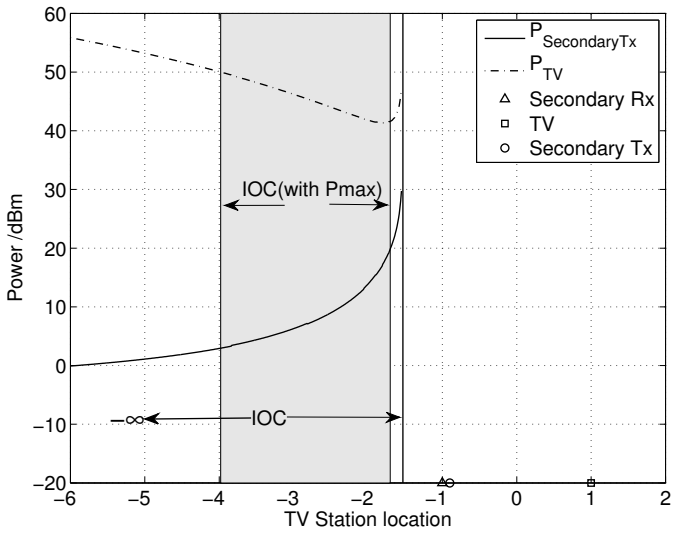

Figure 2.9. The IOC for TV station with or without power constraints (the grey shadowed region indicates the IOC with power constraints) for $a = 1, \gamma = 4, \rho = 12$ dB, $P_{TV,\max} = 50$dBm, $P_{S,\max} = 20$dBm.

networks. As illustrated in Figure 2.10, this is the scenario considered where there is a femto-cell inside a home to which only the owner has access while the user outside is barred from accessing the femto base station even if he/she is close to it. As a result, the interference caused by the femto base stations to the outside user can be severe. On the other hand, the user inside the home may experience interference from the macro base station due to its strong downlink signal strength. In general, femto networks need interference coordination via resource partitioning across base stations to manage inter-cell interference [43]. Such resource partitioning can be performed in the time domain, frequency domain, or spatial domain. However, with the geometric analysis in our chapter, it is possible to use the resources in a more aggressive way, i.e., the links between macro base station and the outside user and between the femto base station and its owner

can share the same spectrum at the same time without having to resort to spatial partitioning. Lemma 1 can serve as a criterion for the coexistence of macro-femto networks. If the geometric conditions in Lemma 1 are satisfied, the macro base station can serve as a centralized controller and choose the optimal transmit powers for itself and femto base station that can satisfy their SINR conditions ρ^{L} and ρ^{S} respectively. If the transmit powers exceed the power constraint for macro or femto base stations, they needs to be allocated to different resources and cannot share the spectrum with each other even if the geometric condition is satisfied in Lemma 1.

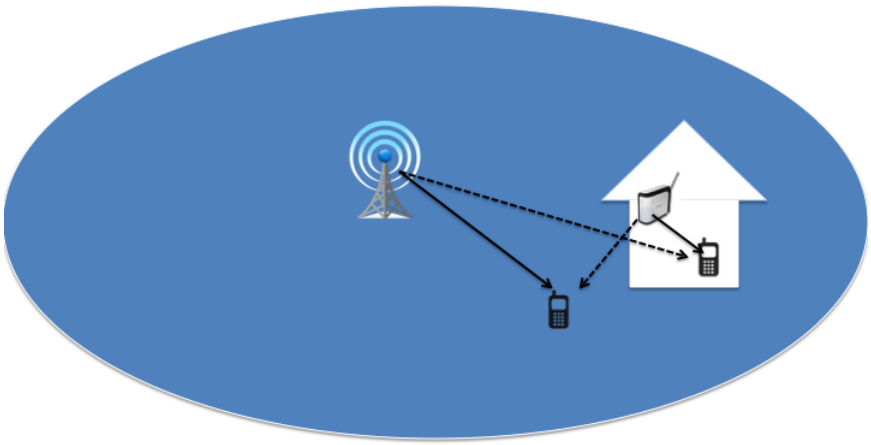

Figure 2.10. A heterogeneous network consisting of a macro and a femto base station with two mobile users where the solid lines indicate the communication links and the dashed lines the interference.

2.7 Concluding Remarks

In this chapter, we first presented a geometric analysis of the power control convergence condition. A novel analytical tool, the Möbius transform, was used to analyze the convergence conditions. The effect of peak power constraints was analyzed in detail to illustrate its influence on random networks. A novel metric, the convergence probability, has been used to study the impact of the peak power constraints.

In general, the power constraint makes the power control problem more complex. Our research provides insight into the design of MAC protocols with dynamic power control under peak power constraints. A novel MAC scheme based on Möbius transform and peak power constraints has been proposed to show that link nesting is possible under peak power constraints. It works well especially in wireless networks with unequal link distances. This is important for the design and analysis of cognitive radio networks, where the secondary users can be placed near the primary transmitter as long as the link distance of the secondary users is short enough and its transmit power is not too high, and heterogeneous networks, where the macro base stations and femto base stations are coexisting. Simulations showed that the performance of our novel MAC is twice as good as that of CSMA in terms of transport density. In summary, the MAC design combined with power control from physical layer takes full advantage of the scarce spectrum and provides a new perspective on the cross-layer design in wireless network.

CHAPTER 3

PROTOTYPE OF VIRTUAL FULL DUPLEX VIA RAPID ON-OFF-DIVISION DUPLEX

3.1 Introduction

3.1.1 Motivation

Almost all radios used in commercial and military wireless networks currently are *half-duplex (HD)*. Due to the limited dynamic range of affordable radio frequency (RF) circuits, radios cannot resolve the desired signal picked up by their receive antenna when they are overwhelmed by their own transmitted signal. A node's own transmission picked up by its own antenna is typically many orders of magnitude stronger than the desired received signal (the power ratio can be anywhere from 15 dB to 100 dB [60]). This chapter challenges the conventional wisdom of separating transmit and receive frames in time or frequency. We explore a novel *full-duplex (FD)* paradigm for the physical (PHY) layer of wireless networks based on *rapid on-off-division duplex (RODD)*[29, 76, 77].

The idea behind the RODD scheme is to let nodes follow an *on-off signaling signature* to transmit over a sequence of slots, so that the node can receive a useful signal during each off slot. A slot spans one or several symbols. Therefore, the duration of one slot is hundreds of nanoseconds to a few microseconds. Using RODD signaling, all nodes in a network can transmit and receive simultaneously over ev-

ery frame interval through their respective on-off signatures, hence achieving FD at the frame level, or *virtual* FD.

While the theoretical results in the literature motivate the use of RODD, it is unclear if RODD is suitable in reality due to practical issues, such as hardware non-idealities and power leakage caused by fast switching the signal on and off. It is also challenging to implement RODD in networks with asynchronous node behavior where nodes may randomly turn on and off, and there is non-trivial overhead involved in detecting the frame(s) of interest in the presence of background noise and interference. These issues motivate the experimental study of RODD.

The goal of this chapter is to prove the key concepts of RODD by implementing a prototype using software-defined radios and evaluating its performance. Using a combination of theory, simulation and experiments, it is shown that virtual FD can be achieved via RODD in a real wireless communication system. We also address practical implementation issues in the following sections. Since the on-off RODD signal is not continuous as the signal in traditional communication systems, it is challenging for physical layer design. Therefore, some signal processing blocks of physical layer are re-designed specially for RODD, in particular the synchronization algorithm and the channel coding scheme.

3.1.2 Main Contributions

The main contributions of this work are summarized as follows:

- We propose a simple architecture to realize a practical RODD system with two nodes.
- We implement this architecture on USRP/LabVIEW[52] and determine the bit error rate (BER).

- We design a synchronization algorithm and channel coding scheme tailored for RODD and characterize the performance.
- On this prototype, we focus on the practical issues that arise in implementing RODD. In particular, we study the transient phase of the RODD signal and investigate and calibrate the effects that on-off signaling has on the system performance.

3.1.3 Organization

The remainder of the chapter is organized as follows. In Section 3.2, we briefly summarize the fundamental idea behind RODD, its advantage over the other FD techniques, and its applications. Section 3.3 describes the system architecture proposed to implement RODD while the synchronization and coding scheme are described in detail in Sections 3.4 and 3.5. We present the simulation and experimental setup of a single-link RODD system in Sections 3.6 and 3.7. The BER curves are given and discussed together with the transients due to on-off signaling. In Section 3.8, we conclude the chapter.

3.2 RODD Theory and Applications

3.2.1 State of Art and RODD for Full Duplex

State-of-the-art MAC designs either schedule nodes orthogonally or apply a random access scheme. Random access may lead to poor efficiency while scheduling may be difficult and prone to overhead. RODD challenges the conventional paradigm of separating transmit and receive frames in time or frequency. The idea of RODD is to introduce off-slots in time within a frame of transmission through which the receiver can collect useful signals without contamination by

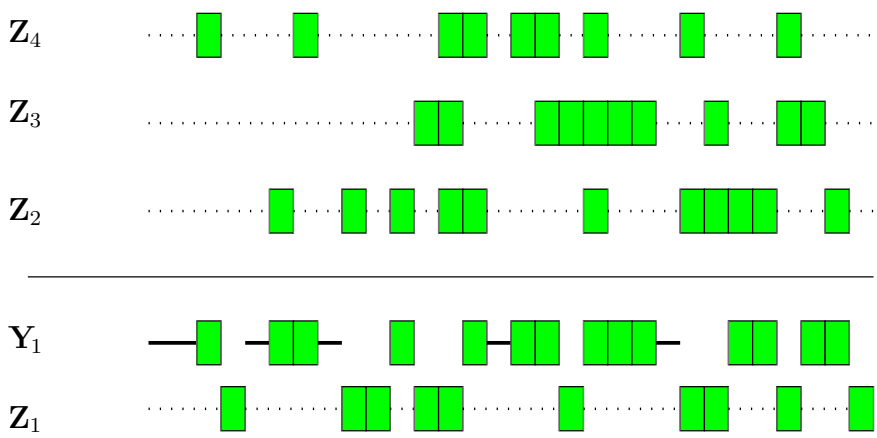

Figure 3.1. RODD signaling. $\mathbf{Z}_1, \mathbf{Z}_2, \mathbf{Z}_3, \mathbf{Z}_4$ represent the transmitted signals of node 1 through node 4, respectively, where the dotted lines represent off-slots and rectangles represent on-slots. The received signal of node 1 through its own off-slots is $\mathbf{Y}_1$, which is the superposition of $\mathbf{Z}_2$, $\mathbf{Z}_3$, and $\mathbf{Z}_4$ with erasures (blanks) at the on-slots of node 1.

self-interference. This allows a frame to be received (albeit with erasures) simultaneously as another frame is being transmitted. Hence, RODD enables half-duplex radios to achieve virtual FD communication and makes the radios to appear as FD-capable to the higher layers although they are still half-duplex at the physical layer [77].

On-off keying is a decades-old technology [54, 82]. The sub-nanosecond response time of RF circuits allows fast switching (e.g., in time-hopping impulse radios[71]), at least in principle. Fig. 3.1 illustrates RODD signals over 30 slots in a frame, where symbol-level synchronous transmission is assumed for simplicity. If no node transmits in a slot then node 1 receives a zero signal represented by a solid line. Over the period of a single RODD frame, every node can broadcast a message to its neighbors, receive a signal, and decode the messages from its neighbors at the same time. Crucial to RODD is error-control coding over a frame

of many on- and off-slots, which allows successful decoding despite erasures and superposition.

3.2.2 Advantages of Full Duplex via RODD

An alternative FD technique is to let the receive chain of a node remove the self-interference caused by the known signal from its transmit chain, so that reception can be concurrent with transmission. The idea is not new (see, e.g., [12, 41]), but has only been successfully implemented in the industrial, scientific and medical (ISM) radio bands in laboratory environments in the past few years [7, 15, 18, 38, 60]. Key to the success are novel analog and digital self-interference cancellation techniques (such as negating a wideband signal using a balanced/unbalanced transformer) as well as spatially separated (symmetric) transmit and receive antennas. We refer to this set of techniques as interference-cancellation-based FD (IC-FD), and IC-FD and virtual FD techniques are collectively referred to as FD techniques.

Each technique has its merit and weaknesses. RODD has to introduce off-slots in a frame in order to receive (which results in *virtual FD*), thus IC-FD is more efficient if the self-interference can be completely removed. However, space limitations may not allow adequate antenna separation. Also, analog cancellation with multiple transmit antennas needs specially structured and symmetric antenna placement [3, 11, 42], because it is hard to reconstruct several self-interference signals accurately from their mixture for cancellation. In such cases RODD is a more viable solution. RODD and IC-FD can also be combined to take the best of both worlds: off-slots are introduced to avoid self-interference, whereas during the on-slots the self-interference is suppressed or cancelled to yield partially useful

received signals.

3.2.3 Applications of Full Duplex via RODD

Apart from potentially doubling the throughput of a link, there are many applications for RODD: one such application is continuously cognitive radios [74]. The question of when to transmit and when to sense the channel has commanded much research effort in the area of cognitive radios. The premise that a radio cannot be cognitive during transmission, however, shall be revised if the secondary users use RODD. A virtual FD radio stays cognitive continuously, ready to abort transmissions as soon as any primary radio is sensed during its off-slots. This dramatically reduces disruption to primary users.

Many advanced network protocols require knowledge of the state of communicating parties, such as the power, modulation format, code rate, ACK, queue length, etc. Such *network state information (NSI)* is typically intended for multiple neighbors, of fewer bits than application data, and more sensitive to delay. NSI is conventionally treated similarly as data, and thus subject to contentions. As a result, the overhead of exchanging NSI often dominates the data traffic in a mobile network. RODD is ideal for NSI exchange: a frame can be reserved, in which all nodes simultaneously broadcast local NSI to their respective neighbors; each node then decodes the NSI from all neighbors at once. In fact, a new sub-layer of the protocol stack devoted to NSI can be designed based on RODD techniques. Other applications include Carrier-sensing Multiple Access (CSMA) with collision detection and instantaneous feedback (and ACK/NACK) using RODD.

3.3 Implementing an RODD system

The RODD system described in [29, 76, 77] is an ideal system with Gaussian channels and perfect synchronization. However, in a practical system, imperfect synchronization negatively affects the system performance. To implement RODD, there are several critical practical issues that need to be solved. The detailed choice and setup of the platform will be discussed in Subsection 3.3.1.

Subsection 3.3.2 will introduce the frame structure that is tailored for an RODD system. The overall implementation of our RODD system will be described in detail in Subsection 3.3.3 where each basic element in RODD system is described and the detailed implementation and their differences from traditional communication systems are covered.

The detailed implementation of synchronization scheme and channel coding for RODD system will be discussed in Sections 3.4 and 3.5 emphasizing the key issues that arise in synchronization and error-control coding and the ways we tackle them.

3.3.1 Platform

We implemented all physical layer processing for RODD by suitably modifying a novel point-to-point wireless testbed based on equipment from National Instruments (NI). The design parameters are specifically chosen based on the RODD properties. The testbed runs on NI LabVIEW on a Windows host computer. NI LabVIEW provides driver functions that interface the host computer with the NI USRP boards [52] that comprise the analog front end and the RF part.

As mentioned earlier in Section 3.2.2, the advantage of RODD over IC-FD is that for RODD, it is not necessary to put all burden on the self-interference

cancellation, which can be complicated in both hardware and software. Although the RF circuits cannot resolve the desired signal picked up by its receive antenna when it is overwhelmed by its own transmitted signal, with a carefully designed yet simple setup for the hardware, self-interference during the on-slots can be suppressed to some extent such that the desired signal during the off-slots can be resolved even with limited dynamic range. In fact, the desired signal can be picked up during the off-slots even if the self-interference in the on-slots is larger than it. Hence, the requirement for self-interference suppression is far less stringent than that for IC-FD. We implement the self-interference suppression in two ways: one way is to use a two-antenna setup. For one user, we use one antenna for the transmit RF chain to transmit on-off signals while a second antenna is used for the receive RF chain to receive the signals continuously. For example, a Tx-Rx antenna separation of about 15–20 cm results in a path loss of about 40 dB (depending on the channel characteristics). Hence, we can adjust the separation between the Tx and Rx antennas according to the link distance between the users. The two-antenna setup may look cumbersome; an alternative is to use a circulator between the Tx and Rx paths to separate the transmitted and received signal. The isolation of the circulator is usually at least 15 dB with an insertion loss of 1 dB at most, which is acceptable for our application if the link distance is short. Larger separation can be achieved by designing a simple balanced feed network using two circulators and two hybrid power combiners as in [45]. It has been shown in [45] that this technique can provide over 40 dB isolation between the transmitter and receiver channels at only 0.75 dB insertion loss for the transmitter-to-antenna and antenna-to-receiver paths. In this chapter, we present results obtained using two setups, one with two antennas and the other with one antenna

and one circulator and demonstrate that both work very well. Fig. 3.2 shows the two different setups for self-interference suppression. The baseband signal at one USRP node while transmitting a QPSK signal based on the two-antenna setup is illustrated in Fig. 3.3.

(a) Hardware setup with two antennas

(b) Hardware setup with one antenna and circulator

Figure 3.2. Two different hardware setups for self-interference suppression.

The two-antenna setup is illustrated in Fig. 3.4(b). Each USRP is equipped with two antennas, one to transmit and one to receive. The setup includes a line of sight (LOS) between Tx1 of USRP #1 and Rx2 of USRP #2 and between Tx2 of USRP #2 and Rx1 of USRP #1; the LOS paths are partially shadowed by the other antenna of each USRP. We evaluate the received signal at both Rx1 and

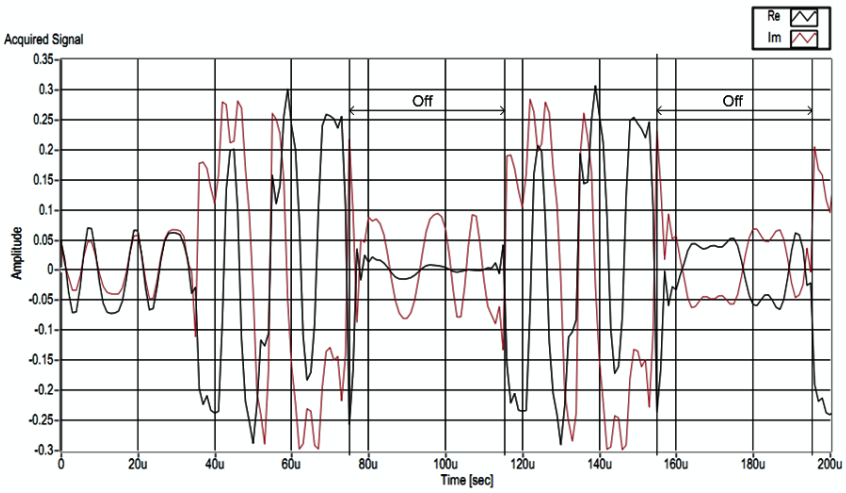

Figure 3.3. Baseband signal received at a USRP node while transmitting a QPSK signal. The carrier frequency is 915 MHz. Between 75μs and 115μs and again between 155μs and 195μs the transmit power is set to 0, so that the device can receive a BPSK signal at 250 kbit/s from another transmitter. The BPSK bits can be detected robustly even if the dynamic range between the two signals is large.

Rx2 of two USRPs for our performance measurements. USRP #2 is connected via Ethernet cable to the host, which enables the programming of the USRPs via NI LabVIEW. The setup has two modes: the unidirectional setup is used as benchmark for the RODD system where only one Tx-Rx path is used via cable connection, i.e., the Tx2 of USRP #2 is connected to Rx1 of USRP #1 via an RF cable with attenuators as shown in Fig. 3.4(a); the bidirectional mode is our normal RODD setup with antennas and transmission over the air as shown in Fig. 3.4(b). The MIMO cable is used here for clock sharing between these two USRPs such that they can be controlled to transmit and receive at the same time. The attenuators are used between the RF front end and the transmitter and receiver antennas to make the testbed operate at different signal-to-noise ratios (SNRs). The reason why attenuators are used is that even if the transmit power

gain is set to the minimal value of 0 dB, the SNR is still too high since the two USRPs are close to each other. The setup with one antenna and one circulator is illustrated in Fig. 3.4(c) where USRP #1 uses one circulator to provide at least 19 dB [20] separation between the transmit and receive signal while USRP #2 still uses the two-antenna setup as a reference.

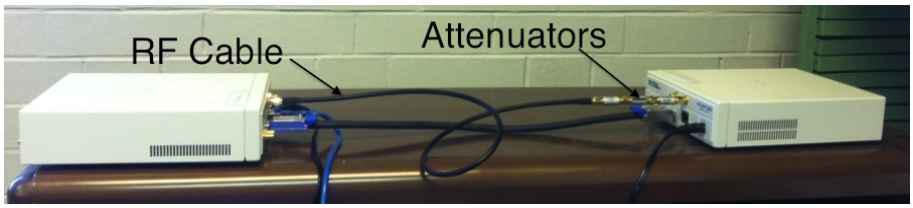

(a) Unidirectional setup

(b) Bidirectional setup with two antennas

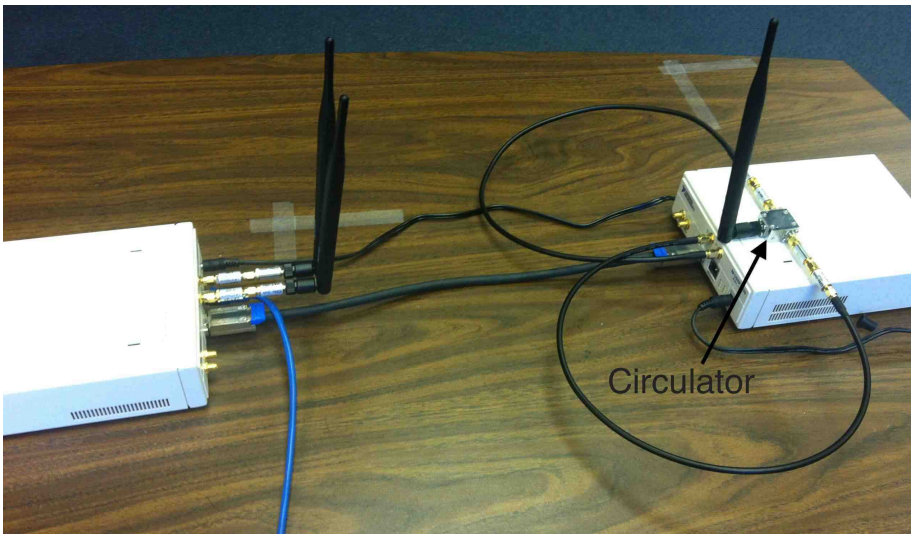

(c) Bidirectional setup with one antenna and one circulator

Figure 3.4. Setup of two NI USRPs connected via MIMO cable to each other for unidirectional and bidirectional experiments. The unidirectional setup is used to exclude the effects of self-interference, multipath propagation, and other channel impairments and serves as a benchmark for comparison with the bidirectional setup.

3.3.2 Frame Structure

Conventionally, transmissions occur in frames with continuous signals. However, a frame in an RODD system is divided into many slots as discussed earlier, and thus a special frame structure is needed. Similarly to IEEE 802.11, the frame consists of a preamble followed by a payload. The preamble consists of P identical training sequences (this is equivalent to the short training sequences in the WLAN preamble [37]), each training sequence comprising L symbols, which is specifically designed to be the same as the number of symbols in an RODD slot. By doing so, each training sequence will be assigned to exactly one on-slot during the transmission. The length of the payload M is chosen to be a multiple of the slot length L; otherwise zero padding at the end of the payload is needed. The repeated training sequences are also very helpful to the timing estimation at the receiver as discussed in detail in Section 3.4. The RODD frame structure is depicted in Fig. 3.5. Further, since the timing does not change significantly over one frame, it is sufficient to estimate the symbol timing once at the beginning of each frame.

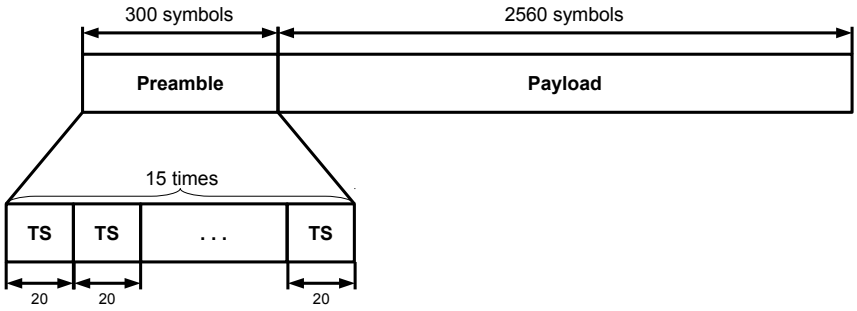

Figure 3.5. RODD frame structure where $P = 15$, $L = 20$, and $M = 2560$. TS is short for training sequence.

3.3.3 Transceiver Chain

The basic elements of the RODD transceiver chain are shown in Fig. 3.6. Between the Pulse Shaping Filter block and the channel, there are upconverter and other RF front end components which are part of the USRPs and therefore omitted in the block diagram. Similarly, between the channel and matched filter block, the signal is received by the antenna and downconverted by the USRPs. The baseband signal is fed into the Matched Filter block for processing. For this prototype we assume that each node knows the on-off signaling signature of the other node besides its own signature. This is also the assumption in [29, 76, 77]. One of the advantages of using random on-off signaling is that there is no need to coordinate different nodes to transmit in order to avoid collisions. One may argue that it is preferable to avoid collisions by using a fast TDMA scheme, at least for the two-node case. However, it is beneficial to use random on-off signaling for the multi-user case where the coordination to avoid collisions is more difficult. The two-node RODD prototype serves as a proof-of-concept and building block for the multi-user case.

3.3.3.1 Transmitter Operation

A source bit stream is first generated randomly. Another random sequence whose length equals the slot length is also generated in a similar way to serve as the training sequence in the preamble and is assumed to be known to all nodes in the system. The data payload is encoded by the channel encoder and concatenated to the preamble. The channel code is a specially designed concatenated code whose implementation is discussed in Section 3.5.

Then the frame that consists of preamble and payload enters the modulator.

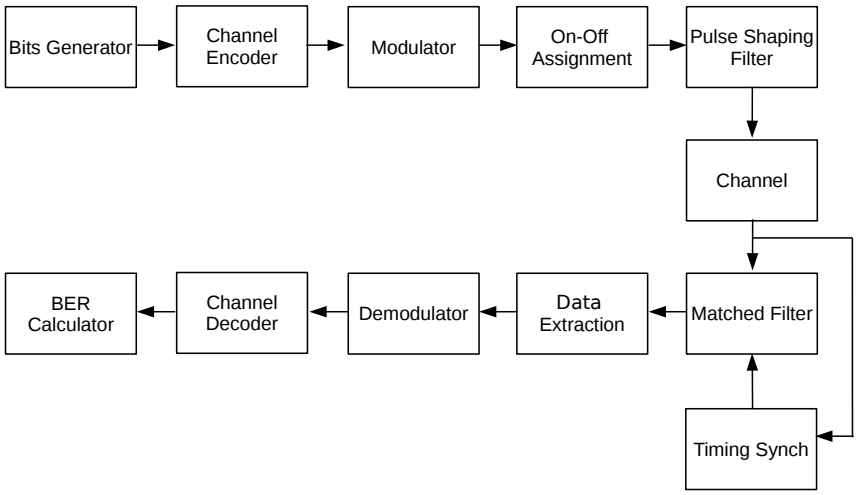

Figure 3.6. Block diagram of the RODD transceiver chain.

Different PSK constellations can be chosen, e.g. BPSK or QPSK. Alternatively, it is possible to set each constellation to operate as differential PSK. The option DBPSK is used later in our experiments since it is more robust to the phase offset introduced by hardware.

To assign the slots in one RODD frame, an on-off signature is generated in a random fashion. The signature is the same for each frame. A frame after on-off assignment is called an on-off frame. The signature is split into equally sized segments of length $\left[\frac{1}{\text{duty cycle}}\right]$, where the duty cycle is the fraction of ones in the on-off signature and $[\cdot]$ denotes rounding to the nearest integer. It may lead to insufficient on-slots if we take a purely random on-off signature with the desired length instead of the signature grouped into equally-sized segments. If the duty cycle is, e.g., 1/3, the size of one segment is 3. Within one segment, one slot is assigned randomly as on-slot while the others are assigned as off-slots. The on-off frame size is calculated as the product of the number of bits per frame and the

inverse duty cycle. With a duty cycle of 1/3, 2560 bits in payload and 15 20-bit training sequences, the on-off frame size is calculated as follows:

$$\text{on-off frame size} = (2560 + 15 \times 20)/(1/3) = 8580.$$

After the signature is generated, the data is assigned to the specified on-slots in an on-off frame. Whenever the signature is one, a slot of the modulated signal is passed to the output. For the rest of the time (when the signature has a value of zero), an array, containing only zeros, with size of one RODD slot, is passed to the output. Thus a signal with either data or zeros per slot appears at the output. Here, "zeros" means the transmitter is "sending" a null signal to allow reception from other nodes.

A pulse shaping filter is used to change the waveform of the transmitted pulses in the same way as in a conventional communication systems. The pulse shaping filter is the commonly used root raised cosine filter with rolloff factor 0.5. Although the abrupt introduction of zero symbols in off-slots will expand the bandwidth of the RODD signal, the pulse shaping filter will truncate it in the frequency domain to prevent energy leakage outside the bandwidth of the filter. Actually, we are creating a bandlimited signal, and therefore there will be power leakage from the on-slot into the off-slot in the time domain at the receiver side. We will discuss and calibrate this leakage in Section 3.7.2. At the end of the transmit chain, the generated baseband signal is sent to the USRP for transmission.

3.3.3.2 Receiver Operation

First the receiver needs to detect the starting point of the frame. An energy detector is used for frame detection while a crosscorrelation-based timing esti-

mation algorithm is designed to find the precise symbol timing information. A matched filter with parameters corresponding to the pulse shaping filter at the transmitter side is applied to the received signal followed by a decimator.

Following the decimator is the data extraction block for the non-erased on-slots. To determine which slots are non-erased, its own on-off signature is inverted and multiplied with the other node's. This way, the slots during which a signal is received without self-interference can be identified. Knowing the positions of interest, only those slots are used for further processing. The resulting signal is a truncated version of the received signal, starting at the first training sequence that has been received successfully. The preamble is used for synchronization as discussed in the following section. The actual starting point of the data is calculated using the information about the number of received preambles without erasures, which is provided by the synchronization block. The output array of the extraction block contains only the received data during the receiver's off slots without the erased data. The incoming symbols are demodulated in a hard-decision fashion to the corresponding output bits. Then the demodulated bits are sent to the channel decoder that will try to recover the erased slots based on the received data. In the end, the recovered bits will be fed into the BER calculation block to obtain the BER by comparing them to the transmitted bits.

3.4 Synchronization for RODD

There are two levels of synchronization. The first level of synchronization is that of different users. The way to synchronize different users is to let them share a common clock. For example, a MIMO cable may be used for the two-user case. As a result, different nodes can transmit and receive at the same time. Such

synchronization is not mandatory for an RODD system, as discussed in [29] but it simplifies the implementation. Although the MIMO cable synchronizes the clock of two USPRs, there is still a small frequency offset due to hardware non-idealities.

The other level of synchronization includes the timing estimation, frequency synchronization, and channel estimation. What makes the synchronization more challenging in the RODD system than in a conventional communication system is that the received signal is an on-off signal with erasures. Hence the need to design an RODD-specific synchronization algorithm. Similar to a traditional communication system, a known training sequence is needed. To avoid a packet drop due to a failed reception of the training sequence, we need to guarantee that the training sequence is received without erasure. Therefore, we adapt the preamble structure in the IEEE 802.11 standards and add it at the start of the packet as shown in Fig. 3.5. To increase the likelihood that at least one training sequence in the preamble is received without an erasure due to self-interference, we send the same training sequence P times in the preamble. Thus the probability that all training sequences collide with a node's self-interference is (duty cycle)^P. For a duty cycle of $1/3$ and $P = 15$, this probability is 7.0×10^{-8}, which is negligible.

Another feature that is specially designed for RODD is that the length of a training sequence is the same as the slot length, as discussed earlier, with the advantage that the training sequence will be assigned to exactly one on-slot, which is easy to implement. Those received training sequences in the preamble without erasure can then be used for timing estimation, frequency synchronization, and channel estimation. In the following, we mainly focus on the design of the timing estimation algorithm since the absence of frequency synchronization and channel estimation has a small impact on the performance due to the choice of differential

binary modulation and the narrow bandwidth of the system.

Even for the synchronized case where the nodes start to transmit and receive at the same time, the receivers do not know exactly when a packet starts since there is latency introduced by the data transmission from the host to the radios and back. Therefore, detecting the packets is the very first step of the successful reception and obviously of central importance for good performance.

Usually, the timing estimation consists of two main tasks: packet detection and symbol synchronization. Packet detection is the task of finding an approximate estimate of the start of the preamble of an incoming data packet. In our design, an energy detector [37] is used for packet detection for its simplicity. The energy is estimated by calculating the energy of a sliding window. The length of the sliding window is chosen to be one slot size L. If the accumulated received signal energy exceeds a certain threshold, the detector forwards the truncated signal to the next stage for symbol synchronization.

Symbol synchronization is the task of finding the precise moment of when the first symbol starts. It is achieved using a modified crosscorrelation-based timing estimation algorithm [37] since the receiver has the knowledge of the preamble, i.e., the repeated training sequences. The block diagram of the algorithm is illustrated in Fig. 3.7. In the sliding window C, the incoming signal r_n is cross-correlated with the known training sequence t_k, which is a pseudo-random sequence. P_1 and P_2 calculate the square root of the accumulated energy for r_n and t_k over a window of slot length, respectively.

The decision statistic $m_{n,2}$ is

$$m_{n,2} = \frac{|c_n|}{p_{n,1}p_{n,2}}, \tag{3.1}$$

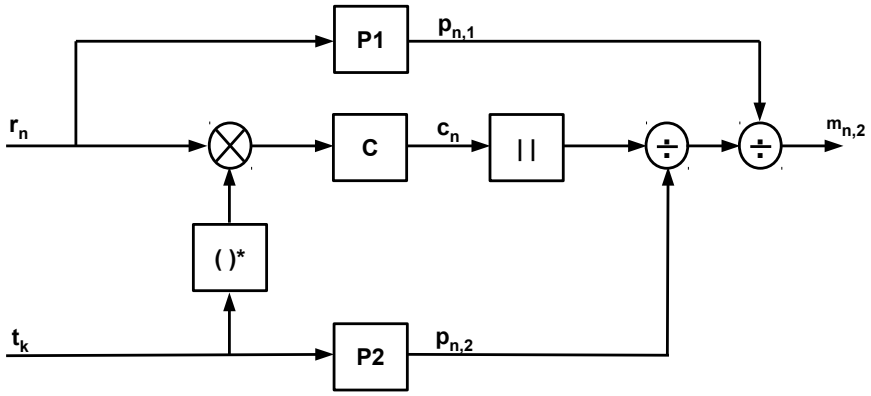

Figure 3.7. Flow graph of symbol timing estimation algorithm in the RODD system where r_n is the incoming signal and t_k is the training sequence.

where c_n is the crosscorrelation between the known training sequence and the incoming signal over a sliding window with length L and $p_{n,1}$ and $p_{n,2}$ are the square roots of the accumulated energy of the signals r_k and t_k over a sliding window with length L. Since $m_{n,2} \in [0, 1]$, it does not depend on the absolute energy level.

Finally, when the correlator output exceeds a certain threshold, which needs some fine-tuning in the simulation and experiments, it provides a coarse starting point n_s. The maximum of the next N calculated decision statistics (starting at n_s) is taken as the estimated starting point of the preamble:

$$\hat{n}_{\text{start}} = \arg\max_{n} |m_{n,2}| , \tag{3.2}$$

where $n \in \{n_s, n_s + 1, \ldots, n_s + N\}$.

As an example, the simulation resulting output $m_{n,2}$ of the synchronization is presented in Fig. 3.8. The plot shows 9 peaks that are significantly higher than the rest of the output and above the threshold. Those peaks are the remaining 9 training sequences out of $P = 15$, which are not erased by the node's self-interference. The algorithm needs at least one remaining training sequence to work quite accurately. The other peaks could be used to improve accuracy or for other purposes such as frequency estimation and channel estimation.

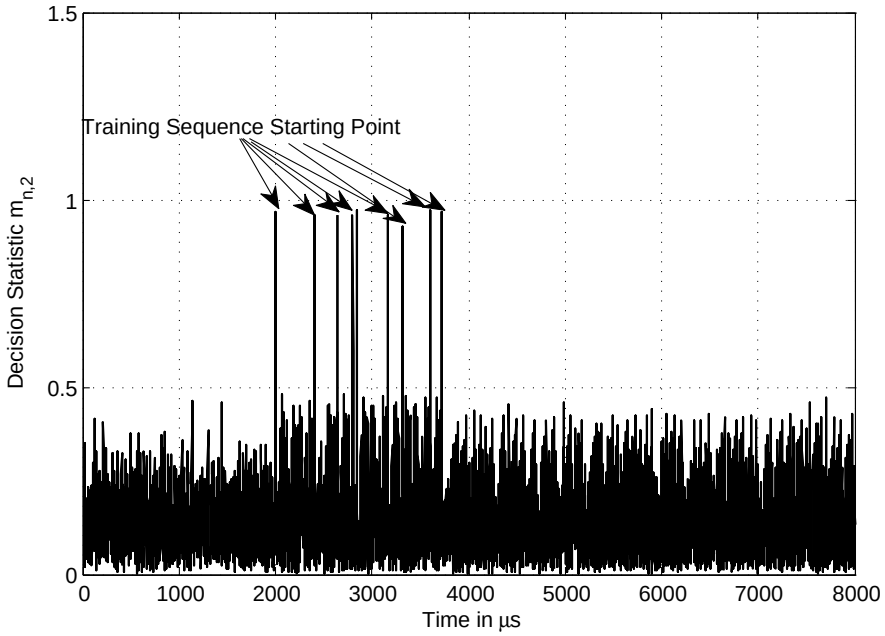

Figure 3.8. Simulation output $m_{n,2}$ of symbol timing estimation algorithm using RODD signaling with duty cycle 1/3, $P = 15$ and $\mathrm{SNR} = 15\,\mathrm{dB}$.

3.5 Channel Coding for RODD

RODD channel can be considered as a combination of erasure channel and AWGN channel. Both Cauchy Reed Solomon (Cauchy RS) code and Vandermonde Reed Solomon (Vandermonde RS) code are good codes for erasure channels. Theoretically, RS codes can detect and correct combinations of errors and erasures. In the following, we propose a concatenated code with a Vandermonde RS code as outer code and a variation of parity check as inner code to serve as the channel coding scheme in the RODD system to recover the message in presence of erasures and Gaussian noise errors.

3.5.1 Code Design

The erasures in the RODD channel are caused by self-interference at known positions to the receivers and errors due to Gaussian noise. To correct both errors and erasures, we use an inner code to detect noise errors for each non-erased on-slot and label it as an erasure and a Vandermonde RS code as an outer code to correct the erasures.

3.5.1.1 Inner Code

The inner code uses a parity bit at the end of each on-slot to detect the noise errors if there is no erasure from self-interference. Given the slot length L, the first bit of an on-slot is not used and serves as a guard bit since it does not convey any useful information due to the choice of DBPSK. The information of a symbol using DBPSK is encoded in the relative phase shift. Consequently, since the continuous signal is cut into pieces (slots), the information for the first symbol in an on slot may get lost if its previous slot gets erased. The last bit of an on-slot is

preserved as a parity bit. Since DBPSK is used, the errors tend to come in pairs. Therefore, the parity bit is chosen as the modulo-two-sum of the bits in the even-numbered-positions, i.e., the parity bit is $x_{k,L} = \left(\sum_{i=1}^{L/2-1} x_{k,2i}\right) \mod 2$, where the k^{th} on-slot consists of $[x_{k,0}, x_{k,1}, x_{k,2}, \cdots, x_{k,L-1}, x_{k,L}]$. Any two-bits-adjacent error event will affect exactly one bit in an even-numbered position and thus will be detected by a violation of the parity. Such a code can detect one error event in an on-slot. This is enough for our application since the slot length L is short.

3.5.1.2 Outer Code

The outer code is an off-the-shelf Vandermonde RS code for erasures correction. In the following, we will discuss the parameters for the outer code.

1. *Size of Data Symbol*

   The size of data symbol in an RS code decides whether the RS code can be implemented efficiently, i.e., if the RS decoder is too slow and there may be overflow since the incoming signal will be accumulated in the decoder. Since the RS codes are implemented in Galois field GF $[2^s]$, where s is the number of bits in one data symbol, a large s will incur significant computational effort. A natural choice is to choose $s = L - 2$, where L is the slot length in bits in the RODD signal. In our experiment, $L = 20$, which would make s too large. Normally, the value of s lies between 2 and 16 for efficient computation. Given the slot length $L = 20$, the size of data symbol in our RS code is chosen to be $s = 6$. As a result, there are $S = 3$ data symbols in one on-slot plus the first bit and last bit, i.e., $S \times s + 2 = L$. For different slot lengths L, the data symbol size s can be varied as long as $L - 2$ is a multiple of s.

2. *Code Rate*

For the one-link experiment with duty cycle 1/3 for the on-off signature, the channel erasure rate is 1/3. Since the erasure positions are known to the receiver, $n-k \geq \frac{1}{3}n$ leads to $\frac{k}{n} \leq \frac{2}{3}$. It means that the code rate can be at most 2/3 in this case without considering Gaussian noise. Theoretically, we can choose an RS code with code rate 2/3 for an RODD signal with duty cycle 1/3 to correct one erasure out of 3 slots on average. Therefore, the throughput can be up to $\frac{1}{3} \times \frac{2}{3} = \frac{2}{9}$ for a two-user RODD system, which is the same as that of a two-user slotted ALOHA system with transmit probability 1/3. However, the instantaneous erasure rate is a random variable with the duty cycle as its average. As a result, it is better to use a lower code rate or a variable-rate code that is based on the number of actual erasures in each frame. Here, we choose a Vandermonde RS code (n, k) as $(64, 32)$ with code rate 1/2 to provide some resilience for the RS code. The erasure rate can be higher than 1/2 with small probability, in which case the RS code cannot decode the message correctly. For a (n, k) RS code, the probability that the erasure rate is higher than k/n is

$$\begin{aligned}\mathbb{P}\left(\left\{\text{erasure rate} > \frac{k}{n}\right\}\right) &= \mathbb{P}\left(\{\text{at least } n-k \text{ slots erased}\}\right) \\ &= \sum_{i=n-k+1}^{n} \left(\frac{1}{3}\right)^{i} \left(\frac{2}{3}\right)^{n-i},\end{aligned}$$

which is 0.2% for RS $(64, 32)$. Although 0.2% is small, it will limit the coding performance if no special care is taken. Hence, in our implementation, we specifically choose the two random on-off signatures such that the erasures caused to each other will not exceed $n-k$ out of n.

3. *Noise Errors*

   The Vandermonde RS code is designed based on the assumption that the erasure locations are known. The erasures are caused by self-interference, and their locations can be derived from the random on-off signatures. However, the locations of the noise errors are unknown. Detecting noise errors is the purpose of the parity bit. It reveals if an on-slot has an error event or not. If it does, this slot is labeled as an erasure and its location is known then. In the end, we only use the on-slots that have no erasures or noise errors to recover the message. By doing so, the coding performance will be improved. For the high-SNR regime, the number of noise errors is small, and the inner code is sufficient to flag all erasures caused by the noise errors. For the low-SNR regime, it is possible that many non-erased on-slots are contaminated by noise errors and hence the decoder is forced to use some of them together with the non-erased on-slots without noise errors to decode.

4. *Other parameters*

   For an uncoded frame of length 1280 bits, there are 64 on-slots. We divide them equally into two parts and each is encoded by RS $(64, 32)$. As a result, the encoded frame length will be doubled, i.e., 2560 bits. More details about the implementation of the Vandermonde RS code can be found in [50, 59].

3.5.2 Discussion

The inner code detects the error and labels the slot as an erasure if there is one error event. There are ways to improve its performance. For example, a soft-decoder can be used for the inner decoder which would improve the performance by 0.5 to 1 dB. An alternative code is obtained by shortening the slot length from L to

$L-1$, i.e., from 20 to 19 in our experiments and use a different RS encoder/decoder that can correct both erasures and errors instead of a Vandermonde RS code. The advantage is that the redundancy in the RS code can be fully exploited. On the other hand, it requires a redesign of the frame structure. Also, the Vandermonde RS code has the advantage that the decoder can start decoding once the receiver obtains enough correct data symbols, i.e., k non-erased on-slots in RODD frame for an RS (n, k) code, which reduces the latency.

The choice of channel code is application-specific depending on the delay constraint and other system requirements. Fountain codes [8] (also known as rateless erasure codes) are a class of erasure codes with the property that a potentially infinite sequence of encoding symbols can be generated from a given set of source symbols such that the original source symbols can ideally be recovered from any subset of the encoding symbols of size equal to or only slightly larger than the number of source symbols. These codes may be particularly suitable if we apply RODD to a feedback system, in which the receiver can send an ACK back to transmitter if it receives enough symbols to decode the message. Different coding schemes will be evaluated in future work.

From a channel access perspective, RODD can be considered as a slot-level random access scheme. Its advantages over the popular MAC schemes have been discussed in [77] where the differences between RODD and CDMA, TDMA, ALOHA and CSMA are described in detail. We would like to emphasize that RODD is similar to slotted ALOHA but operates at a much faster timescale. Consequently, ALOHA cannot achieve the same throughput as RODD unless it encodes across frames in order to correct the frame erasures instead of slot erasures, which is impractical since, in that case, the receiver needs to wait for a long time (many

frames) in order to decode the coded frames. This would make the decoding delay prohibitively long. On the other hand, the decoding delay of RODD is always at most one frame interval.

3.6 Simulation Results

The purpose of the simulations is to verify the functionality of the RODD system over simulated AWGN channels. Each block in the system such as the SNR estimator, timing synchronization block, and channel coding block can be tested. In this section, simulation results and, in particular, BER versus energy per bit to noise power spectral density ratio (E_b/N_0) curves (in the following denoted as BER curves) of the RODD implementation are shown and discussed.

3.6.1 Simulation Setup

In the following we discuss the parameters that are used for the LabVIEW simulation. At the beginning of each frame we add 100 zeros to serve as guard bits between frames. The pseudo-random generated training sequence is repeated $P = 15$ times and randomly assigned to slots at the beginning of an on-off frame. One training sequence in the preamble is set to have the same length as one RODD slot. Non-coherent modulation is chosen for the experiments as well as simulation for the following reason: the real channel, in general, introduces an unknown phase-shift to the PSK signal; in these cases the differential schemes can yield a better error-rate than the coherent schemes. This is true even if two USRPs share the same clock. Further, we decided to use binary modulation because the decision regions in the constellation graph are larger than for larger constellations, e.g., QPSK or 8-PSK. The results are averaged over 10 000 runs. The absolute

transmit power level is set to 0 dBm for the simulation. The results are obtained for a simulated AWGN channel with path loss values from 61 dB to 70 dB for self-interference and from 76 dB to 85 dB for the link, respectively, while the noise level is fixed at -90 dBm. The parameters are summarized in Table 3.1.

3.6.2 Simulation Results

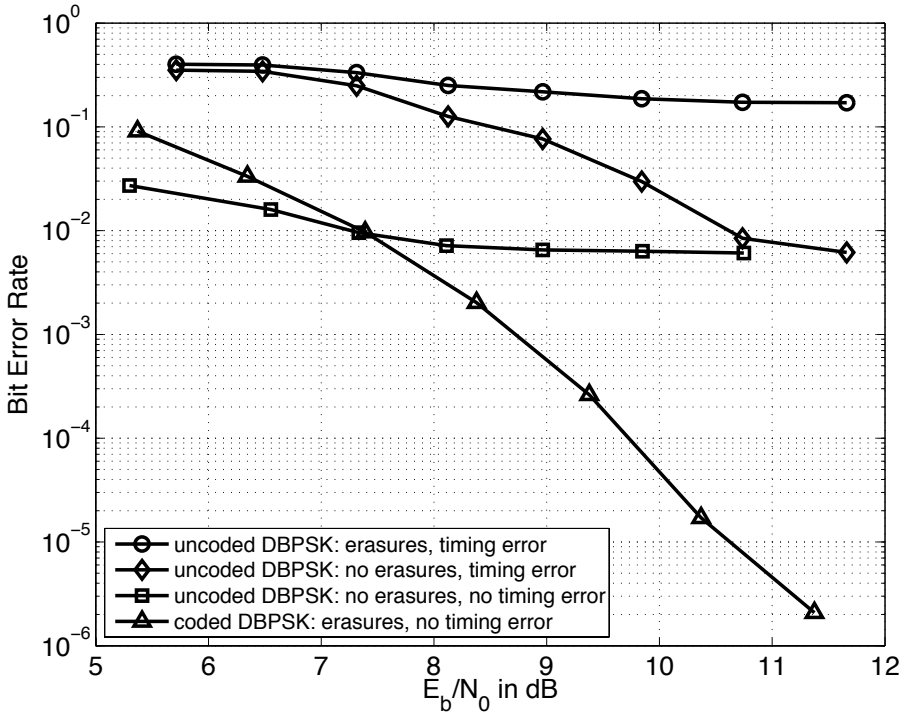

Figure 3.9. BER curves of RODD simulation.

The simulated BER curves are shown in Fig. 3.9. We observe a noticeable

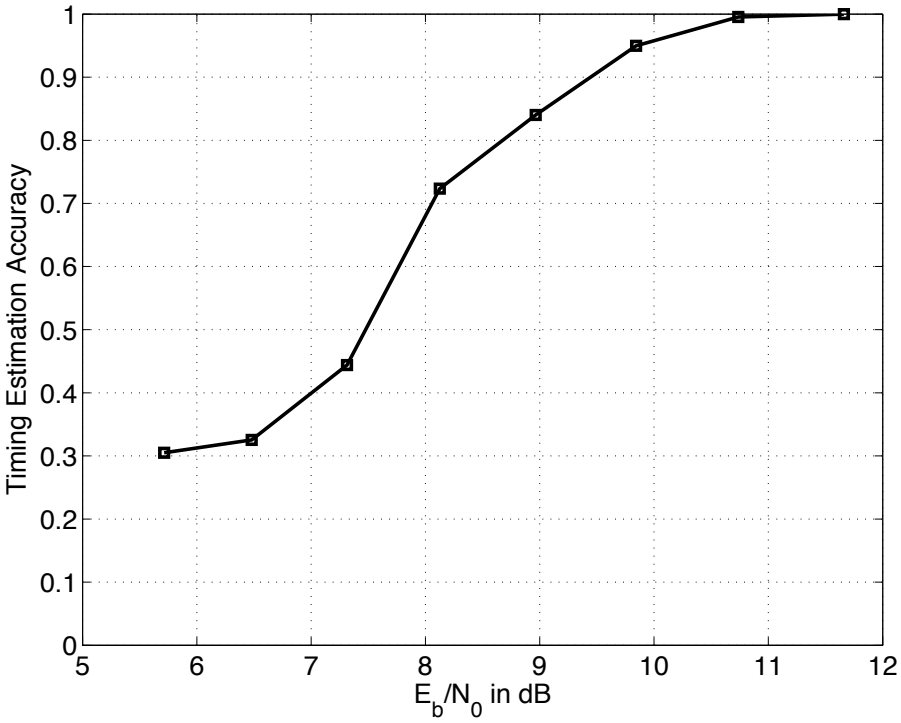

Figure 3.10. Timing estimation accuracy of RODD simulation.

difference of the uncoded BER curves compared to the coded BER curve. It is mainly due to three factors: erasures, timing errors, and first-bit inaccuracy in the on-slots due to DBPSK. The erasures have significant effects on the BER even among the different uncoded BER curves. With a 1/3 erasure rate, the uncoded BER curve with erasures has an error floor of around $\frac{1}{3} \times 50\%$, which is shown in Fig. 3.9. The coded curve shows that coding can deal with the erasures very well.

Fig. 3.10 shows the timing estimation accuracy in the simulation. Timing estimation accuracy is defined as the ratio of the number of iterations with accurate timing estimation and the total number of iterations. In the low-SNR regime, the BER difference between the uncoded and coded case is mainly caused by the timing error. For example, at an SNR of 6 dB, the timing error is about

$1 - 0.3 = 0.7$ from Fig. 3.10. When the timing is wrong, the packet will have about 50% BER. Therefore, the BER is about $0.7 \times 50\% = 0.35$, in agreement with the value from Fig. 3.9. The timing errors can be fixed by boosting the preamble power by 3 dB in the low-SNR regime, i.e. by doubling the preamble power as in [69] to achieve nearly perfect synchronization.

In the high-SNR regime, i.e., SNR greater than 10 dB, there is an error floor in the uncoded BER curves without erasures. The first bit is error-prone due to the choice of DBPSK, as discussed in Section 3.5. As a result, we ignore the first bit in a slot since it does not convey any useful information. Moreover, we will show in the following that the first bit may be distorted by the leakage from the previous slot if the previous slot is self-interference. Therefore, the first bit is reserved as a guard bit. The coded BER curve without timing errors is much better than the uncoded curves for the high-SNR regime where the timing accuracy is not an issue. Compared to the uncoded curves without timing error or erasures, the coded curve is better in the high-SNR regime and slightly worse in the low-SNR regime where the channel code can not correct all erasures due to the many noise errors.

3.7 Experimental Results

3.7.1 Setup

For the measurements on the USRP platform most of the parameters are the same as for the simulation so that the results can be compared. Some parameters are changed or additionally needed in order to meet the hardware requirements. They are discussed in the following.

The system operates in the 915 MHz ISM band with an IQ sampling rate of

800 kS/sec. The starting time for the transmitter is set to 1.2 s which is the same as that for the receiver. The reason is that the hardware initialization may take up to 1.2 s.

To measure the BER curve on the USRPs, we used two different implementations: the unidirectional mode and the bidirectional mode, as illustrated in Fig. 3.4. Comparing the two modes, we get an idea of how a node's own transmitted signal affects its receive performance. The settings for certain measured E_b/N_0 values are summarized in Tables A.1, A.2 and A.3 in Appendix A.2. For the unidirectional mode the setup illustrated in Fig. 3.4(a) is used. An RF cable is used for transmission between Tx1 of USRP #1 and Rx2 of USRP #2. The setups in Fig. 3.4(b) and Fig. 3.4(c) are used for the bidirectional mode, one with two antennas and the other with one antenna and one circulator. Hence, the bidirectional mode is additionally affected by fading or other channel impairments caused by the wireless channel and self-interference. The received signals at both receivers are evaluated. The two USRPs are connected via a MIMO cable. This connection enables the option to share the clock and is used to synchronize two users between the two USRPs as discussed earlier. Therefore the synchronization is more reliable over one frame. The second USRP uses the clock and the frequency reference of the first USRP. Note that due to hardware imperfections, there is still small a frequency offset between these two USRPs. The experiments are run to transmit 10 000 frames continuously to obtain the averaged BER values. We will focus on the performance without timing errors in experiments.

3.7.2 Transient Analysis

The rapid switching in RODD signals leads to transients that may affect the performance. In this subsection, we study the impact of these transients by taking measurements from specifically designed experiments. In particular, the goal is to determine the number of symbols that can be potentially impaired by the transients. Fig. 3.11 shows a typical on-off signal with 20 DBPSK-symbols per slot and a duty cycle of 1/3. The oversampling factor is 32 instead of 4 in order to obtain a good resolution of the signal in the time domain.

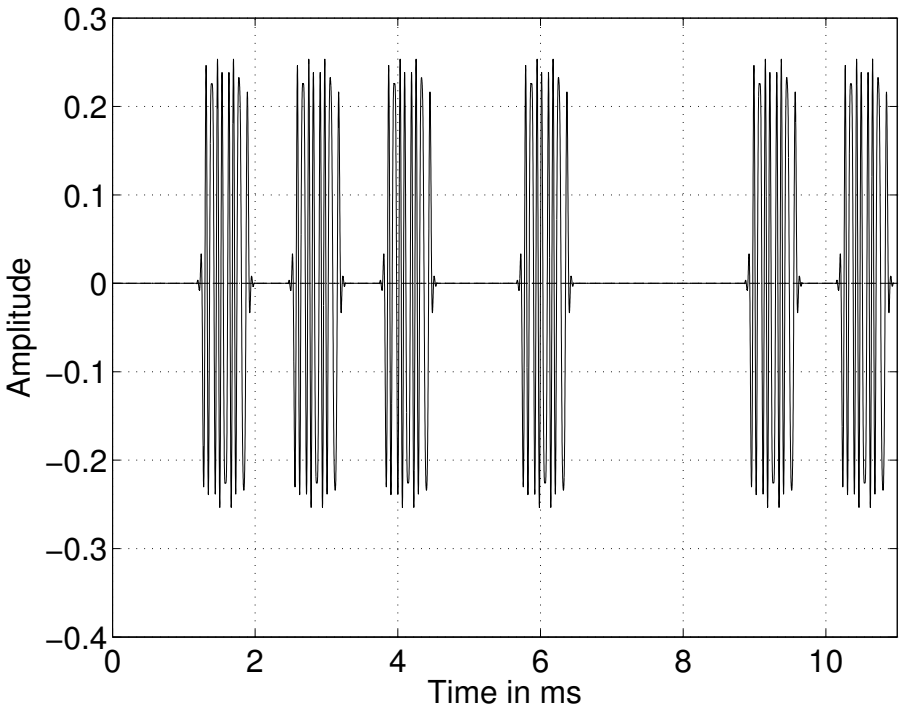

Figure 3.11. On-off signaling with 20 DBPSK symbols per RODD slot and duty cycle 1/3.

The generated signal (DBPSK symbols) is separated into on- and off-slots of certain duration (here 20 symbols). The off-slot in this sense is a period of time during which the USRP does not transmit DBPSK symbols but only null symbols. The on-slot is the time period where the USRP transmits data.

First, we examine the time of one symbol and compare it with the duration of its side lobes. The theoretical duration of one symbol is

$$T_{symbol} = \frac{32}{800\,\mathrm{kHz}} = 40\,\mu\mathrm{s}. \tag{3.3}$$

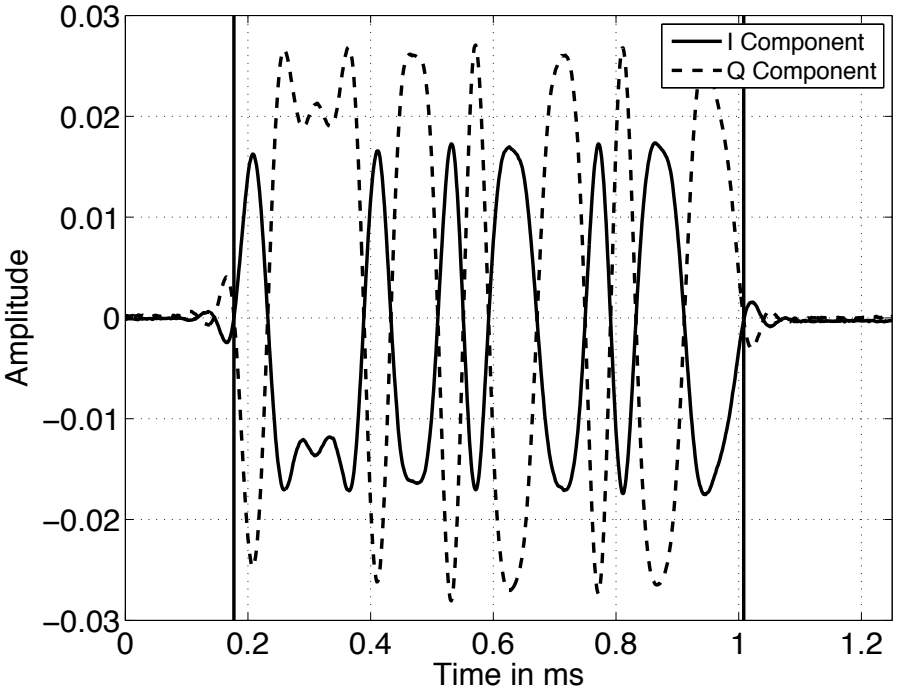

Figure 3.12. Plot of received RODD on-slot containing 20 DBPSK symbols with sampling rate 800 kHz and oversampling factor 32. The duration of the on-slot is measured to be 830 μs.

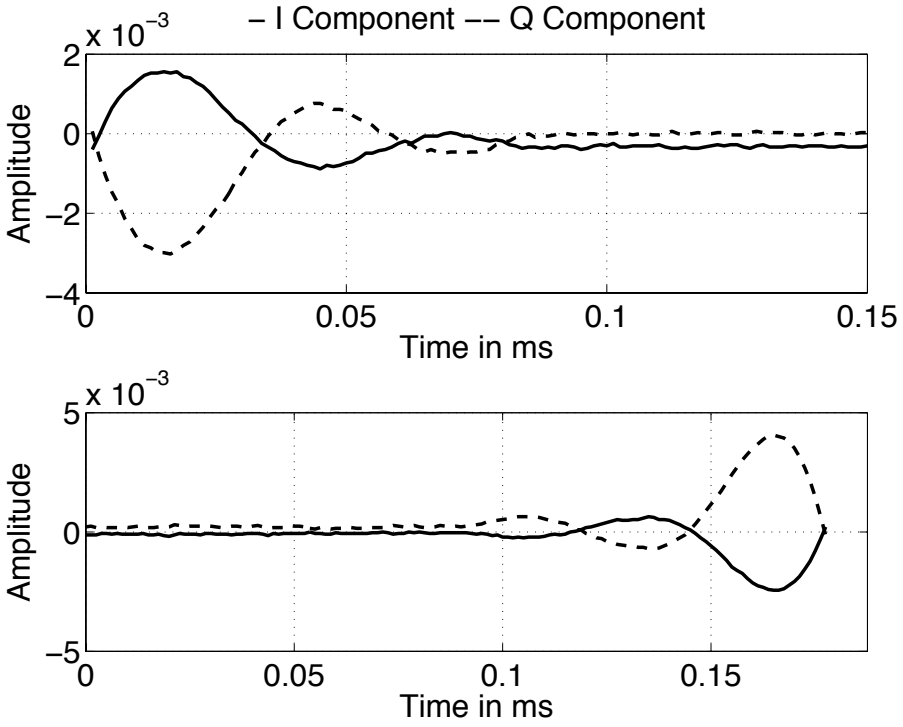

Figure 3.13. Transient between on- and off-slot (upper plot) and transient between off- and on-slot (lower plot) at Rx side.

As measuring only one symbol's duration is very inaccurate, we took the average over 20 DBPSK symbols, as shown in Fig. 3.12. The duration of the on-slot is measured without the side lobes. The starting and the end points are shown in Fig. 3.12 with black vertical lines. The on-slot was measured to last 830 μs. Therefore the duration of one symbol is 41.5 μs and thus similar to the theoretical result.

Focusing on the transient phase between on- and off-slots, Fig. 3.13 shows the transient due to the switching from an on-slot to an off-slot (upper plot) and the other way around (lower plot). The duration of the significant side lobes is

measured to be 80 μs, which is roughly two symbol durations. Examining the side lobes we see that only the first side lobe has a significant amplitude. Thus, we conclude that most parts of the side lobes disappear within one symbol duration in relation to the measured symbol duration for chosen symbol rate.

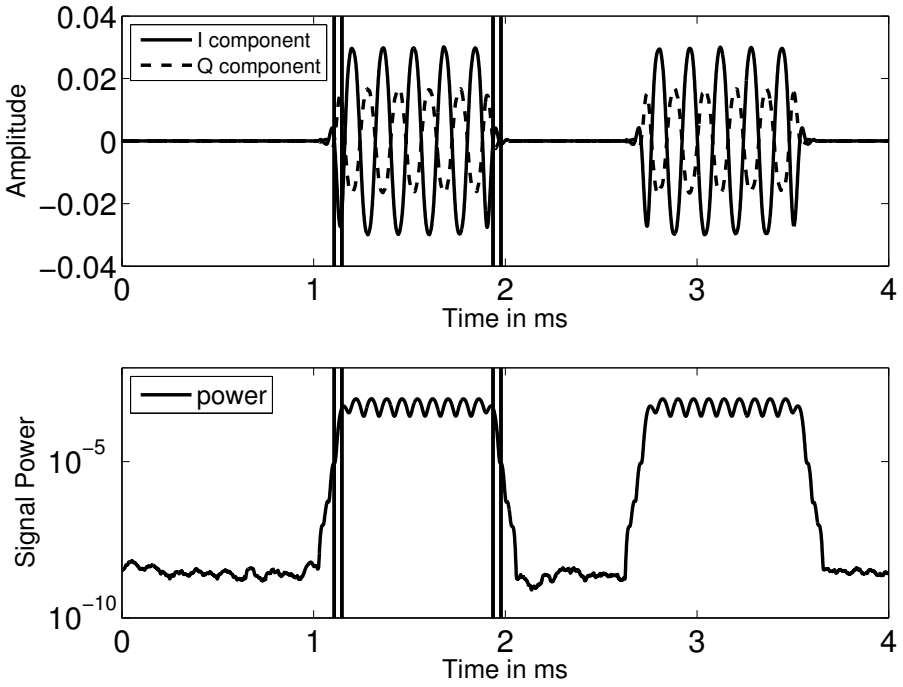

Figure 3.14. RODD signal containing two on-slots (upper plot) and estimated energy of the signal (lower plot).

To quantify the length of the transient, we examine the average received signal power during and after an on-slot. A sequence of on- and off-slots is extracted from the whole signal and plotted in Fig. 3.14 (upper plot). The average power

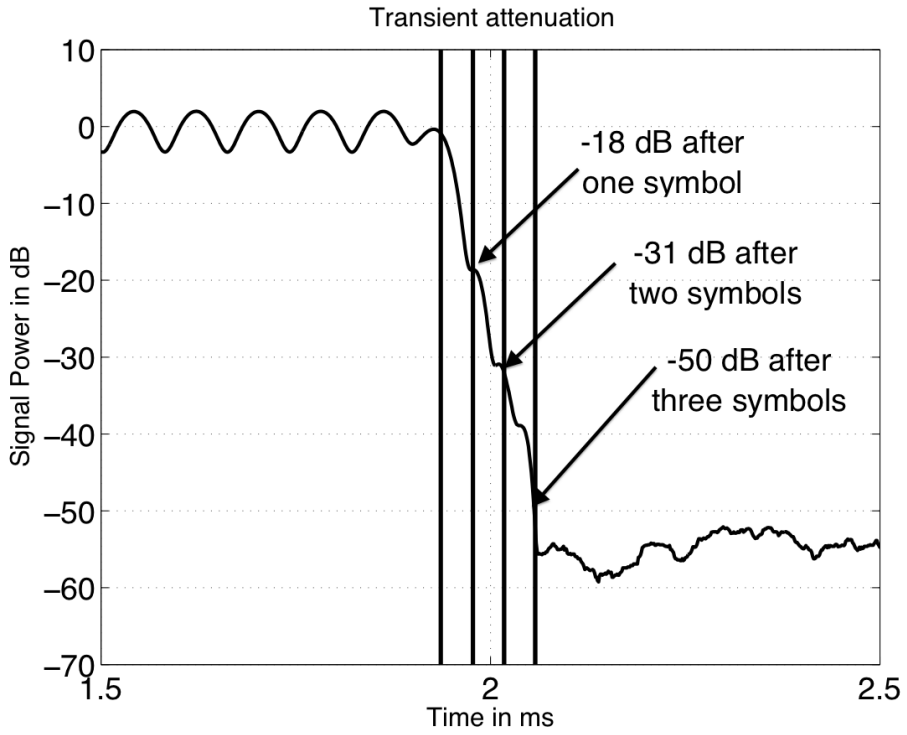

Figure 3.15. Received signal power gain at the transient from an on-slot to an off-slot. Markers are set in 32 samples distance to indicate the number of symbols after the on-slot.

for the duration of one symbol (32 samples) is calculated with a sliding window of size 32:

$$\bar{P}_k = \frac{1}{32} \sum_{i=0}^{31} |r_{k+i}|^2 \,. \tag{3.4}$$

The resulting power figure is shown in Fig. 3.14 (lower plot). The first vertical line indicates the starting point of the on-slot. The fourth vertical line is exactly 32 samples after the on-slot, i.e., one symbol duration later. To calculate the average power $\bar{P}_{on}$ over one on-slot, values starting at the second vertical line and ending at the third vertical line are used. The second vertical line is exactly 32 samples after the on-slot started. Thus the moving window is fully covered by the on-slot

at this time. The third vertical line is exactly at the end of the on-slot. We use the average power over this interval as a reference to calculate the attenuation of the following signal compared to the on-slot. To do so, we divide the estimated average power values by this value and convert the result into dB:

$$\text{gain}^{(\text{dB})} = 10 \log_{10} \left(\frac{\bar{P}_k}{\bar{P}_{on}} \right). \tag{3.5}$$

The trend of the signal power gain is illustrated in Fig. 3.15. The average power after one symbol duration is about 18 dB smaller than during the on-slot. After two symbol durations, it is about 31 dB smaller. Another symbol duration later, the power level is about 50 dB lower. The power level is beneath 50 dB during an off-slot, which is at the noise power level of -80 dBm since the signal has -10 dBm transmit power and the isolation between Tx and Rx on the same USRP is about 15 to 20 dB. In summary, as the signal power is attenuated around 18 dB after one symbol duration, we can assume that at most one symbol is affected by the transient of the RODD signaling (for the tested symbol rate). The off-slots (without the transients) are nicely silent, as required.

3.7.3 BER vs. SNR Curves

The BER is calculated only for frames with accurate timing to ensure that timing errors do not affect the results.

Fig. 3.16 compares the BER curves for the unidirectional experiment, the bidirectional experiment, and the bidirectional simulation[1]. Note that there is a point of Node 1 in bidirectional mode which is zero at 13.21 dB averaged over 10000

[1]Only one node's BER curve is plotted since the bidirectional simulation results for both nodes are very close.

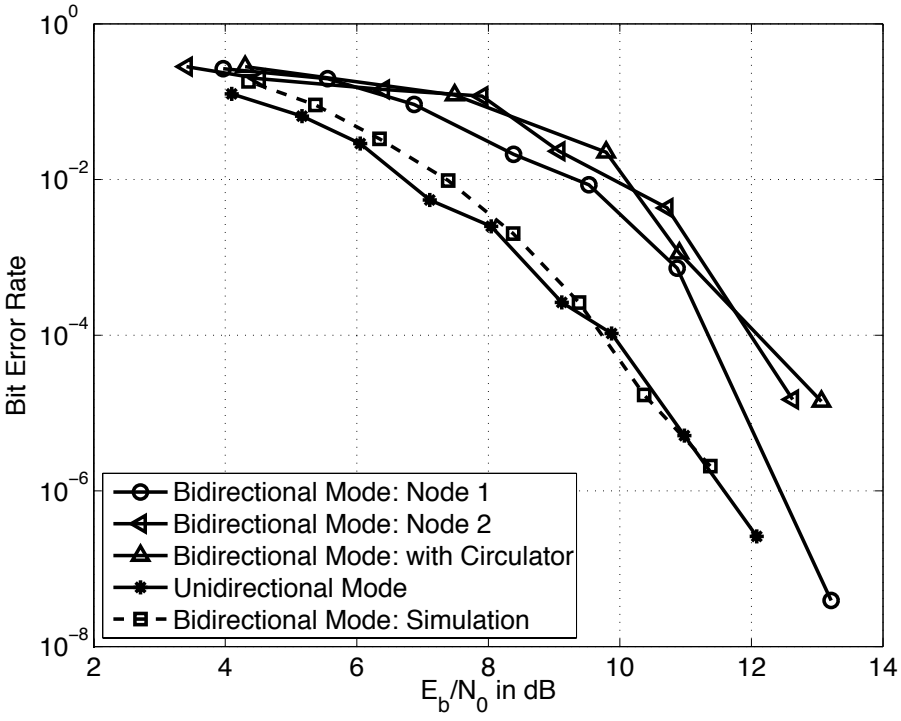

Figure 3.16. Comparison of BER curves for unidirectional and bidirectional implementation and simulation result.

runs. It means that the BER is at the level of $\frac{1}{10^4 \times 2560} = 3.91 \times 10^{-8}$ given that the frame length is 2560. The error event has extremely low probability and hence no error is reported in 10000 runs. The curve from unidirectional mode is the best since there is no self-interference in this scenario. We observe that the unidirectional mode performs better than the bidirectional mode. This is an expected result, as the self-interference as well as multipath propagation in the bidirectional mode introduce additional challenges for the system. The curves validate that the channel coding designed for RODD system is able to correct the erasures caused by the self-interference. The curve from the setup with circulator has similar performance to that from the two-antenna setup. Hence, both setups work equally

well for RODD. The setup with circulator is preferable since it only needs one antenna.

The horizontal gap between the simulation result and the measured curves has mainly two reasons. First, the simulation BER curve is obtained for an ideal AWGN channel, and the AWGN channel differs significantly from the real channel. Second, the relatively small oversampling factor can cause sample timing errors, which results in intersymbol interference.

In summary, we can conclude that the principle of on-off signaling is promising, as the shape of the measured BER curves follows the simulation curve. There is at most 2 dB difference for most of the experimental measurements in the BER performance due to the practical limitations. Therefore, it can be concluded that the USRP/LabVIEW-based prototype works quite well.

3.8 Conclusions

In this chapter, we have presented a software-radio implementation of an RODD system to achieve virtual full-duplex operation. We experimentally demonstrate that a pair of nodes can indeed communicate in a full-duplex manner at the frame level. The effects that on-off signaling has introduced have been studied and calibrated. The BER performance of unidirectional and bidirectional modes has been measured and compared with the theoretical and simulation results.

In general, it can be concluded that RODD can achieve virtual full duplex in practice. Our results suggest that RODD can indeed overcome the half-duplex constraint as predicted by the theory.

Parameter	Value
frame size M	2560 symbols
slot length L	20 symbols
N	5
duty cycle	1/3
number of repeated training sequences P	15
inner code	(19,18)
outer code	RS (64,32)
pulse shaping/matched filter	root raised cosine pulse
rolloff factor	0.5
filter length	6 symbols
oversampling factor	4
AGWN level	-90 dBm
sampling frequency	800 kHz
modulation type	DBPSK
simulated transmit power	0 dBm

TABLE 3.1

Simulation Parameters

CHAPTER 4

THROUGHPUT ANALYSIS FOR FULL-DUPLEX WIRELESS NETWORKS

4.1 Chapter Introduction

FD communication can potentially double the throughput if the self-interference can be well mitigated. FD radios have been successfully implemented in the industrial, scientific and medical (ISM) radio bands in laboratory environments in the past few years [15, 18, 38, 60]. Key to the success are novel analog and digital self-interference cancellation techniques and/or spatially separated transmit and receive antennas. A FD system with only one antenna has also been implemented in [45] by using specially designed circulator and the FD WiFi radio with one antenna and one circulator has been prototyped in [16]. In general, the main idea of FD transmission is to let the receive chain of a node remove the self-interference caused by the known signal from its transmit chain, so that reception can be concurrent with transmission. A novel signaling technique was proposed in [29] to achieve virtual FD with applications in neighbor discovery [30] and mutual broadcasting [77] with its prototyping presented in [68].

From a theoretical perspective, the two-way transmission capacity of wireless ad hoc networks has been studied in [70] for a FDD model. A FD cellular system has been analyzed in [23] where the throughput gain has been illustrated via extensive simulation for a cellular system with FD base station and HD mobile users.

The throughput gain of single-cell multiple-input and multiple-output (MIMO) wireless systems with FD radios has been quantified in [6]. A capacity analysis of FD and HD transmissions with bounded radio resources has been presented in [2] with focus only on a single-link system. [39, 44] evaluate the capacity of FD ad hoc networks and alleviate the capacity degradation due to the extra interference of FD by using beamforming and an ARQ protocol, respectively. Both capacity analyses in [39, 44] are based on perfect self-interference cancellation and the approximation that the distances of the two interfering nodes of a FD link to the desired receiver are the same.

In this chapter, the impacts of FD transmission on the network throughput are explored. On the one hand, FD transmission allows bidirectional communication between two nodes simultaneously and therefore potentially doubles the throughput. On the other hand, the extra interference caused by FD transmissions and imperfect self-interference cancellation can degrade the throughput gain over HD, which makes it unclear whether FD can actually outperform HD. this chapter utilizes the powerful analytical tools from stochastic geometry to study the throughput performance of a wireless network of nodes with both FD and HD capabilities. Our results analytically show that for an ALOHA MAC protocol, FD always outperforms HD in terms of throughput if perfect self-interference cancellation is assumed. However, for a path loss exponent α, the achievable throughput gain is upper bounded by $\frac{2\alpha}{\alpha+2}$, i.e., it ranges from 0-33% for the practical range $\alpha \in (2, 4]$. This result holds for arbitrary node densities, link distances and SIR regimes. Moreover, we model imperfect self-interference cancellation and quantify its effects on the throughput. Imperfect self-interference cancellation causes a SIR loss in the FD transmission and thus reduces the throughput gain between the FD

network and HD network. Tight bounds on the SIR loss are obtained using the concept of horizontal shifts of the SIR distribution. The amount of self-interference cancellation determines if HD or FD is preferable in the networks.

4.2 Network Model

Consider an independently marked Poisson point process (PPP) [33] $\hat{\Phi} = \{(x_i, m(x_i), s(x_i))\}$ on $\mathbb{R}^2 \times \mathbb{R}^2 \times \{0, 1, 2\}$ where the ground process $\Phi = \{x_i\}$ is a PPP with density λ and $m(x_i)$ and $s(x_i)$ are the marks of point x_i. The mark $m(x_i)$ is the location of the node that x_i communicates with. Here, we fix $\|x - m(x)\| = R$, $\forall x \in \Phi$, i.e., R is the distance of all links. Therefore, $m(x_i)$ can also be written as $m(x_i) = x_i + R\,(\cos\varphi_i, \sin\varphi_i)$, where the angles φ_i are independent and uniformly distributed on $[0, 2\pi]$. The link distance R can also be random without affecting the main conclusions since we can always derive the results by first conditioning on R and then averaging over R. We define $m(\Phi) = \{m(x) : x \in \Phi\}$, which is also a PPP of density λ. The mark $s(x_i)$ indicates the independently chosen state of the link that consists of x_i and $m(x_i)$: $s(x_i) = 0$ means the link is silent, $s(x_i) = 1$ means the link is in HD mode, and $s(x_i) = 2$ means it is in FD mode. HD means that in a given time slot the transmission is unidirectional, i.e., only from x_i to $m(x_i)$, while FD means that x_i and $m(x_i)$ are transmitting to each other concurrently. Therefore, for any link there are three states: silence, HD, and FD. Assume that a link is in the state of silence with probability p_0, HD with probability p_1 and FD with probability p_2, where $p_0 + p_1 + p_2 = 1$. p_1 and p_2 are the medium access probabilities (MAPs) for HD and FD modes, respectively. As a result, $\Phi = \bigcup_{i=0}^{2} \Phi_{[i]}$, where $\Phi_{[i]} = \{x \in \Phi : s(x) = i\}$ with density λp_i and $i \in \{0, 1, 2\}$. From the marking

theorem [33, Thm. 7.5], these three node sets $\Phi_{[i]}$ are independent. We call the link consisting of a node x_0 and its mark $m(x_0)$ as the *typical link*.

The marked point process $\hat{\Phi}$ can be used to model a wireless network of nodes with both FD and HD capabilities. The self-interference in the FD links is assumed to be cancelled imperfectly with residual self-interference-to-power ratio (SIPR) β, i.e., when the transmit power of a node is P, the residual self-interference is βP. The parameter β quantifies the amount of self-interference cancellation, and $-10\log_{10}\beta$ is the self-interference cancellation in dB. When $\beta = 0$, there is perfect self-interference cancellation, while for $\beta = 1$, there is no self-interference cancellation. An example of a realization of such a wireless network is illustrated in Figure 4.1. In the following, we will use this model to study the performance of wireless networks with FD radios.

In this network setup, we use the SIR model where a transmission attempt from x to y is considered successful if

$$\mathrm{SIR}_y = \frac{P_{xy} K h_{xy} l(x,y)}{\sum_{z\in\tilde{\Phi}\setminus\{x\}} P_{yz} K h_{yz} l(z,y) + \beta P_{xy} \mathbb{1}_{xy}^{\mathrm{FD}}} > \theta, \tag{4.1}$$

where $\tilde{\Phi}$ is the set of transmitting nodes in a given time slot, θ is the SIR threshold, h_{xy} and h_{zy} are the fading power coefficients with mean 1 from the desired transmitter x and the interferer z to y respectively, and $\mathbb{1}_{xy}^{\mathrm{FD}}$ is the indicator function that the link xy is in FD mode. The inclusion of $\mathbb{1}_{xy}^{\mathrm{FD}}$ means that the interference of FD links has an extra term due to the imperfect self-interference cancellation. The transmit powers $P_{xy} = P$ when link xy is active. We focus on the Rayleigh fading case for both the desired link and interferers. K is a unitless constant that depends on the antenna characteristics and the average channel attenuations. $K = G_{\mathrm{tx}} G_{\mathrm{rx}} \left(\frac{c_{\mathrm{L}}}{4\pi f_c}\right)^2$, where c_{L} is the speed of light, f_c is the carrier frequency, and

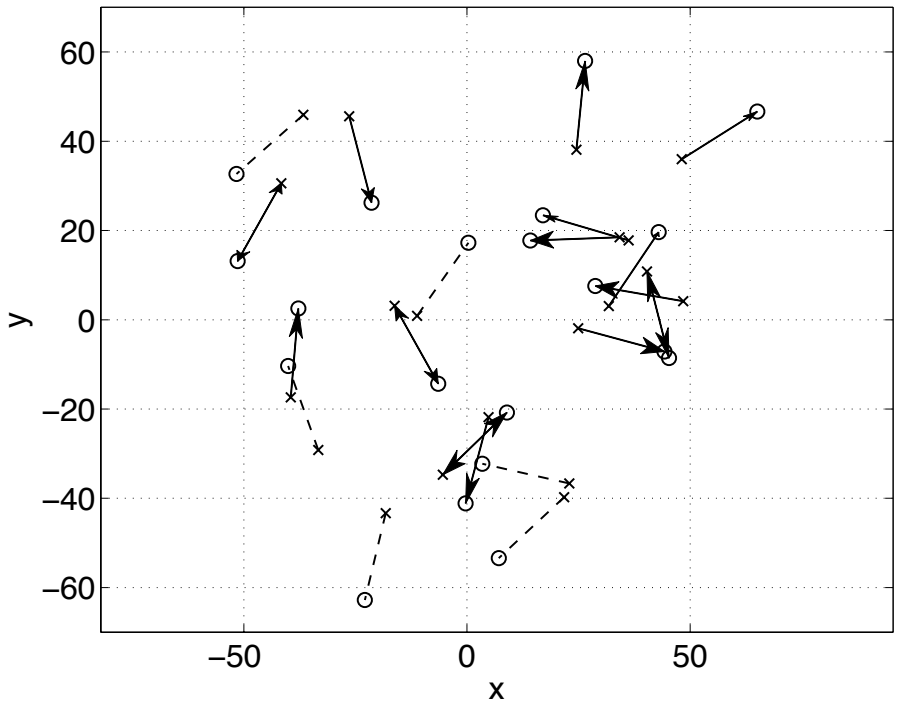

Figure 4.1. An example of the class of wireless networks considered in this chapter. The dashed lines indicate the link is silent, the arrows mean the link is in HD mode, and the double arrows in FD mode. The $\times$'s form Φ while the $\circ$'s form $m(\Phi)$.

G_{tx} and G_{rx} are the antenna gain at the transmitter and receiver, respectively. The path loss function $l(x, y)$ between node x and y is $l(x, y) = \|x - y\|^{-\alpha}$, where $\alpha > 2$ is the path-loss exponent. If y is at the origin, the index y will be omitted, i.e., $l(x, \mathbf{0}) \equiv l(x)$. Also, we call a given set of system parameters $(\lambda, \theta, R, \alpha)$ a *network configuration*. We will show that some conclusions hold regardless of the network configuration.

4.3 Success Probability

Our first metric of interest is the success probability, defined as

$$p_s \triangleq \mathbb{P}(\mathrm{SIR}_y > \theta), \tag{4.2}$$

which is also the complementary cumulative distribution function (ccdf) of the SIR. Without changing the distribution of the point process, we may assume that the receiver y is at the origin. This implies there is a transmitter at fixed distance R from the origin. The success probability plays an important role in determining the throughput, as will be described in the following section.

4.3.1 Derivation of the Success Probability and Its Bounds

Before obtaining the unconditional success probability given in (4.2), we first derive the conditional success probabilities given that a link is HD or FD[1]. We denote the success probabilities conditioning that the typical link is HD and FD as p_s^{HD} and p_s^{FD}, respectively. The following theorem gives the conditional success probabilities p_s^{HD} and p_s^{FD} of the FD/HD-mixed wireless network modeled by the marked PPP:

Theorem 8. *In a wireless network described by the marked PPP $\hat{\Phi}$, the conditional success probability p_s^{HD} is given by*

$$p_s^{\mathrm{HD}} = \exp(-\lambda p_1 H(\theta R^\alpha, \alpha)) \exp(-\lambda p_2 F(\theta R^\alpha, \alpha, R)), \tag{4.3}$$

[1]When the link is inactive, the conditional success probability is obviously zero by (4.1).

where $H(s,\alpha) \triangleq \frac{\pi^2 \delta s^\delta}{\sin(\pi\delta)}$ *with* $\delta \triangleq 2/\alpha$ *and*

$$F(s,\alpha,R) \triangleq \int_0^\infty \left(2\pi - \frac{1}{1+sr^{-\alpha}} \int_0^{2\pi} \frac{d\varphi}{1+s\left(r^2+R^2+2rR\cos\varphi\right)^{-\alpha/2}}\right) rdr, \tag{4.4}$$

and the conditional success probability p_s^{FD} *is given by*

$$p_s^{\mathrm{FD}} = \kappa p_s^{\mathrm{HD}}, \tag{4.5}$$

where $\kappa \triangleq e^{-\frac{\theta R^\alpha \beta}{K}}$.

Proof. Conditional on that the link is active, the SIR from (4.1) can be rewritten as

$$\mathrm{SIR}_y = \frac{h_{xy} l(x,y)}{\sum_{z\in\tilde{\Phi}\setminus\{x\}} h_{yz} l(z,y) + \frac{\beta \mathbb{1}_{xy}^{\mathrm{FD}}}{K}} > \theta, \tag{4.6}$$

by dividing both numerator and denumerator by PK. As a result, it is equivalent to a network where each node transmit with unit power while the SIPR β is scaled by K. Hence, with Rayleigh fading, the desired signal strength S at the receiver at the origin is exponential, i.e., $S = hR^{-\alpha}$. Conditional on that the link is HD, the interference I consists of two parts: the interference from the HD nodes $\Phi_{[1]}$ and the interference from the FD nodes $\Phi_{[2]}$. Hence, it can be expressed as:

$$I = \sum_{x\in\Phi_{[1]}} h_x l(x) + \sum_{x\in\Phi_{[2]}} \left(h_x l(x) + h_{m(x)} l(m(x))\right).$$

The Laplace transform of the interference follows as

$$\begin{aligned} L_I(s) &= \mathbb{E}e^{-s\left(\sum_{x\in\Phi_{[1]}} h_x l(x)+\sum_{x\in\Phi_{[2]}}\left(h_x l(x)+h_{m(x)}l(m(x))\right)\right)} \\ &= \mathbb{E}\left(\prod_{x\in\Phi_{[1]}} e^{-sh_x l(x)} \prod_{x\in\Phi_{[2]}} e^{-s\left(h_x l(x)+h_{m(x)}l(m(x))\right)}\right) \\ &\overset{(a)}{=} \mathbb{E}\left(\prod_{x\in\Phi_{[1]}} e^{-sh_x l(x)}\right)\mathbb{E}\left(\prod_{x\in\Phi_{[2]}} e^{-s\left(h_x l(x)+h_{m(x)}l(m(x))\right)}\right), \end{aligned} \tag{4.7}$$

where (a) follows from the fact that $\Phi_{[1]}$ and $\Phi_{[2]}$ are independent PPPs from the marking theorem [33, Thm. 7.5]. The first term in the product of (4.7) is the Laplace transform of the interference of the PPP $\Phi_{[1]}$, given by [33, page 103]:

$$\begin{aligned} L_{I_1}(s) &= \mathbb{E}\left(\prod_{x\in\Phi_{[1]}} e^{-sh_x l(x)}\right) \\ &= \exp(-\lambda p_1 H(s,\alpha)). \end{aligned}$$

The second term in the product of (4.7) can be written as follows:

$$\begin{aligned} L_{I_2}(s) &= \mathbb{E}\left(\prod_{x\in\Phi_{[2]}} e^{-s\left(h_x l(x)+h_{m(x)}l(m(x))\right)}\right) \\ &= \mathbb{E}\left(\prod_{x\in\Phi_{[2]}} \frac{1}{1+sl(x)}\frac{1}{1+sl(m(x))}\right) && (4.8) \\ &\overset{(a)}{=} \exp\left(-\lambda p_2 \int_{\mathbb{R}^2}\left(1-\frac{1}{1+sl(x)}\frac{1}{1+sl(m(x))}\right)dx\right) && (4.9) \\ &= \exp(-\lambda p_2 F(s,\alpha,R)), && (4.10) \end{aligned}$$

where (a) follows from the probability generating functional of the PPP. As a

result, the success probability is

$$p_s^{\mathrm{HD}} = L_{I_1}(\theta R^\alpha) L_{I_2}(\theta R^\alpha) \tag{4.11}$$

$$= \exp(-\lambda p_1 H(\theta R^\alpha, \alpha)) \exp(-\lambda p_2 F(\theta R^\alpha, \alpha, R)), \tag{4.12}$$

which completes the proof of p_s^{HD}.

Conditional on a FD link, there is an extra term in the interference, which is the residual self-interference scaled by the constant K. Hence, the interference for a FD link consists of three parts as follows:

$$I = \sum_{x \in \Phi_{[1]}} h_x l(x) + \sum_{x \in \Phi_{[2]}} \left(h_x l(x) + h_{m(x)} l(m(x)) \right) + \frac{\beta}{K}.$$

The first two terms are the same as in the proof of p_s^{HD} while the third term is the residual self-interference. Hence, the Laplace transform of the interference follows as

$$L_I(s) \;\; = \;\; L_{I_1}(s) L_{I_2}(s) e^{-\frac{s\beta}{K}}. \tag{4.13}$$

As a result, the conditional success probability p_s^{FD} is

$$\begin{aligned} p_s^{\mathrm{FD}} &= L_{I_1}(\theta R^\alpha) L_{I_2}(\theta R^\alpha) e^{-\frac{\theta R^\alpha \beta}{K}} \\ &= \kappa p_s^{\mathrm{HD}}, \end{aligned}$$

where the last step is from (4.11). □

Alternatively, p_s^{HD} can also be derived using the results for the Gauss-Poisson process[28].

The fact that the conditional success probability p_s^{HD} (and the Laplace transform of the interference) is a product of two terms follows from the independence of the point processes $\Phi_{[i]}$. The names of the functions H and F are chosen to reflect the fact that they represent the case of half- and full-duplex, respectively.

The residual self-interference for FD links simply adds an exponential factor to the success probability for HD links, which is similar to the effect of noise as in [33, page 105]. Theorem 8 also reveals the connection between two conditional success probability p_s^{FD} and p_s^{HD}. As expected, $p_s^{\mathrm{FD}} \leq p_s^{\mathrm{HD}}$, with equality for perfect self-interference cancellation.

The unconditional success probability can be easily obtained from the results in Theorem 8.

Corollary 9. *In a wireless network described by the marked PPP $\hat{\Phi}$, the unconditional success probability p_s is given by*

$$p_s = (p_1 + \kappa p_2)\, e^{-\lambda p_1 H(\theta R^\alpha, \alpha)} e^{-\lambda p_2 F(\theta R^\alpha, \alpha, R)}. \tag{4.14}$$

Proof. Since a link is HD with probability p_1 and FD with probability p_2, the unconditional success probability from (4.2) is the average

$$p_s = p_1 p_s^{\mathrm{HD}} + p_2 p_s^{\mathrm{FD}}. \tag{4.15}$$

Inserting the results from (4.3) and (4.5), we have (4.14). □

The (un)conditional success probabilities are not in strict closed-form due to the integral form of $F(\theta R^\alpha, \alpha, R)$. However, tight simple bounds can be obtained.

Theorem 10. *The conditional success probability p_s^{HD} is lower and upper bounded*

by

$$\underline{p}_s = \exp(-\lambda(p_1 + 2p_2)H(\theta R^\alpha, \alpha)) \tag{4.16}$$

and

$$\overline{p}_s = \exp(-\lambda(p_1 + p_2(1+\delta))H(\theta R^\alpha, \alpha)). \tag{4.17}$$

and, similarly, p_s^{FD} *is bounded as*

$$\kappa \underline{p}_s \leq p_s^{\mathrm{FD}} \leq \kappa \overline{p}_s. \tag{4.18}$$

The unconditional success probability is lower and upper bounded as

$$(p_1 + \kappa p_2)\underline{p}_s \leq p_s \leq (p_1 + \kappa p_2)\overline{p}_s. \tag{4.19}$$

Proof. Bounds only need to be established for the second term of the product in the conditional success probability that contains the integral $F(\theta R^\alpha, \alpha, R)$.

Lower Bound: From (4.9),

$$\begin{aligned} L_{I_2}(s) &= \mathbb{E}\left(\prod_{x\in\Phi_{[2]}} e^{-s\left(h_x l(x) + h_{m(x)} l(m(x))\right)}\right) \\ &\overset{(a)}{\geq} \mathbb{E}\left(\prod_{x\in\Phi_{[2]}} e^{-s h_x l(x)}\right)\mathbb{E}\left(\prod_{x\in\Phi_{[2]}} e^{-s h_{m(x)} l(m(x))}\right) \qquad (4.20) \\ &\overset{(b)}{=} \exp(-2\lambda p_2 H(s,\alpha)), \qquad (4.21) \end{aligned}$$

where (a) follows from the FKG inequality [33, Thm 10.13] since both $\prod_{x\in\Phi} e^{-s h_x l(x)}$ and $\prod_{x\in\Phi} e^{-s h_{m(x)} l(m(x))}$ are decreasing random variables. In (4.20), the first term is similar to the calculation of $L_{I_1}(s)$ with $\Phi_{[1]}$ replaced by $\Phi_{[2]}$ while in the second term, $m(\Phi_{[2]})$ is a PPP with the same density as $\Phi_{[2]}$ due to the displacement

theorem [33, page 35]. As a result, the two factors in (4.20) are equal, and

$$p_s^{\mathrm{HD}} \geq L_{I_1}(\theta R^\alpha) \exp(-2\lambda p_2 H(\theta R^\alpha, \alpha)) = \underline{p}_s.$$

Upper Bound: From (4.8),

$$\begin{aligned} L_{I_2}(s) &= \mathbb{E}\left(\prod_{x \in \Phi_{[2]}} \frac{1}{1+sl(x)} \frac{1}{1+sl(m(x))} \right) \\ &\leq \left\{ K_1(s,\alpha) K_2(s,\alpha) \right\}^{\frac{1}{2}}, \end{aligned}$$

which follows from the Cauchy-Schwarz inequality with $K_1(s,\alpha) = \mathbb{E}\left(\prod_{x \in \Phi_{[2]}} \frac{1}{(1+sl(x))^2} \right)$ and $K_2(s,\alpha) = \mathbb{E}\left(\prod_{x \in \Phi_{[2]}} \frac{1}{(1+sl(m(x)))^2} \right)$. We have

$$\begin{aligned} K_1(s,\alpha) &= \exp\left(-2\pi\lambda p_2 \int_0^\infty \left(1 - \frac{1}{(1+sr^{-\alpha})^2} \right) r dr \right) \\ &= \exp\left(-\pi\lambda p_2 (1+\delta)\Gamma(1+\delta)\Gamma(1-\delta) s^\delta \right) \\ &= \exp(-\lambda p_2 (1+\delta) H(s,\alpha)), \end{aligned}$$

where $\Gamma(\cdot)$ is the gamma function. $K_2(s,\alpha) = K_1(s,\alpha)$ because $m(\Phi_{[2]})$ is a PPP with the same density as $\Phi_{[2]}$. As a result,

$$L_{I_2}(s) \leq \left\{ K_1(s,\alpha) K_2(s,\alpha) \right\}^{\frac{1}{2}} \tag{4.22}$$

$$= \exp(-\lambda p_2 (1+\delta) H(s,\alpha)). \tag{4.23}$$

Therefore,

$$p_s^{\mathrm{HD}} \leq e^{-\lambda p_1 H(\theta R^\alpha, \alpha)} e^{-\lambda p_2 (1+\delta) H(\theta R^\alpha, \alpha)} = \overline{p}_s.$$

The lower and upper bounds of p_s^{FD} and p_s simply follow from (4.5) and (4.14). $\square$

The lower bound can be intuitively understood as lower bounding the interference of the FD nodes (which are formed by two *dependent* PPPs) by that of two *independent* PPPs with the same density.

The upper bound turns out to be the same as the result obtained by assuming $l(x) = l(m(x))$, $\forall x \in \Phi$, i.e., the distances between the receiver at the origin and the interfering pair from the FD links are the same. Indeed, assuming $l(x) = l(m(x))$, we have

$$\begin{aligned}
\tilde{L}_{I_2}(s) &= \mathbb{E}\left(\prod_{x\in\Phi_{[2]}} e^{-s\left(h_x+h_{m(x)}\right)l(x)}\right) \\
&= \exp\left(-\pi\lambda p_2 \mathbb{E}\left[\left(h_x+h_{m(x)}\right)^{\delta}\right]\Gamma\left(1-\delta\right)s^{\delta}\right) \\
&= \exp(-\pi\lambda p_2 \Gamma(2+\delta)\Gamma(1-\delta)s^{\delta}) \\
&= \exp(-\pi\lambda p_2 \left(1+\delta\right)\Gamma(1+\delta)\Gamma(1-\delta)s^{\delta}) \\
&= \exp(-\lambda p_2(1+\delta)H(s,\alpha))
\end{aligned}$$

where $\mathbb{E}\left[\left(h_x+h_y\right)^{\delta}\right] = \Gamma(2+\delta)$ since $h_x + h_y$ has an Erlang distribution and $\Gamma(2+\delta) = (1+\delta)\Gamma(1+\delta)$. Hence, the approximated success probability assuming $l(x) = l(m(x))$ is $\tilde{p}_s = L_{I_1}(\theta R^{\alpha})\tilde{L}_{I_2}(\theta R^{\alpha}) = \overline{p}_s$. This result is not surprising. The equality holds for the Cauchy-Schwarz inequality if $\prod_{x\in\Phi_{[2]}} \frac{1}{(1+sl(x))^2}$ and $\prod_{x\in\Phi_{[2]}} \frac{1}{(1+sl(m(x)))^2}$ are linearly dependent. Obviously, $l(x) = l(m(x))$ satisfies this condition. Therefore, we have $\tilde{p}_s = \overline{p}_s$ as expected.

The horizontal gap between two success probability curves (or SIR distributions) is often quite insensitive to the success probability where it is evaluated and

the path loss models, as pointed out in [27, 34]. The horizontal gap is defined as

$$G(p) \triangleq \frac{p_{s_1}^{-1}(p)}{p_{s_2}^{-1}(p)}, \quad p \in (0,1), \tag{4.24}$$

where $p_s^{-1}(p)$ is the inverse of the success probability and p is the target success probability. The sharpness of the upper and lower bounds of the success probabilities is established by the following corollary.

Corollary 11. *The horizontal gap between the upper and lower bound of the conditional success probability p_s^{HD} does not depend on the target success probability and is given by*

$$G = \left(\frac{p_1 + 2p_2}{p_1 + p_2(1+\delta)}\right)^{1/\delta}. \tag{4.25}$$

Furthermore, the horizontal gap between the lower and upper bound of the conditional success probability p_s^{FD} and the bounds of the unconditional success probability p_s under perfect self-interference cancellation is also G.

Proof. The horizontal gap can be obtained by setting $\overline{p}_s(\overline{\theta}) = \underline{p}_s(\underline{\theta})$ and calculating $G = \overline{\theta}/\underline{\theta}$. From (4.16) and (4.17), we have

$$\exp(-\lambda(p_1 + 2p_2)H(\overline{\theta}R^{\alpha}, \alpha)) = \exp(-\lambda(p_1 + p_2(1+\delta))H(\underline{\theta}R^{\alpha}, \alpha)). \tag{4.26}$$

Solving the above equation for the ratio $\overline{\theta}/\underline{\theta}$, we obtain (4.25). When the self-interference cancellation is perfect, $\kappa = 1$. From (4.18) and (4.19), we obtain the same horizontal gap G for p_s^{FD} and p_s. □

From the above corollary, it is apparent that the gap G is independent of the SIR threshold θ and the target success probability; it only depends on δ and the transmit probabilities. Also, for $\alpha \downarrow 2$, $G \downarrow 1$. Figure 4.2 plots the unconditional

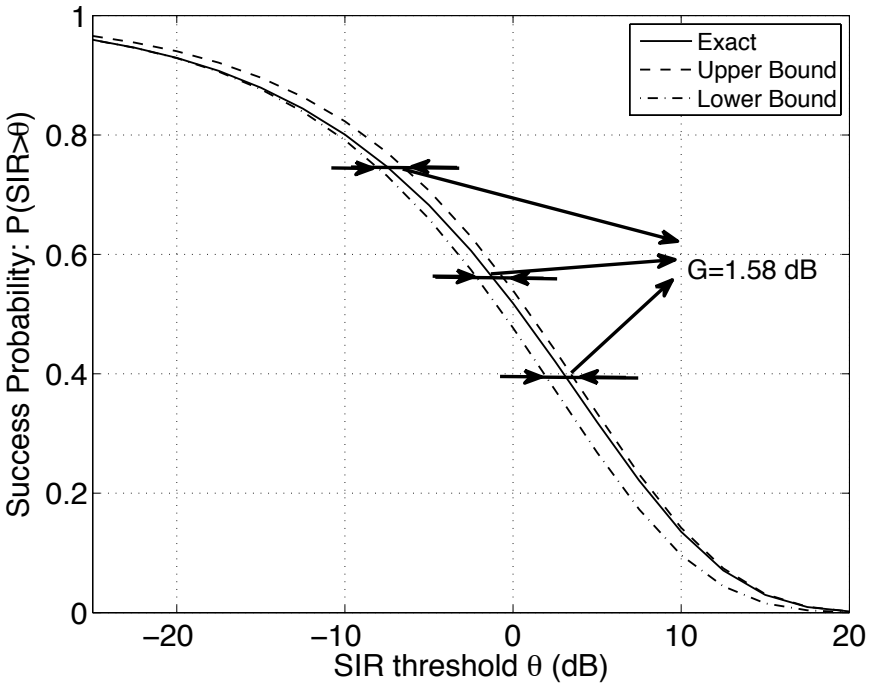

Figure 4.2. Comparison of unconditional success probability between the theoretical result from (4.14) and its bounds as a function of the SIR threshold θ in dB: $\alpha = 4$, $\lambda = 0.1$, $R = 1$, $p_0 = 0$, $p_1 = p_2 = 0.5$, $\beta = 0$. The horizontal gap from (4.25) is $G = 36/25$ or 1.58 dB for these parameters.

success probability from (4.14) and its closed-form upper and lower bounds under perfect self-interference cancellation as a function of the SIR threshold in dB. To obtain the exact curve, the double integral $F(\theta R^\alpha, \alpha, R)$ is numerically evaluated. As seen, both bounds are tight with constant horizontal gap $G = 1.58$ dB everywhere for $p_1 = p_2 = 0.5$ and $\delta = 2/\alpha = 1/2$.

Furthermore, we can examine the relationship between the two key functions $F(\theta R^\alpha, \alpha, R)$ and $H(\theta R^\alpha, \alpha)$. The following corollary bounds their ratio:

Corollary 12. *The ratio F/H is bounded as follows:*

$$1+\delta \leq \frac{F(\theta R^{\alpha},\alpha,R)}{H(\theta R^{\alpha},\alpha)} \leq 2, \quad \forall\, \theta>0, R>0, \alpha>2. \tag{4.27}$$

Moreover, the ratio is independent of the link distance R and

$$\lim_{\theta\to\infty} \frac{F(\theta R^{\alpha},\alpha,R)}{H(\theta R^{\alpha},\alpha)} = 1+\delta. \tag{4.28}$$

Proof. From the proof of the upper and lower bounds of the conditional success probability p_s^{HD}, i.e., (4.21) and (4.23), we have

$$\exp(-2\lambda p_2 H(s,\alpha)) \leq L_{I_2}(s) \leq \exp(-\lambda p_2(1+\delta)H(s,\alpha)), \tag{4.29}$$

where $L_{I_2}(s) = \exp(-\lambda p_2 F(s,\alpha,R))$ from (4.10). By taking the logarithm on both sides of the above, we have

$$-2\lambda p_2 H(s,\alpha) \leq -\lambda p_2 F(s,\alpha,R) \leq -\lambda p_2(1+\delta)H(s,\alpha), \tag{4.30}$$

which leads to (4.27).

For the independence on the link distance R, since $H(\theta R^{\alpha},\alpha) = \frac{\pi^2\delta\theta^{\delta}R^2}{\sin(\pi\delta)}$, we need to prove that $F(\theta R^{\alpha},\alpha,R)$ is also proportional to R^2. By the change of the variable $r_1 = r/R$, we can express (4.4) as

$$F(\theta R^{\alpha},\alpha,R) = R^2 \int_0^{\infty} \left(2\pi - \frac{1}{1+\theta r_1^{-\alpha}} \int_0^{2\pi} \frac{d\varphi}{1+\theta\left(r_1^2+1+2r_1\cos\varphi\right)^{-\alpha/2}}\right) r_1 dr_1, \tag{4.31}$$

which completes the proof of independence of link distance R. For the limit, by

the change of the variable $r_2 = r_1\theta^{-\frac{1}{\alpha}}$, we have

$$F(\theta R^\alpha, \alpha, R) = \theta^\delta R^2 \int_0^\infty \left(2\pi - \frac{1}{1+r_2^{-\alpha}} \int_0^{2\pi} \frac{d\varphi}{1+\left(r_2^2+\theta^{-\delta}+2r_2\theta^{-\delta/2}\cos\varphi\right)^{-\alpha/2}}\right) r_2 dr_2. \tag{4.32}$$

Therefore,

$$\lim_{\theta\to\infty} \frac{F(\theta R^\alpha, \alpha, R)}{H(\theta R^\alpha, \alpha)} = \lim_{\theta\to\infty} \frac{\int_0^\infty \left(2\pi - \frac{1}{1+r_2^{-\alpha}} \int_0^{2\pi} \frac{d\varphi}{1+\left(r_2^2+\theta^{-\frac{2}{\alpha}}+2r_2\theta^{-\frac{1}{\alpha}}\cos\varphi\right)^{-\alpha/2}}\right) r_2 dr_2}{\frac{\pi^2\delta}{\sin(\pi\delta)}} \tag{4.33}$$

$$= \frac{\int_0^\infty \left(2\pi - \frac{2\pi}{\left(1+r_2^{-\alpha}\right)^2}\right) r_2 dr_2}{\frac{\pi^2\delta}{\sin(\pi\delta)}} \tag{4.34}$$

$$= 1+\delta. \tag{4.35}$$

□

This corollary is useful in calculating the SIR loss, the maximal throughput, and their bounds in the following. Also, we can conclude that the upper bound of the success probability is asymptotically exact as $\theta \to \infty$. It is also illustrated by Fig. 4.2.

4.3.2 SIR Loss Due to FD Operation

In this subsection, we investigate the SIR loss caused by the FD operation in wireless networks described by $\hat{\Phi}$. Consider two extreme cases: one is the case where all concurrently transmitting nodes work in HD mode, i.e., $p_1 = 1$, and the

other is where all concurrently transmitting nodes work in FD mode, i.e., $p_2 = 1$. The success probabilities of HD-only and FD-only networks follows from (4.3) as

$$p_{s,\, p_1=1} = \exp(-\lambda H(\theta R^\alpha, \alpha)) \tag{4.36}$$

and

$$p_{s,\, p_2=1} = \kappa \exp(-\lambda F(\theta R^\alpha, \alpha, R)). \tag{4.37}$$

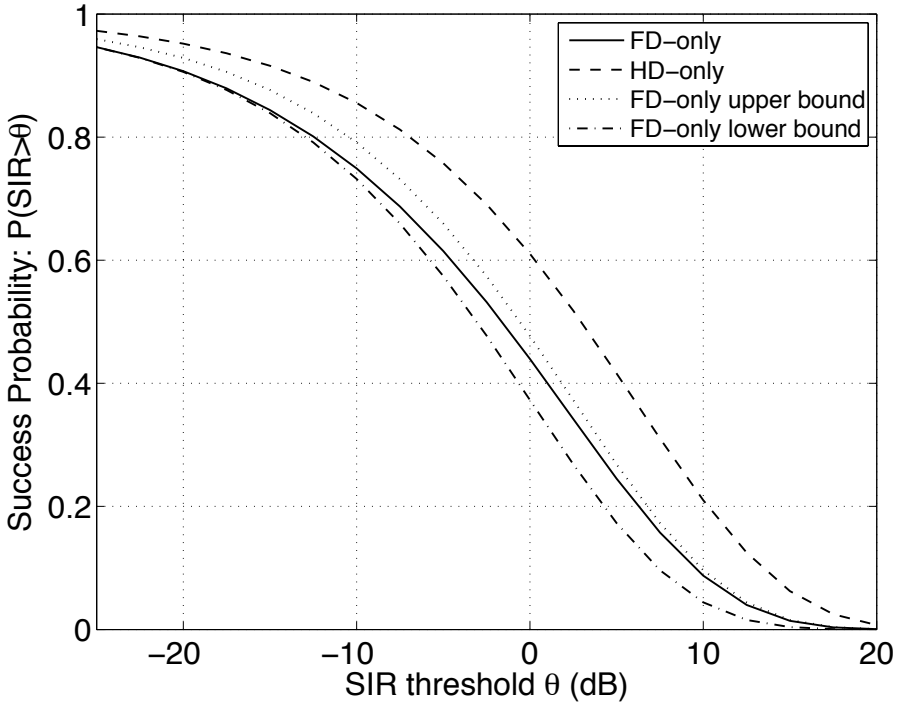

Figure 4.3. Comparison of success probabilities of FD-only networks, its bounds, and HD-only networks as a function of the SIR threshold θ in dB under perfect self-interference cancellation: $\alpha = 4$, $\lambda = 0.1$, $R = 1$, $p_0 = 0$, $\beta = 0$.

Figure 4.3 plots the success probability of FD-only networks and its upper and lower bounds as well as success probability of HD-only networks as a function of the SIR threshold in dB. Clearly, FD transmission in a FD-only wireless network leads to a SIR loss compared to its counterpart HD-only wireless network in the success probability, which is the ccdf of SIR. The SIR loss can be defined as the horizontal gap between two SIR distributions as follows from (4.24):

Definition 1. *The SIR loss between FD-only and HD-only networks is defined as*

$$G(p) \triangleq \frac{\theta_{\mathrm{HD}}(p)}{\theta_{\mathrm{FD}}(p)} = \frac{p^{-1}_{s,\,p_1=1}(p)}{p^{-1}_{s,\,p_2=1}(p)}, \tag{4.38}$$

where p is the target success probability and p_s^{-1} is the inverse of the ccdf of the SIR. $\theta_{\mathrm{HD}}(p)$ is the SIR threshold when the target success probability is p, i.e., $\theta_{\mathrm{HD}}(p) = p^{-1}_{s,\,p_1=1}(p)$. Similarly, $\theta_{\mathrm{FD}}(p) = p^{-1}_{s,\,p_2=1}(p)$.

The following theorem bounds this SIR loss.

Theorem 13. *The SIR loss $G(p)$ between the FD-only network and HD-only network is bounded as*

$$(1+\delta+\gamma(\theta_{\mathrm{FD}}(p)))^{1/\delta} \leq G(p) \leq (2+\gamma(\theta_{\mathrm{FD}}(p)))^{1/\delta}, \tag{4.39}$$

where $\gamma(x) = x^{1-\delta}\frac{R^{\alpha-2}\beta\sin(\pi\delta)}{\lambda\pi^2\delta K}$.

Proof. The proof is quite straightforward by equating

$$p_{s,\,p_1=1}(\theta_{\mathrm{HD}}) = p_{s,\,p_2=1}(\theta_{\mathrm{FD}}),$$

and solving for the ratio $\frac{\theta_{\mathrm{HD}}}{\theta_{\mathrm{FD}}}$. From (4.36) and (4.37), we obtain

$$\lambda H(\theta_{\mathrm{HD}} R^{\alpha}, \alpha) = \lambda F(\theta_{\mathrm{FD}} R^{\alpha}, \alpha) + \theta_{\mathrm{FD}} R^{\alpha} \beta / K,$$

and from (4.27) in Corollary 12, we have

$$(1+\delta)\lambda H(\theta_{\mathrm{FD}} R^{\alpha}, \alpha) \leq \lambda H(\theta_{\mathrm{HD}} R^{\alpha}, \alpha) - \theta_{\mathrm{FD}} R^{\alpha} \beta / K \leq 2\lambda H(\theta_{\mathrm{FD}} R^{\alpha}, \alpha). \quad (4.40)$$

By inserting $H(s, \alpha) = \frac{\pi^2 \delta s^{\delta}}{\sin(\pi\delta)}$ into (4.40) and after elementary manipulations, (4.40) leads to

$$(1 + \delta + \gamma(\theta_{\mathrm{FD}}))^{1/\delta} \leq \frac{\theta_{\mathrm{HD}}}{\theta_{\mathrm{FD}}} \leq (2 + \gamma(\theta_{\mathrm{FD}}))^{1/\delta}. \quad (4.41)$$

Hence, we have (4.39). □

Apparently, the bounds of the SIR loss depend on the SIR threshold θ_{FD} due to the imperfect self-interference cancellation since $\gamma(\theta_{\mathrm{FD}}) > 0$ for imperfect self-interference cancellation. It means that imperfect self-interference cancellation introduces an extra SIR loss compared to perfect self-interference cancellation and that the SIR loss gets larger as the residual self-interference increases, as shown in Figure 4.4.

Corollary 14. *The SIR loss $G(p)$ between the FD-only network and HD-only network under perfect self-interference cancellation ($\beta = 0$) is bounded as*

$$(1+\delta)^{1/\delta} \leq G(p) \leq 2^{1/\delta}. \quad (4.42)$$

Proof. Follows from Theorem 13 since $\gamma(\theta_{\mathrm{FD}}) = 0$ for $\beta = 0$. □

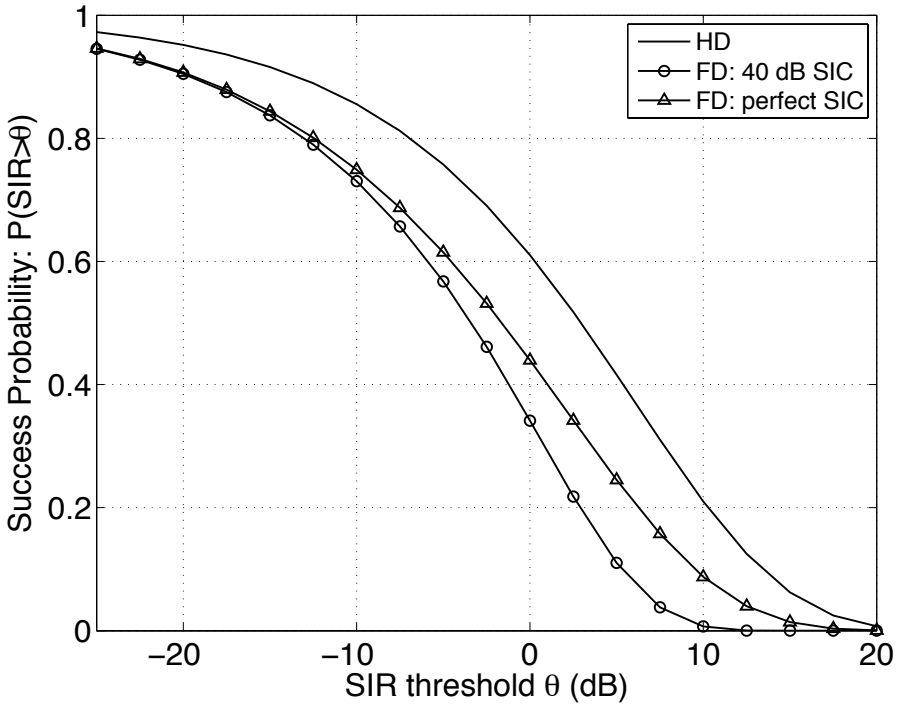

Figure 4.4. Success probabilities of FD-only networks ($p_{s,\,p_2=1}(\theta)$) and HD-only networks ($p_{s,\,p_1=1}(\theta)$) at two SIPRs $\beta = 10^{-4}$ and $\beta = 0$. The other parameters are $\alpha = 4$, $\lambda = 0.1$, $R = 1$, $K = -34$ dB (Assume that $G_{\text{tx}} = G_{\text{rx}} = 2$, i.e., 3 dBi, and $f_c = 2.4$ GHz).

For perfect self-interference cancellation ($\beta = 0$), the bounds of the SIR loss only depend on the path loss exponent $\alpha = 2/\delta$, i.e., they are independent of the SIR threshold, the target success probability p, and the link distance R. Corollary 14 can also be proven in the following way. Under perfect self-interference cancellation, from (4.36), we have

$$p_{s,\,p_1=1}(\theta_{\text{HD}}) = e^{-c\theta_{\text{HD}}^{\delta}},$$

where $c = \frac{\lambda \pi^2 \delta R^2}{\sin(\pi\delta)}$. From (4.37) and (4.27), we have

$$\underline{p}_{s,\, p_2=1}(\theta_{\mathrm{FD}}) = e^{-2c\theta_{\mathrm{FD}}^{\delta}},$$
$$\overline{p}_{s,\, p_2=1}(\theta_{\mathrm{FD}}) = e^{-(1+\delta)c\theta_{\mathrm{FD}}^{\delta}}.$$

By solving

$$\underline{p}_{s,\, p_2=1}(\theta_{\mathrm{FD}}) = p_{s,\, p_1=1}(\theta_{\mathrm{FD}}\overline{G}),$$
$$\overline{p}_{s,\, p_2=1}(\theta_{\mathrm{FD}}) = p_{s,\, p_1=1}(\theta_{\mathrm{FD}}\underline{G}),$$

we obtain the upper bound $\overline{G} = 2^{\frac{1}{\delta}}$ and the lower bound $\underline{G} = (1+\delta)^{\frac{1}{\delta}}$.

Therefore, the upper (lower) bound of the SIR loss are actually the constant horizontal gap between the upper (lower) bound of the success probability of the FD-only network and that of the HD-only network. Under perfect self-interference cancellation, the upper bound of the success probability of the FD-only network is just the success probability curve of the HD-only network left shifted by $\underline{G}^{\mathrm{dB}} = \frac{10\log_{10}(1+\delta)}{\delta}$ dB, whereas the lower bound is that left shifted by $\overline{G}^{\mathrm{dB}} = \frac{10\log_{10}2}{\delta}$ dB. For $\alpha = 4$, the upper bound in Figure 4.3 is equivalent to the HD curve left-shifted by 3.5 dB while the lower bound equivalent to that left-shifted by 6.0 dB.

To summarize, FD-only operation can result in up to 6.0 dB SIR loss compared to HD-only operation even under perfect self-interference cancellation. Remarkably, this result only depends on the path loss exponent. The above analysis accurately quantifies the SIR loss caused by the extra interference introduced by the FD transmissions. Imperfect self-interference cancellation further adds to the SIR loss, especially when the SIR threshold is high, as shown in Fig. 4.4.

4.4 Throughput Analysis

4.4.1 Problem Statement

The purpose of FD transmission in a network is to increase the network throughput. While FD increases the throughput of an isolated link, it also causes additional interference to the other links. As analyzed in the previous section, FD transmission leads to SIR loss. There is a tradeoff between the link throughput and interference when the nodes in the networks decide to choose FD or HD. Given a network that consists of nodes of FD capability and HD capability, how should a node choose between FD and HD operation in order to maximize the network-wide throughput as the network configuration varies? It is important to determine under what condition one should choose FD.

First, we need to define the throughput. In a random wireless network described by $\hat{\Phi}$, we can consider the throughput of the *typical link* as mentioned in the network model. It has probability p_1 to be in HD mode and p_2 to be in FD mode. Therefore, its throughput can be defined as follows:

Definition 15. For a wireless network described by $\hat{\Phi}$, the throughput is defined as

$$T \triangleq \lambda \left(p_1 p_s^{\mathrm{HD}} \log(1+\theta) + 2 p_2 p_s^{\mathrm{FD}} \log(1+\theta) \right), \tag{4.43}$$

assuming that a spectral efficiency of $\log(1+\theta)$ is achievable for a SIR threshold θ.

Let $\lambda_1 \triangleq \lambda p_1$ and $\lambda_2 \triangleq \lambda p_2$ be the densities of HD links and FD links. λ_1 and λ_2 can be tuned by changing the transmit probabilities of HD and FD modes p_1 and p_2 given a fixed node density λ or vice versa. By doing so, we can optimize the throughput over the densities of HD and FD links (λ_1 and λ_2) instead of just the

transmit probabilities p_1 and p_2 and reduce the variables by one as well. Hence, (4.43) can be rewritten as

$$T = \lambda_1 p_s^{\mathrm{HD}} \log(1+\theta) + 2\lambda_2 p_s^{\mathrm{FD}} \log(1+\theta). \tag{4.44}$$

Given the definition of throughput, there are two extreme cases that are particularly relevant: HD-only networks and FD-only networks, as mentioned earlier. Their throughputs are given as

$$T^{\mathrm{HD}} = \lambda_1 \log(1+\theta) \exp(-\lambda_1 H(\theta_{\mathrm{HD}} R^{\alpha}, \alpha)) \tag{4.45}$$

and

$$T^{\mathrm{FD}} = 2\lambda_2 \kappa \log(1+\theta) \exp(-\lambda_2 F(\theta R^{\alpha}, \alpha)). \tag{4.46}$$

With the above setup, the goal is to optimize the throughput over the densities λ_1 and λ_2:

$$T_{\max} = \max_{\lambda_1, \lambda_2} T(\lambda_1, \lambda_2). \tag{4.47}$$

It is also interesting to find the relationship between the maxima of T^{HD}, T^{FD} and T, denoted as $T_{\max}^{\mathrm{HD}}$, $T_{\max}^{\mathrm{FD}}$ and $T_{\max}$.

4.4.2 Throughput Optimization

Inserting p_s^{HD} and p_s^{FD} from (4.3) and (4.5) into (4.43), we have

$$T(\lambda_1, \lambda_2) = (\lambda_1 + 2\lambda_2 \kappa) \exp(-\lambda_1 H) \exp(-\lambda_2 F) \log(1+\theta). \tag{4.48}$$

From now on, we will use H to denote $H(\theta R^{\alpha}, \alpha)$ and F to denote $F(\theta R^{\alpha}, \alpha, R)$

for simplicity. $T_{\max}^{\mathrm{HD}}$ and $T_{\max}^{\mathrm{FD}}$ can be easily obtained by the following lemma.

Lemma 16. *For a HD-only network, described by $\hat{\Phi}$ with $p_1 = 1$, $T_{\max}^{\mathrm{HD}}$ is given by*

$$T_{\max}^{\mathrm{HD}} = T^{\mathrm{HD}}\left(\frac{1}{H}\right) = \frac{1}{eH}\log(1+\theta), \tag{4.49}$$

with optimal density of HD links

$$\lambda_1^{\mathrm{opt}} = \frac{1}{H}. \tag{4.50}$$

For a FD-only network, described by $\hat{\Phi}$ with $p_2 = 1$, $T_{\max}^{\mathrm{FD}}$ is given by

$$T_{\max}^{\mathrm{FD}} = T^{\mathrm{FD}}\left(\frac{1}{F}\right) = \frac{2}{e\kappa F}\log(1+\theta), \tag{4.51}$$

with optimal density of FD links

$$\lambda_2^{\mathrm{opt}} = \frac{1}{F}. \tag{4.52}$$

Proof. The proof is straightforward by taking the derivatives of T^{HD} and T^{FD} with respect to λ_1 and λ_2, respectively. □

A similar result for HD-only networks has been presented in [32, Proposition 4]. In fact, $1/H$ and $1/F$ are the spatial efficiency [32] of HD-only networks and FD-only networks, respectively. The spatial efficiency quantifies how efficiently a wireless network uses space as a resource. A large spatial efficiency indicates high spatial reuse.

In the following theorem, we show that $T_{\max}$ is achieved by setting all concurrently transmitting nodes to be in FD mode or in HD mode or in a mixed FD/HD mode, depending on one simple condition.

Theorem 17. *Let*

$$L \triangleq \{(\lambda_1, \lambda_2) \in (\mathbb{R}^+)^2 \colon \lambda_1 + 2\kappa\lambda_2 = H^{-1}\}. \tag{4.53}$$

For a wireless network described by $\hat{\Phi}$, the maximal throughput is given by

$$T_{\max} = \begin{cases} T_{\max}^{\mathrm{FD}} & \text{if } F < 2\kappa H \\ T_{\max}^{\mathrm{HD}} & \text{if } F > 2\kappa H \\ T_{\max}^{\mathrm{HD}} = T_{\max}^{\mathrm{FD}} & \text{if } F = 2\kappa H \end{cases} \tag{4.54}$$

with the optimal densities of HD and FD links

$$\left(\lambda_1^{\mathrm{opt}}, \lambda_2^{\mathrm{opt}}\right) \begin{cases} = \left(0, \frac{1}{F}\right) & \text{if } F < 2\kappa H \\ = \left(\frac{1}{H}, 0\right) & \text{if } F > 2\kappa H \\ \in L & \text{if } F = 2\kappa H. \end{cases} \tag{4.55}$$

Proof. Taking the derivative of T w.r.t. λ_1 and λ_2 leads to

$$\frac{\partial T}{\partial \lambda_1} = \exp(-\lambda_1 H - \lambda_2 F) \log(1+\theta)[1 - H(2\kappa\lambda_2 + \lambda_1)], \tag{4.56}$$

$$\frac{\partial T}{\partial \lambda_2} = \exp(-\lambda_1 H - \lambda_2 F) \log(1+\theta)[2\kappa - F(2\kappa\lambda_2 + \lambda_1)]. \tag{4.57}$$

Setting $\frac{\partial T}{\partial \lambda_1} = 0$ and $\frac{\partial T}{\partial \lambda_2} = 0$, we have

$$\lambda_1 + 2\kappa\lambda_2 = \frac{1}{H} \tag{4.58}$$

$$\lambda_1 + 2\kappa\lambda_2 = \frac{2\kappa}{F}. \tag{4.59}$$

1. $F = 2\kappa H$: Both partial derivatives are zero as long as $(\lambda_1, \lambda_2) \in L$. $(1/H, 0)$ and $(0, 2\kappa/F)$ both lie in L. Hence, $T_{\max} = T(1/H, 0) = T^{\mathrm{HD}}_{\max}$ and also $T_{\max} = T(0, 2\kappa/F) = T^{\mathrm{FD}}_{\max}$. This case is the break-even point where FD and HD have the same throughput. That means in a wireless network, the typical link has the same throughput no matter if it is in FD or HD mode.

2. $F > 2\kappa H$: Under this condition, let $\frac{\partial T}{\partial \lambda_1} = 0$ and we have (4.58). Moreover, $\frac{\partial T}{\partial \lambda_2} < 0$. Therefore, the maximal T is achieved at $(\lambda_1, \lambda_2) = (1/H, 0)$ from (4.58) and $\frac{\partial T}{\partial \lambda_2} < 0$. Note that $T(1/H, 0) = T^{\mathrm{HD}}(1/H) = T^{\mathrm{HD}}_{\max}$. On the other hand, letting $\frac{\partial T}{\partial \lambda_2} = 0$, we have (4.59) and $\frac{\partial T}{\partial \lambda_1} > 0$, which leads to that the maximal T is achieved at $(\lambda_1, \lambda_2) = (2\kappa/F, 0)$. Since $T(2\kappa/F, 0) < T(1/H, 0)$. We conclude that $T_{\max} = T^{\mathrm{HD}}$ in this case.

3. $F < 2\kappa H$: By similar reasoning as in the second case, we can conclude that $T_{\max} = T^{\mathrm{FD}}$ in this case.

□

Under perfect self-interference cancellation ($\beta = 0$), $F < 2\kappa G$, and we always have

$$T_{\max} = T^{\mathrm{FD}}_{\max},$$

which means $T_{\max}$ is always achieved by setting all transmitting nodes to work in FD mode, despite the extra interference caused by the FD nodes. This conclusion holds for all network configurations $(\lambda, \theta, R, \alpha)$.

On the other hand, the following corollary quantifies how the imperfect self-interference cancellation affects the throughput in a wireless network with full-duplex radios.

Corollary 18. *Given an SIR threshold θ, path loss exponent α, and link distance R, there exists a critical SIPR value β_c in the wireless network described by $\hat{\Phi}$: when $\beta < \beta_c$, FD is preferable in terms of throughput while HD has better throughput when $\beta > \beta_c$, where*

$$\beta_c = \frac{K \log(2H/F)}{\theta R^\alpha}. \tag{4.60}$$

Proof. β_c can be obtained by solving $F = 2\kappa H = 2e^{-\theta R^\alpha \beta/K} H$. By Corollary 12, the ratio of F/H does not depend on R and hence β_c scales as $R^{-\alpha}$. □

Figure 4.5 plots the relationship between the link distance and the self-interference cancellation threshold β_c. It provides very valuable insight into the system design. The curves are linear in this log-log plot with slope $-1/\alpha$. The region under the lines is the region where FD transmission achieves a higher network throughput. For example, assume that the self-interference cancellation is limited to 80 dB due to hardware imperfection. In this case, FD transmission is preferable only if the link distance is smaller than 10 when $\theta = 0$ dB and $\alpha = 4$ under the wireless network model used in this chapter. To achieve a link distance of up to 100, the self-interference cancellation needs to be at least 100 dB ($\alpha = 3$) and 120 dB ($\alpha = 4$) when $\theta = 0$ dB. When the link distance is greater than 100 with self-interference cancellation no greater than 120 dB, it is better to use HD. So the amount of self-interference cancellation determines the maximal transmission range for which FD has better throughput than HD.

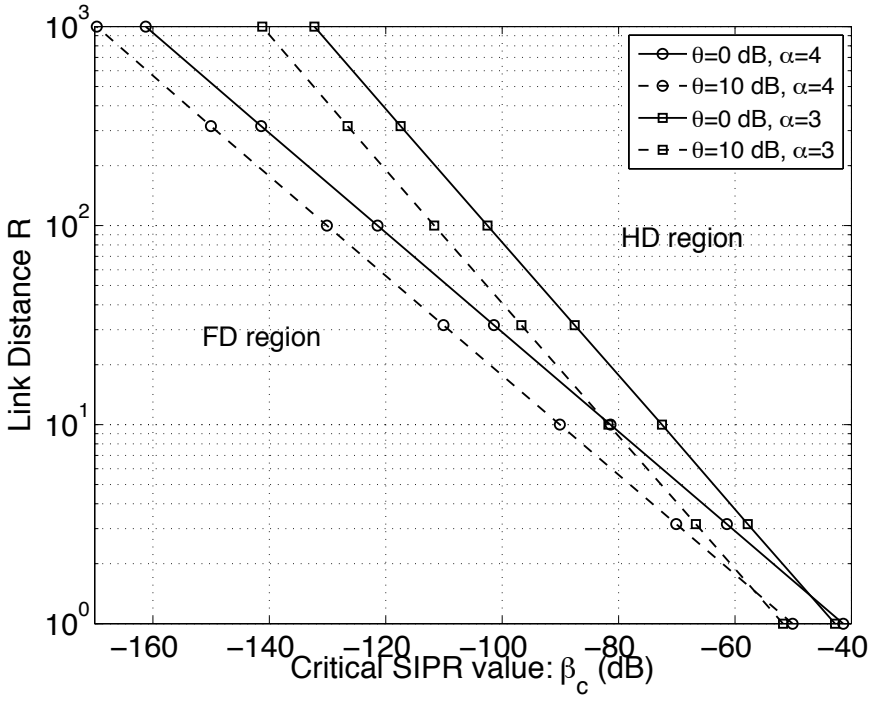

Figure 4.5. The link distance vs the critical SIPR β_c from (4.60) with $K = -34$ dB for $G_{\text{tx}} = G_{\text{rx}} = 2$, i.e., 3 dBi, and $f_c = 2.4$ GHz, which corresponds to the carrier frequency of a WiFi signal. Below the curves, FD provides a higher throughput, while above the curves, HD does.

4.4.3 Comparison of FD with HD

Since the mixed FD/HD network achieves the maximal throughput in the extreme case of a FD-only or HD-only network, we can simply focus on FD-only and HD-only networks and compare their maximal throughputs from the results in Lemma 16. The throughput gain of a FD network over a HD network is of great interest. It is defined as follows.

Definition 19. The throughput gain (TG) is defined as the ratio between the maximal throughput of FD-only networks and HD-only networks given the same

network parameters (θ, R, α):

$$\mathrm{TG} \triangleq \frac{T_{\max}^{\mathrm{FD}}}{T_{\max}^{\mathrm{HD}}}.$$

The following corollary quantifies and bounds TG in terms of F and H. Note that F and H are constant given (θ, R, α).

Corollary 20. *The throughput gain is given by*

$$\mathrm{TG} = \frac{2\kappa H}{F} \tag{4.61}$$

and bounded as

$$\kappa < \mathrm{TG} < \frac{2\kappa}{1+\delta}. \tag{4.62}$$

Moreover, for any $\beta \geq 0$,

$$\mathrm{TG}(\theta) \sim \frac{2\kappa}{1+\delta} = \frac{2}{1+\delta} \exp(-\theta R^{\alpha} \beta / K), \quad \theta \to \infty. \tag{4.63}$$

Proof. From (4.49) and (4.51), we have (4.61). The upper and lower bounds are easily obtained from Corollary 12.

For $\beta > 0$,

$$\lim_{\theta \to \infty} \kappa = \lim_{\theta \to \infty} e^{-\frac{\theta R^{\alpha} \beta}{K}} = 0. \tag{4.64}$$

Therefore, both the lower bound and upper bound of TG converge to 0 as θ goes to ∞. As a result,

$$\lim_{\theta \to \infty} \mathrm{TG}(\theta) = 0. \tag{4.65}$$

$\beta = 0$ implies $\kappa = 1$, which leads to

$$\lim_{\theta \to \infty} \mathrm{TG}(\theta) = \lim_{\theta \to \infty} \frac{2H}{F} = \frac{2}{1+\delta} \tag{4.66}$$

from (4.28). Combining (4.65) and (4.66), we obtain (4.63). □

(4.63) indicates that the throughput gain converges to its upper bound as θ goes to infinity. Fig. 4.6 illustrates the throughput gain as a function of the SIR threshold together with its upper and lower bounds given in (4.62). As seen, the throughput gain is always lower than $\frac{2}{1+\delta}$ since the upper bound is smaller than that. For perfect self-interference cancellation, the throughput gain increases as the SIR threshold gets larger as shown in Fig. 4.6(c). The throughput gain decreases in the high SIR regime due to the imperfect self-interference cancellation as shown in Fig. 4.6(a) and Fig. 4.6(b). When the self-interference cancellation is not sufficient, the throughput gain is less than 1, which means that the HD-only network has a higher throughput, i.e., the value in the curve after $\theta >$ 10 dB in Fig. 4.6(a) is less than 1. These figures illustrate the throughput gain under different conditions, especially the impact of the imperfect self-interference cancellation on the throughput.

4.5 Conclusion

In this chapter, we analyzed the throughput of wireless networks with FD radios using tools from stochastic geometry. Given a wireless network of radios with both FD and HD capabilities, we showed that FD transmission is always preferable compared to HD transmission in terms of throughput when the self-interference cancellation is perfect. It turns out that the throughput of HD transmission cannot be doubled and the actual gain is $\frac{2\alpha}{\alpha+2}$ for an ALOHA protocol, where α is the path loss exponent. Under imperfect self-interference cancellation, the network has a break-even point where FD and HD have the same throughput. The break-even point depends on the amount of self-interference cancellation and the

link distance. Given a fixed SIR threshold and path loss exponent, the necessary amount of self-interference cancellation in dB is logarithmically proportional to the link distance. It means that the residual self-interference determines the maximal link distance within which FD is beneficial compared to HD. It provides great insights into the network design with FD radios. We also analyzed and quantified the effects of imperfect self-interference cancellation on the network throughput and SIR loss. The SIR loss of a FD-only network over a HD-only network is quantified within tight bounds. The horizontal gap is utilized to determine the SIR loss. Moreover, the throughput gain of FD over HD is presented under imperfect self-interference cancellation.

In our network model, we consider the interference-limited case where the thermal noise is ignored. However, this is not a restriction as the throughput gain is independent of the thermal noise since the thermal noise adds the same exponential factor ($\exp(-\theta R^{\alpha} W)$ [33, Page 105], where W is the thermal noise power) to the throughput expressions of both HD and FD networks and they cancel each other in the throughput gain.

In general, FD is a very powerful technique that can be adapted for the next-generation wireless networks. The throughput gain may be larger if more advanced MAC protocols other than ALOHA are used or the interference management can be used for the pairwise interferers in the FD links. A FD-friendly MAC scheme should let the node decide to use FD or HD based on its surrounding interference in order to maximize the overall network throughput. There is a strong need for a MAC protocol tailored for a wireless network of radios with both FD and HD capacities and an intelligent and adaptive scheme to switch between FD and HD based on different network configurations.

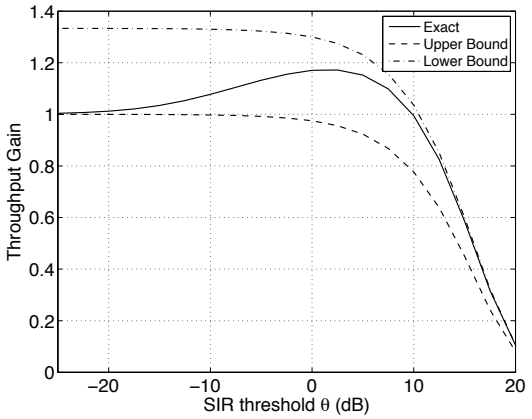

(a) 50 dB self-interference cancellation: $\beta = 10^{-5}$

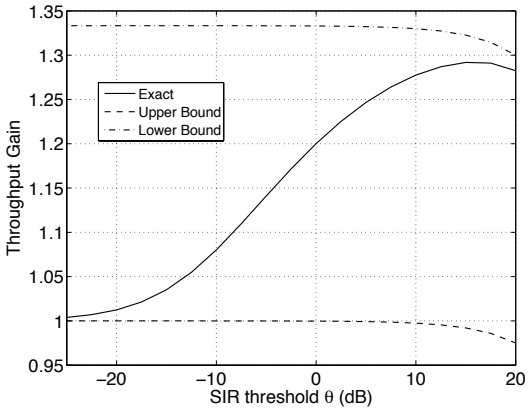

(b) 70 dB self-interference cancellation: $\beta = 10^{-7}$

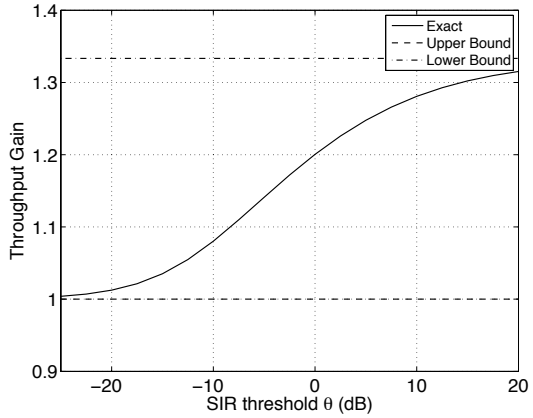

(c) Perfect self-interference cancellation: $\beta = 0$

Figure 4.6. Throughput gain as a function of the SIR threshold θ and its bounds at different SIPRs for $\alpha = 4$, $R = 1$.

CHAPTER 5

CONCLUSION AND FUTURE WORK

5.1 Power Control and Full Duplex

Power control has been a technique that is exclusively used in wireless networks to improve the network performance. Future work can be focused on design distributed power control algorithm for the FD wireless networks. Novel dynamic power control algorithms have been proposed in a point-to-point FD transmission [13] where the FD sum-rate has been maximized via analysis and/or simulation. [58] studied three-node full-duplex relay link and proposed a hybrid FD/HD relaying scheme with adaptive power control. There are also other references in the literature that are focused on FD relaying with power control such as [57, 81]. While most are focused FD relaying or single-link FD transmission, it is interesting to study FD wireless networks with power control.

Given a random wireless network with FD radios, we can propose a new power control algorithm. Compared to the results in Chapter 2, the convergence condition of the power control algorithm needs to be modified since each node serves both transmitter and receiver in the network. A novel MAC scheme tailored for FD wireless networks may be available based on the new convergence conditions.

5.2 RODD

Chapter 3 provides the first proof of concept of RODD. We will test different on-off signaling and coding schemes and compare the link throughput for unidirectional and bidirectional traffic with and without synchronization. We will also test ARQ-type schemes where a receiver can immediately stop the sender once it has acquired enough information for decoding. The extension from two nodes to three or more nodes will be the next big step in our prototype in which an *RODD network* will be created and evaluated.

5.3 Novel MAC schemes for Full-Duplex Wireless Networks

FD has attracted a lot of attention and been considered as a strong candidate technology for the next-generation wireless networks. Given a wireless network with FD radios, a FD-specific MAC scheme needs to be designed. Such a FD scheme should let the node decide to use FD or HD based on its surrounding interference in order to maximize the overall network throughput. Moreover, we need to come up with an intelligent and adaptive scheme to switch between FD and HD based on different network configurations.

APPENDIX A

A.1 Proof of Proposition 1

Proof. For $n = 2$,

$$\mathcal{P}_{\text{con}}(\infty) = \mathbb{E}_{\mathbf{r}_1,\mathbf{r}_2}\left[\int\int 1_{\left\{\|\mathbf{t}_1-\mathbf{r}_2\|\cdot\|\mathbf{t}_2-\mathbf{r}_1\|>R^2\rho^{2/\gamma}\right\}} f(\mathbf{t}_1 \mid \mathbf{r}_1) f(\mathbf{t}_2 \mid \mathbf{r}_2) d\mathbf{t}_1 d\mathbf{t}_2\right] \quad \text{(A.1)}$$

$$= \mathbb{E}_{\mathbf{r}_1,\mathbf{r}_2}\left[\left(\frac{1}{2\pi}\right)^2 \int_0^{2\pi}\int_0^{2\pi} 1_{\left\{\|Re^{j\theta_1}+\mathbf{r}_1-\mathbf{r}_2\|\cdot\|Re^{j\theta_2}+\mathbf{r}_2-\mathbf{r}_1\|>R^2\rho^{2/\gamma}\right\}} d\theta_1 d\theta_2\right] \quad \text{(A.2)}$$

$$= \mathbb{E}_{\mathbf{r}_1,\mathbf{r}_2}\left[\left(\frac{1}{2\pi}\right)^2 \int_0^{2\pi}\int_0^{2\pi} 1_{\left\{\|e^{j\theta_1}+\frac{\mathbf{r}_1-\mathbf{r}_2}{R}\|\cdot\|e^{j\theta_2}+\frac{\mathbf{r}_2-\mathbf{r}_1}{R}\|>\rho^{2/\gamma}\right\}} d\theta_1 d\theta_2\right] \quad \text{(A.3)}$$

$$\overset{\text{(a)}}{\geq} \mathbb{E}_{\mathbf{r}_1,\mathbf{r}_2}\left[\left(\frac{1}{2\pi}\right)^2 \int_0^{2\pi}\int_0^{2\pi} 1_{\left\{|\|\frac{\mathbf{r}_1-\mathbf{r}_2}{R}\|-1|\cdot|\|\frac{\mathbf{r}_2-\mathbf{r}_1}{R}\|-1|>\rho^{2/\gamma}\right\}} d\theta_1 d\theta_2\right] \quad \text{(A.4)}$$

$$= \mathbb{E}_{\mathbf{r}_1,\mathbf{r}_2}\left[1_{\left\{\left(\|\frac{\mathbf{r}_1-\mathbf{r}_2}{R}\|-1\right)^2>\rho^{2/\gamma}\right\}}\right], \quad \text{(A.5)}$$

where (a) results from the triangle inequality. Hence, a lower bound of $\mathcal{P}_{\text{con}}(\infty)$ (denoted as $\underline{\mathcal{P}}_{\text{con}}(\infty)$) is

$$\underline{\mathcal{P}}_{\text{con}}(\infty) = \mathbb{E}_{\mathbf{r}_1,\mathbf{r}_2}\left[1_{\left\{\left(\|\frac{\mathbf{r}_1-\mathbf{r}_2}{R}\|-1\right)^2>\rho^{2/\gamma}\right\}}\right]. \quad \text{(A.6)}$$

Letting $D = \|\mathbf{r}_1 - \mathbf{r}_2\|$,

$$\underline{\mathcal{P}}_{\text{con}}(\infty) = \mathbb{E}_D\left[1_{\left\{\left(\frac{D}{R}-1\right)^2>\rho^{2/\gamma}\right\}}\right]. \quad \text{(A.7)}$$

Note that $\mathbf{r}_1$ and $\mathbf{r}_2$ are two points that are independently and uniformly distributed over $B = [0, l]^2$. From Theorem 2.4.4 in [51], we can derive the PDF of their distance D as

$$f(d) = \begin{cases} \frac{2\pi d}{l^2} - \frac{8d^2}{l^3} + \frac{2d^3}{l^4}, & 0 \le d \le l \\ \frac{4d}{l^2}\left[\sin^{-1}\left(\frac{l}{d}\right) - \cos^{-1}\left(\frac{l}{d}\right) - \frac{d^2}{2l^2} - \frac{2\sqrt{d^2-l^2}}{l} - 1\right], & l \le d \le \sqrt{2}l \\ 0, & \text{otherwise.} \end{cases} \tag{A.8}$$

Given $\rho > 0$ dB and $R_0 = R\left(1 + \rho^{\frac{1}{\gamma}}\right) < l$,

$$\begin{aligned} \underline{\mathcal{P}}_{\text{con}}(\infty) &= \mathbb{E}_D\left[1_{\left\{\left(\frac{D}{R}-1\right)^2 > \rho^{2/\gamma}\right\}}\right] && \text{(A.9)} \\ &= \int_{R_0}^{\infty} f(x)dx && \text{(A.10)} \\ &= \int_{R_0}^{l}\left(\frac{2\pi x}{l^2} - \frac{8x^2}{l^3} + \frac{2x^3}{l^4}\right)dx && \text{(A.11)} \\ &\quad + \int_{l}^{\sqrt{2}l}\frac{4x}{l^2}\left[\sin^{-1}\left(\frac{l}{x}\right) - \cos^{-1}\left(\frac{l}{x}\right) - \frac{x^2}{2l^2} - \frac{2\sqrt{x^2-l^2}}{l} - 1\right]dx && \text{(A.12)} \\ &= \pi - 3 - \left(\frac{\pi R_0^2}{l^2} - \frac{8R_0^3}{3l^3} + \frac{R_0^4}{2l^4}\right) + I_0 - I_1, && \text{(A.13)} \end{aligned}$$

where $I_0 = \int_l^{\sqrt{2}l} \frac{4x}{l^2}\left[\sin^{-1}\left(\frac{l}{x}\right)\right]dx$, and $I_1 = \int_l^{\sqrt{2}l} \frac{4x}{l^2}\left[\cos^{-1}\left(\frac{l}{x}\right)\right]dx$. From [51], I_0 and I_1 can be calculated in terms of Gauss' hypergeometric function. By some basic calculations, we can obtain that $I_0 = 2$ and $I_1 = 2 - \pi$. Inserting I_0 and I_1 into (A.13), we obtain (2.42). □

A.2 E_b/N_0 Calculation

In order to be able to measure some values on the BER curve, we first have to know the SNR in the current setup. The relation between E_b/N_0 and SNR is given as follows:

$$\text{SNR} = \frac{E_b}{N_0} \cdot \frac{f_b}{B}, \tag{A.14}$$

where f_b is the channel data rate, and B is the channel bandwidth. Since binary modulation is used in our experiments, the datarate and the channel bandwidth are the same. Therefore, $E_b/N_0 = \text{SNR}$.

The basic idea to obtain the SNR is to estimate the power of the useful received signal (when only the other node is transmitting) and to estimate the power of a silent off-slot (when no one is transmitting) and divide the results. The different signal types are illustrated in Fig. A.1. The interesting slots are the silent off-slot and the one with the desired signal of another node. To avoid that the leakage of the transmitted signal affects the estimated values, 15% of the window size T is ignored at the beginning and the end of a slot for the calculation as illustrated in Fig. A.2. T corresponds to the length of one RODD slot in time. This value is reasonable, because as shown in Section 3.7.2, the side lobes are decreased by more than 30 dB after two symbols, which is 10% of a slot with size 20.

As the measurement setup is static, we assume that the E_b/N_0 stays nearly the same within one frame. The E_b/N_0 is calculated once for each frame. To increase the accuracy of E_b/N_0, all the non-erased slots with wanted received signal and all the silent off-slots during the preamble of one on-off frame are used to the E_b/N_0 calculation.

The procedure leads not exactly to the SNR ($\frac{S}{N}$), rather to $\frac{S+N}{N} = \frac{S}{N} + 1$. Therefore the value is reduced by 1 before conversion to dB. To achieve differ-

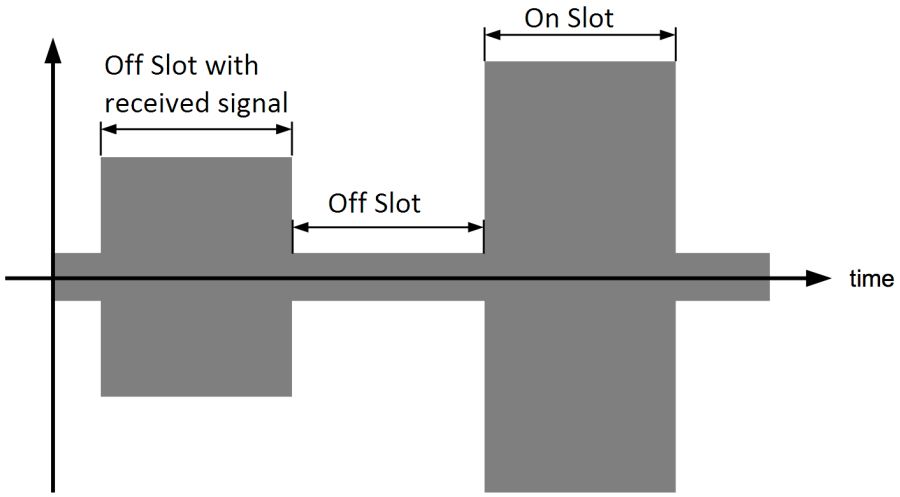

Figure A.1. Illustration of RODD signaling with off-slot that contains wanted signal and noise, respectively, as well as an on-slot with self-interference.

ent E_b/N_0 values, a combination of some factors is used. First of all the transmit/receive power gains can be set in software. For the transmitter the value can be set from 0 dB to 31 dB. The maximum output power using frequencies from 50 MHz to 1.2 GHz (we use 915 MHz for the measurements) is 17 dBm to 20 dBm (50 mW to 100 mW) [52]. The receiver's gain range is from 0 dB to 31.5 dB, and its maximum input power is 0 dBm (1 mW) [52]. The measurements in our experiments are made with all power gains set to 0 dB, which is the minimal gain for both transmitter and receiver in order to achieve the desired SNR range. Thus the output power at the transmitter is at most -10 dBm (0.1 mW). Moreover, attenuators are used to further decrease the SNR to the range of interest in the experiments.

Next, for the unidirectional benchmark an RF cable is used to connect the transmitter of one USRP with the receiver of the other USRP. To achieve different

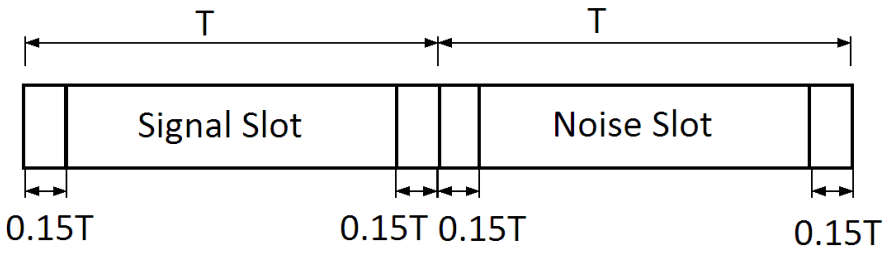

Figure A.2. Illustration of signal structure for the SNR calculation.

E_b/N_0 we attached different amounts of attenuators to the cable. The settings are summarized in Tables A.1 and A.2. The unidirectional mode is a more controlled measurement setup than the bidirectional mode. As an RF cable is used between the two USRPs, the SNR does not depend on the actual setup of the antennas or the position of the USRPs. Thus the measurements for different SNR values are not affected by changes in the placement of the USRPs. In contrast, the bidirectional mode is quite sensitive to such changes. The first column in Table A.2 is the hardware attenuation added to the transmitter side between the Tx antenna and the RF font end and the second column for the receiver side. The resulting SNRs at both nodes with standard deviation are summarized in the third and fourth columns.

attenuation (dB)	resulting E_b/N_0 (dB)
71	4.10 ± 0.52
70	5.17 ± 0.53
69	6.05 ± 0.53
68	7.11 ± 0.55
67	8.04 ± 0.55
66	9.12 ± 0.57
65	9.87 ± 0.57
64	10.98 ± 0.58
63	12.08 ± 0.59

TABLE A.1

Settings for different E_b/N_0 values for the BER measurement in unidirectional mode.

attenu. at Tx	attenu. at Rx	E_b/N_0 at Node 1	E_b/N_0 at Node 2
18	34	3.92 ± 0.61	3.68 ± 0.62
17	34	5.13 ± 0.61	4.40 ± 0.66
18	31	6.74 ± 0.65	6.09 ± 0.66
17	31	8.11 ± 0.65	7.90 ± 0.65
15	31	9.53 ± 0.66	9.08 ± 0.65
13	31	10.87 ± 0.66	10.72 ± 0.67
12	31	13.21 ± 0.66	12.63 ± 0.68

TABLE A.2

Settings for different E_b/N_0 values for the BER measurement in bidirectional mode.

attenu. at Tx	attenu. at Rx	E_b/N_0 at Node with Circulator
18	31	4.30 ± 0.57
16	31	7.49 ± 0.63
14	31	9.79 ± 0.65
12	31	10.90 ± 0.66
10	31	13.06 ± 0.70

TABLE A.3

Settings for different E_b/N_0 values for the BER measurement in bidirectional mode from Fig. 3.4(c).

BIBLIOGRAPHY

1. S. Agarwal, R. Katz, S. Krishnamurthy, and S. Dao. Distributed power control in ad-hoc wireless networks. In *2001 12th IEEE International Symposium on Personal, Indoor and Mobile Radio Communications*, volume 2, pages F–59–F–66 vol.2, Sep./Oct. 2001. doi: 10.1109/PIMRC.2001.965296.

2. V. Aggarwal, M. Duarte, A. Sabharwal, and N. Shankaranarayanan. Full- or half-duplex? A capacity analysis with bounded radio resources. In *2012 IEEE Information Theory Workshop (ITW)*, pages 207–211, Sept 2012. doi: 10.1109/ITW.2012.6404659.

3. E. Aryafar, M. A. Khojastepour, K. Sundaresan, S. Rangarajan, and M. Chiang. MIDU: Enabling MIMO full duplex. In *Proceedings of the 18th Annual International Conference on Mobile Computing and Networking (Mobicom'12)*, pages 257–268, New York, NY, USA, 2012. ISBN 978-1-4503-1159-5. doi: 10.1145/2348543.2348576. URL `http://doi.acm.org/10.1145/2348543.2348576`.

4. F. Baccelli and B. Blaszczyszyn. Stochastic Geometry and Wireless Networks, Volume II - Applications. *Found. Trends Netw.*, 2(1-2):1–312, 2009.

5. N. Bambos, S. Chen, and G. Pottie. Channel access algorithms with active link protection for wireless communication networks with power control.

IEEE/ACM Transactions on Networking, 8(5):583–597, Oct 2000. ISSN 1063-6692. doi: 10.1109/90.879345.

6. S. Barghi, A. Khojastepour, K. Sundaresan, and S. Rangarajan. Characterizing the throughput gain of single cell MIMO wireless systems with full duplex radios. In *2012 10th International Symposium on Modeling and Optimization in Mobile, Ad Hoc and Wireless Networks (WiOpt)*, pages 68–74, May 2012.

7. D. Bharadia, E. McMilin, and S. Katti. Full duplex radios. *SIGCOMM Comput. Commun. Rev.*, 43(4):375–386, Aug. 2013. ISSN 0146-4833. doi: 10.1145/2534169.2486033. URL `http://doi.acm.org/10.1145/2534169.2486033`.

8. J. W. Byers, M. Luby, M. Mitzenmacher, and A. Rege. A digital fountain approach to reliable distribution of bulk data. *SIGCOMM Comput. Commun. Rev.*, 28(4):56–67, Oct. 1998. ISSN 0146-4833. doi: 10.1145/285243.285258. URL `http://doi.acm.org/10.1145/285243.285258`.

9. V. Chandrasekhar, J. Andrews, and A. Gatherer. Femtocell networks: a survey. *IEEE Communications Magazine*, 46(9):59–67, Sep. 2008. ISSN 0163-6804. doi: 10.1109/MCOM.2008.4623708.

10. V. Chandrasekhar, J. Andrews, T. Muharemovic, Z. Shen, and A. Gatherer. Power control in two-tier femtocell networks. *IEEE Transactions on Wireless Communications*, 8(8):4316–4328, Aug. 2009. ISSN 1536-1276. doi: 10.1109/TWC.2009.081386.

11. B. Chen, Y. Yenamandra, and K. Srinivasan. Flexradio: Fully flexible radios. *Technical Report*, 2013. Online: http://web.cse.ohio-state.edu/~kannan/cosyne/nsdi14-anyduplex.pdf.

12. S. Chen, M. Beach, and null. Division-free duplex for wireless applications. *Electronics Letters*, 34(2):147–148, 1998. ISSN 0013-5194. doi: 10.1049/el:19980022.

13. W. Cheng, X. Zhang, and H. Zhang. Optimal dynamic power control for full-duplex bidirectional-channel based wireless networks. In *INFOCOM, 2013 Proceedings IEEE*, pages 3120–3128, April 2013. doi: 10.1109/INFCOM.2013.6567125.

14. M. Chiang, P. Hande, T. Lan, and C. W. Tan. Power control in wireless cellular networks. *Found. Trends Netw.*, 2(4):381–533, Apr. 2008. ISSN 1554-057X. doi: 10.1561/1300000009.

15. J. I. Choi, M. Jain, K. Srinivasan, P. Levis, and S. Katti. Achieving single channel, full duplex wireless communication. In *Proceedings of the sixteenth annual international conference on Mobile computing and networking*, MobiCom '10, pages 1–12, New York, NY, USA, 2010. ACM. ISBN 978-1-4503-0181-7. doi: 10.1145/1859995.1859997. URL `http://doi.acm.org/10.1145/1859995.1859997`.

16. D. Bharadia, E. McMilin and S. Katti. Full Duplex Radios. available at http://www.stanford.edu/ skatti/pubs/sigcomm13-fullduplex.pdf accessed on Aug. 15, 2013.

17. S. Das and H. Viswanathan. A comparison of reverse link access schemes for next-generation cellular systems. *IEEE Journal on Selected Areas in Communications*, 24(3):684–692, 2006. ISSN 0733-8716. doi: 10.1109/JSAC.2005.862419.

18. M. Duarte and A. Sabharwal. Full-duplex wireless communications using off-the-shelf radios: Feasibility and first results. In *2010 Conference Record of the Forty Fourth Asilomar Conference on Signals, Systems and Computers (ASILOMAR)*, pages 1558–1562, 2010. doi: 10.1109/ACSSC.2010.5757799.

19. T. ElBatt and A. Ephremides. Joint scheduling and power control for wireless ad-hoc networks. In *Twenty-First Annual Joint Conference of the IEEE Computer and Communications Societies (INFOCOM'02)*, volume 2, pages 976–984, New York, NY, USA, 2002. doi: 10.1109/INFCOM.2002.1019345.

20. Fairview Microwave. SMA Circulator with 19 dB isolation from 800 MHz to 960 MHz. Online at http://www.fairviewmicrowave.com/images/productPDF/SFC8096.pdf.

21. G. Foschini and Z. Miljanic. A simple distributed autonomous power control algorithm and its convergence. *IEEE Transactions on Vehicular Technology*, 42(4):641–646, Nov. 1993. ISSN 0018-9545. doi: 10.1109/25.260747.

22. R. K. Ganti and M. Haenggi. Limit of the Transport Capacity of a Dense Wireless Network. *Journal of Applied Probability*, 47:886–892, Sep 2010.

23. S. Goyal, P. Liu, S. Hua, and S. Panwar. Analyzing a full-duplex cellular system. In *2013 IEEE 47th Annual Conference on Information Sciences and Systems (CISS)*, pages 1–6, 2013.

24. S. Grandhi and J. Zander. Constrained power control in cellular radio systems. In *1994 IEEE 44th Vehicular Technology Conference*, pages 824–828 vol.2, Stockholm, Sweden, Jun. 1994. doi: 10.1109/VETEC.1994.345205.

25. S. Grandhi, R. Vijayan, and D. Goodman. Distributed power control in cellular radio systems. *IEEE Transactions on Communications*, 42(234):226–228, Feb.–Apr. 1994. ISSN 0090-6778. doi: 10.1109/TCOMM.1994.577019.

26. S. A. Grandhi, J. Zander, and R. Yates. Constrained power control. *Wireless Personal Communications*, 1:257–270, 1994. ISSN 0929-6212.

27. A. Guo and M. Haenggi. Asymptotic deployment gain: A simple approach to characterize the SINR distribution in general cellular networks. *Communications, IEEE Transactions on*, PP(99):1–1, 2015. ISSN 0090-6778. doi: 10.1109/TCOMM.2014.2387170.

28. A. Guo, Y. Zhong, M. Haenggi, and W. Zhang. Success probabilities in Gauss-Poisson networks with and without cooperation. In *2014 IEEE International Symposium on Information Theory (ISIT'14)*, July 2014.

29. D. Guo and L. Zhang. Virtual full-duplex wireless communication via rapid on-off-division duplex. In *2010 48th Annual Allerton Conference on Communication, Control, and Computing (Allerton)*, pages 412–419, 2010. doi: 10.1109/ALLERTON.2010.5706936.

30. D. Guo, J. Luo, L. Zhang, and K. Shen. Compressed neighbor discovery for wireless networks. *Performance Evaluation*, 70:457–471, Jul. 2013.

31. P. Gupta and P. Kumar. The capacity of wireless networks. *IEEE Transactions on Information Theory*, 46(2):388–404, Mar. 2000. ISSN 0018-9448. doi: 10.1109/18.825799.

32. M. Haenggi. Outage, Local Throughput, and Capacity of Random Wireless

Networks. *IEEE Transactions on Wireless Communications*, 8(8):4350–4359, Aug. 2009.

33. M. Haenggi. *Stochastic Geometry for Wireless Networks*. Cambridge University Press, 2012.

34. M. Haenggi. The mean interference-to-signal ratio and its key role in cellular and amorphous networks. *IEEE Wireless Communication Letters*, 3:597–600, Dec 2014.

35. L. S. Hanh. *Complex numbers and geometry*. The Mathematical Association of America, 1994.

36. S. Hanly. An algorithm for combined cell-site selection and power control to maximize cellular spread spectrum capacity. *IEEE Journal on Selected Areas in Communications*, 13(7):1332–1340, Sep. 1995. ISSN 0733-8716. doi: 10.1109/49.414650.

37. J. Heiskala and J. Terry. *OFDM Wireless LANs: A Theoretical and Practical Guide*. Sams Publishing, 2002.

38. M. Jain, J. I. Choi, T. Kim, D. Bharadia, S. Seth, K. Srinivasan, P. Levis, S. Katti, and P. Sinha. Practical, real-time, full duplex wireless. In *Proceedings of the 17th annual international conference on Mobile computing and networking*, MobiCom '11, pages 301–312, New York, NY, USA, 2011. ACM. ISBN 978-1-4503-0492-4. doi: 10.1145/2030613.2030647. URL `http://doi.acm.org/10.1145/2030613.2030647`.

39. H. Ju, D. Kim, H. Poor, and D. Hong. Bi-directional beamforming and its capacity scaling in pairwise two-way communications. *IEEE Transactions on*

Wireless Communications, 11(1):346–357, January 2012. ISSN 1536-1276. doi: 10.1109/TWC.2011.111611.110970.

40. E.-S. Jung and N. H. Vaidya. A power control MAC protocol for ad hoc networks. In *Proceedings of the 8th annual international conference on Mobile computing and networking*, MobiCom '02, pages 36–47, New York, NY, USA, 2002. ACM. ISBN 1-58113-486-X. doi: 10.1145/570645.570651.

41. G. Kenworthy. Self-cancelling full-duplex RF communication system. In *US Patent 5,691,978*, 1997.

42. A. K. Khandani. Two-way (true full-duplex) wireless. In *2013 13th Canadian Workshop on Information Theory (CWIT)*, pages 33–38, June 2013. doi: 10.1109/CWIT.2013.6621588.

43. A. Khandekar, N. Bhushan, J. Tingfang, and V. Vanghi. LTE-Advanced: Heterogeneous networks. In *2010 European Wireless Conference (EW)*, pages 978–982, 2010. doi: 10.1109/EW.2010.5483516.

44. D. Kim, S. Park, H. Ju, and D. Hong. Transmission capacity of full-duplex-based two-way ad hoc networks with ARQ protocol. *IEEE Transactions on Vehicular Technology*, 63(7):3167–3183, Sept 2014. ISSN 0018-9545. doi: 10.1109/TVT.2014.2302013.

45. M. Knox. Single antenna full duplex communications using a common carrier. In *Wireless and Microwave Technology Conference (WAMICON), 2012 IEEE 13th Annual*, pages 1–6, 2012. doi: 10.1109/WAMICON.2012.6208455.

46. K. Kredo, II and P. Mohapatra. Medium access control in wireless sensor networks. *Comput. Netw.*, 51(4):961–994, Mar. 2007. ISSN 1389-1286. doi: 10.

1016/j.comnet.2006.06.012. URL http://dx.doi.org/10.1016/j.comnet.2006.06.012.

47. S. Kumar, V. S. Raghavan, and J. Deng. Medium access control protocols for ad hoc wireless networks: A survey. *Ad Hoc Networks*, 4(3):326–358, 2006. ISSN 1570-8705. doi: 10.1016/j.adhoc.2004.10.001. URL http://www.sciencedirect.com/science/article/pii/S1570870504000873.

48. C.-H. Lee and M. Haenggi. Interference and outage in Poisson cognitive networks. *IEEE Transactions on Wireless Communications*, 11(4):1392–1401, Apr. 2012. ISSN 1536-1276. doi: 10.1109/TWC.2012.021512.110131.

49. Y. Li and A. Ephremides. Joint scheduling, power control, and routing algorithm for ad-hoc wireless networks. In *Proceedings of the 38th Annual Hawaii International Conference on System Sciences, 2005 (HICSS'05)*, page 322b, Big Island, Hawaii, USA, Jan. 2005. doi: 10.1109/HICSS.2005.367.

50. S. Lin and D. J. Costello. *Error Control Coding, Second Edition*. Prentice-Hall, Inc., Upper Saddle River, NJ, USA, 2004. ISBN 0130426725.

51. A. M. Mathai. *An introduction to geometrical probability: distributional aspects with applications*. Gordan and Breach Science Publishers, 1999.

52. National Instruments Cooperation. Device specifications NI USRP 2920 50 MHz to 2.2 GHz Tunable RF Transceiver. Online at http://www.ni.com/pdf/manuals/375839a.pdf.

53. C. S. Ogilvy. *Excursions in Geometry*. Dover Publications, 1990.

54. H. O. Peterson, J. B. Attwood, H. E. Goldstine, G. E. Hansell, and R. E.

Schock. Observations and comparisons on radio telegraph signaling by frequency shift and on-off keying. *RCA Review*, 12:11–32, Mar. 1946.

55. M. Pursley, H. Russell, and J. Wysocarski. Energy-efficient transmission and routing protocols for wireless multiple-hop networks and spread-spectrum radios. In *EUROCOMM 2000. Information Systems for Enhanced Public Safety and Security. IEEE/AFCEA*, pages 1–5, 2000. doi: 10.1109/EURCOM.2000.874759.

56. L. Qian, X. Li, J. Attia, and Z. Gajic. Power control for cognitive radio ad hoc networks. In *15th IEEE Workshop on Local Metropolitan Area Networks, 2007 (LANMAN'07)*, pages 7–12, Princeton, NJ, USA, Jun. 2007. doi: 10.1109/LANMAN.2007.4295967.

57. T. Riihonen, S. Werner, and R. Wichman. Transmit power optimization for multiantenna decode-and-forward relays with loopback self-interference from full-duplex operation. In *2011 Conference Record of the Forty Fifth Asilomar Conference on Signals, Systems and Computers (ASILOMAR)*, pages 1408–1412, Nov 2011. doi: 10.1109/ACSSC.2011.6190248.

58. T. Riihonen, S. Werner, and R. Wichman. Hybrid full-duplex/half-duplex relaying with transmit power adaptation. *IEEE Transactions on Wireless Communications*, 10(9):3074–3085, September 2011. ISSN 1536-1276. doi: 10.1109/TWC.2011.071411.102266.

59. L. Rizzo. Effective erasure codes for reliable computer communication protocols. *SIGCOMM Comput. Commun. Rev.*, 27(2):24–36, Apr. 1997. ISSN 0146-4833. doi: 10.1145/263876.263881. URL `http://doi.acm.org/10.1145/263876.263881`.

60. A. Sahai, G. Patel, and A. Sabharwal. Pushing the limits of full-duplex: Design and real-time implementation. *CoRR*, abs/1107.0607, 2011.

61. S. Sorooshyari, C. W. Tan, and M. Chiang. Power control for cognitive radio networks: Axioms, algorithms, and analysis. *IEEE/ACM Transactions on Networking*, 20(3):878 –891, Jun. 2012. ISSN 1063-6692. doi: 10.1109/TNET.2011.2169986.

62. S. Srinivasa and M. Haenggi. Distance Distributions in Finite Uniformly Random Networks: Theory and Applications. *IEEE Transactions on Vehicular Technology*, 59(2):940–949, Feb. 2010.

63. Z. Tong and M. Haenggi. Transport Density vs. Channel Access Time in Wireless Networks: Power Control and Efficient MAC Design. In *2012 Allerton Conference on Communication, Control and Computing*, Monticello, IL, Oct. 2012.

64. Z. Tong and M. Haenggi. Optimizing Spatial Reuse by Dynamic Power Control. In *IEEE International Conference on Communications (ICC'12)*, Ottawa, Canada, June 2012.

65. Z. Tong and M. Haenggi. Geometric analysis of distributed power control and Möbius MAC design. *Wireless Communications and Mobile Computing*, 2014. ISSN 1530-8677. doi: 10.1002/wcm.2554. URL `http://dx.doi.org/10.1002/wcm.2554`. Accepted.

66. Z. Tong and M. Haenggi. Throughput Analysis for Full-Duplex Wireless Networks with Imperfect Self-interference Cancellation. *IEEE Transaction on Communications*, 2015. Submitted.

67. Z. Tong and M. Haenggi. Throughput analysis for wireless networks with full-duplex radios. In *2015 IEEE Wireless Communications and Networking Conference (WCNC'15)*, New Orleans, LA, USA, March 2015.

68. Z. Tong, C. Russ, S. Vanka, and M. Haenggi. Prototype of Virtual Full Duplex via Rapid On-Off-Division Duplex. *IEEE Transactions on Communication*, 2014. Submitted, available at https://www3.nd.edu/ mhaenggi/pubs/tcom15a.pdf.

69. S. Vanka, S. Srinivasa, Z. Gong, P. Vizi, K. Stamatiou, and M. Haenggi. Superposition Coding Strategies: Design and Experimental Evaluation. *IEEE Transactions on Wireless Communications*, 11(7):2628–2639, July 2012.

70. R. Vaze, K. Truong, S. Weber, and R. Heath. Two-way transmission capacity of wireless ad-hoc networks. *IEEE Transactions on Wireless Communications*, 10(6):1966–1975, June 2011. ISSN 1536-1276. doi: 10.1109/TWC.2011.041311.101488.

71. M. Z. Win and R. A. Scholtz. Ultra-wide bandwidth time-hopping spread-spectrum impulse radio for wireless multiple-access communications. *IEEE Transactions on Communications*, 48:679–691, 2000.

72. M. Xiao, N. B. Shroff, and E. K. P. Chong. Distributed admission control for power-controlled cellular wireless systems. *IEEE/ACM Trans. Netw.*, 9(6): 790–800, Dec. 2001. ISSN 1063-6692. doi: 10.1109/90.974532.

73. R. Yates. A framework for uplink power control in cellular radio systems. *IEEE Journal on Selected Areas in Communications*, 13(7):1341–1347, Sep. 1995. ISSN 0733-8716. doi: 10.1109/49.414651.

74. T. Yucek and H. Arslan. A survey of spectrum sensing algorithms for cognitive radio applications. *Communications Surveys & Tutorials, IEEE*, 11(1):116–130, 2009. ISSN 1553-877X. doi: 10.1109/SURV.2009.090109.

75. J. Zander. Distributed cochannel interference control in cellular radio systems. *IEEE Transactions on Vehicular Technology*, 41(3):305–311, Aug. 1992. ISSN 0018-9545. doi: 10.1109/25.155977.

76. L. Zhang and D. Guo. Neighbor discovery in wireless networks using compressed sensing with Reed-Muller codes. In *2011 International Symposium on Modeling and Optimization in Mobile, Ad Hoc and Wireless Networks (WiOpt)*, pages 154–160, 2011. doi: 10.1109/WIOPT.2011.5930008.

77. L. Zhang and D. Guo. Virtual full duplex wireless broadcasting via compressed sensing. *IEEE/ACM Trans. on Networking*, 22:1659–1671, October 2014.

78. X. Zhang and M. Haenggi. Random power control in Poisson networks. *IEEE Transactions on Communications*, 60(9):2602–2611, Sep. 2012.

79. X. Zhang and M. Haenggi. Delay-optimal Power Control Policies. *IEEE Transactions on Wireless Communications*, 11(10):3518–3527, Oct. 2012.

80. Q. Zhao and B. Sadler. A survey of dynamic spectrum access. *IEEE Signal Processing Magazine*, 24(3):79–89, May 2007. ISSN 1053-5888. doi: 10.1109/MSP.2007.361604.

81. G. Zheng. Joint beamforming optimization and power control for full-duplex MIMO two-way relay channel. *IEEE Transactions on Signal Processing*, 63 (3):555–566, Feb 2015. ISSN 1053-587X. doi: 10.1109/TSP.2014.2376885.

82. R. E. Ziemer and W. H. Tranter. *Principles of Communications*. Wiley Publishing, 6th edition, 2008. ISBN 0470252545, 9780470252543.